University of California
Los Angeles

Terahertz Quantum-Cascade Transmission-Line Metamaterials

A dissertation submitted in partial satisfaction
of the requirements for the degree
Doctor of Philosophy in Electrical Engineering

by

Amir Ali Tavallaee

2012

Abstract of the Dissertation

Terahertz Quantum-Cascade Transmission-Line Metamaterials

by

Amir Ali Tavallaee

Doctor of Philosophy in Electrical Engineering

University of California, Los Angeles, 2012

Professor Benjamin S. Williams, Chair

Terahertz quantum-cascade (QC) lasers operating at $0.6 - 5$ THz ($\lambda \sim 60 - 500$ μm) are poised to become the dominant solid-state sources of continuous-wave (cw) far-infrared radiation enabling applications in terahertz spectroscopy, imaging, and sensing. QC-lasers are the longest wavelength semiconductor laser sources in which terahertz gain is obtained from electronic intersubband radiative transitions in GaAs/AlGaAs heterostructure quantum wells. Since their invention in 2001, rapid development has enabled demonstration of cw powers greater than 100 mW. However, challenges still remain in the areas of operating temperature, laser efficiency and power, and beam quality to name a few.

The highest-temperature operation of terahertz quantum-cascade lasers (200 K pulsed, 117 K cw) depends on the use of a low-loss "metal-metal" waveguide where the active gain material is sandwiched between two metal cladding layers; a technique similar, in concept, to microstrip transmission line technology at microwave frequencies. Due to the subwavelength transverse dimensions of the metal-metal waveguide, however, obtaining a directive beam pattern and efficient out-coupling of THz power is non-trivial.

This thesis reports the demonstration of a one-dimensional waveguide for terahertz quantum-cascade lasers that acts as a leaky-wave antenna and tailors laser radiation in one dimension to a directional beam. This scheme adapts microwave transmission-line metamaterial concepts to a planar structure realized in terahertz metal-metal waveguide technology and is fundamentally different from distributed feedback/photonic crystal structures that work based on Bragg scattering of propagating modes. The leaky-wave metamaterial antenna operates based on a propagating mode with an effective phase index smaller than unity such that it radiates in the surface direction via a leaky-wave mechanism. Surface emission ($\sim 40^\circ$ from broadside) with a single directive beam (FWHM $\sim 15^\circ$) at 2.74 THz was demonstrated from terahertz QC-lasers with leaky-wave coupler antennas which exhibited slope efficiencies ~ 4 times greater than conventional Fabry-Pérot metal-metal waveguides. Using this technique the first demonstration of beam scanning for a terahertz QC-laser was reported (from $35^\circ - 60^\circ$) as the emission frequency varied from $2.65 - 2.81$ THz.

Towards the bigger goal of realizing an active terahertz metamaterial to ultimately develop "zero-index" terahertz quantum-cascade lasers immune to spatial hole burning, or "negative-index" metamaterials for superresolution terahertz imaging, a composite right-/left-handed transmission-line metamaterial based upon subwavelength metal waveguide loaded with terahertz QC material was demonstrated. Due to the addition of distributed series capacitors (realized by introducing gaps in top metallization) and shunt inductors (realized by operating in the higher-order lateral mode of the waveguide), the transmission-line metamaterial exhibits left-handed (backward waves or negative index) leaky-wave propagation from $2.3 - 2.45$ THz in addition to the conventional right-handed leaky-wave behavior (from $2.6 - 3.0$ THz).

The dissertation of Amir Ali Tavallaee is approved.

Tatsuo Itoh

Bahram Jalali

Mark Morris

Benjamin S. Williams, Committee Chair

University of California, Los Angeles

2012

To my father . . .

for his unconditional love and ceaseless support.

Table of Contents

Acknowledgments

First and foremost, I would like to thank my advisor Prof. Benjamin S. Williams for not only giving me the opportunity to work on this project but also for teaching and advising me along the way. His insight, support, and patience have guided me through difficult periods.

I also thank Prof. Tatsuo Itoh for his academic advising, and Prof. Bahram Jalali and Prof. Mark Morris for agreeing to serve on my thesis committee.

A large part of the success of this project is due to the excellent MBE growths obtained from Qi-Sheng Chen at Northrop Grumman.

I also wish to thank my many colleagues and research group-mates. I am particularly indebted to Alexandros Shailos and Cyrus Haselby who trained me with many of the valuable skills that I have today. I consider myself lucky to have worked along with them at the early stages of the lab. I am grateful to many other past and present students in this research group including Zhiping Chen, Karan Mehta, Matthew Puckett, Partia Naghibi, Luyao Xu, Chris Curwen, Benjamin Burnett, and Zhijun Liu. It has been a pleasure to work with them and to learn from them. I would specifically like to thank Philip Hon for all his help with many of the simulations. I am deeply grateful to the members of the Integrated NanoMaterials Core Lab namely Charles Reyner, Giacomo Mariani, Adam Scofield, Pradeep Senanayake, and Andrew Lin for all the help given to me during the course of this project. I appreciate all the help and support from the staff at HFC, NRF, and CNSI.

Finally, I want to thank my parents and sisters for all of their love and support. None of this would have been possible without you. Thanks to all of my family and friends who made my stay in Los Angeles unforgettable.

Vita

2003	B.S. (Electrical Engineering), Sharif University of Technology, Tehran, Iran.
2006	M.Eng. (Electrical and Computer Engineering), McGill University, Montréal, QC, Canada.
2004–2006	Research Assistant, Electrical and Computer Engineering Department, McGill University.
2004–2006	Teaching Assistant, Electrical and Computer Engineering Department, McGill University.
2007–present	Research Assistant, Electrical Engineering Department, UCLA.
2008–2009	Teaching Assistant, Electrical Engineering Department, UCLA.

Publications and Presentations

A. A. Tavallaee, P. Hon, K. Mehta, T. Itoh, and B. S. Williams,"Zero-Index Terahertz Quantum-Cascade Metamaterial Lasers," IEEE J. of Quantum Electronics, **46**, 7, July 2010, pp. 1091 − 1098. **(paper covered in Nature Photonics "Research Highlights" July 2010)**

A. A. Tavallaee, B. S. Williams, P. Hon, T. Itoh, and Q.-S. Chen, "Terahertz Quantum-Cascade Laser with Active Leaky-Wave Antenna," Appl. Phys. Lett.,

99, 14, Oct 2011, pp. 141115.

Z. Liu, P. Hon, A. A. Tavallaee, T. Itoh, and B. S. Williams, "Terahertz Composite Right-Left Handed Transmission-Line Metamaterial Waveguides," Appl. Phys. Lett., **100**, 14, Feb 2012, pp. 071101.

P. Hon, A. A. Tavallaee, Q.-S. Chen, B. S. Williams, and T. Itoh, "Radiation Model for Terahertz Transmission-Line Metamaterial Quantum-Cascade Lasers," IEEE Trans. on Terahertz Science and Technology, **2**, 3, May 2012, pp. 323 − 332.

A. A. Tavallaee, K. Mehta, B. S. Williams, P. Hon, and T. Itoh, "Feasibility of a Terahertz Quantum Cascade Active Metamaterial Based on Composite Right/Left-Handed Transmission Lines," 10th International Conference on Intersubband Transitions in Quantum Wells (ITQW), Montreal, QC, Canada, (September 2009).

A. A. Tavallaee, M. Puckett, B. S. Williams, P. Hon, T. Itoh, and Q.-S. Chen, "A Terahertz Quantum-Cascade Laser with an Active Leaky-Wave Metamaterial Antenna," 2011 Conference on Lasers and Electro-optics (CLEO), Baltimore, MD, (May 2011).

A. A. Tavallaee, M. Puckett, B. S. Williams, P. Hon, T. Itoh, and Q.-S. Chen, "An Active Terahertz Quantum-Cascade Metamaterial Antenna," 11th International Conference on Intersubband Transitions in Quantum Wells (ITQW), Sardinia, Italy, (September 2011).

CHAPTER 1

Introduction

The terahertz spectral regime, defined as frequencies from $0.3 - 10$ THz (wavelengths from $30 - 1000$ μm), has long resisted technological development mostly due to the lack of economical, compact, and efficient components. Primarily driven by the astronomical and space science community, terahertz sources and detectors are highly desirable for applications in spectroscopy, imaging, and sensing [1–4]. Operation at such wavelengths is convolved with unique challenges not present for neighboring millimeter-wave and infrared spectral ranges. For instance, despite the fact that sensitive terahertz detectors such as photoconductive and bolometric semiconductor detectors have long existed [5, 6], there has been a dearth of coherent sources of terahertz radiation. However, in the past decade there has been a dramatic surge of interest in the terahertz, and a number of simultaneous technological advances in the field has led to the development of efficient, low-cost, and coherent sources of radiation.

Traditionally, terahertz generation has relied on indirect techniques, many, for instance, based on down conversion from visible range by employing nonlinear techniques such as photomixing in photoconductive antennas [7–9], or by up conversion from the microwave regime using chains of frequency multipliers [10–12]. Advances in these areas have led to the development of optical-heterodyne converters/photomixers that are capable of generating coherent continuous-wave (cw) terahertz radiation from microwaves up to 3.8 THz from low-temperature-

grown (LTG) gallium arsenide (GaAs) [13], or Uni-Traveling Carrier Photodiodes (UTC-PDs) [14]. Today there exist frequency multiplier-based all solid-state electronic sources delivering useful levels of output power at frequencies as high as 2.7 THz [15, 16]. A prime example is the 1.9 THz frequency multiplier chain developed by the National Aeronautics and Space Administration (NASA) for a high-resolution spectrometer employed in European Space Agency's (ESA's) satellite Herschel [17, 18]. Herschel (launched 2009) is equipped with a Heterodyne Instrument for the Far Infrared (HIFI) that covers two bands ($157-212$ μm and $240-625$ μm), complementary to two other photoconductor array camera and imaging spectrometers PACS and SPIRE, at wavelength ranges $55-210$ μm and $194-672$ μm respectively [19]. In the past few years, microwave solid-state amplifiers and oscillators have reached cut-off frequency f_{T} and maximum oscillation frequency f_{max} surpassing 500 GHz and beyond [20]. High electron mobility transistors (HEMTs) have been demonstrated in Indium Phosphide (InP) materials system with $f_{\mathrm{T}} = 586$ GHz and $f_{\mathrm{max}} > 1$ THz [21, 22]. Some of the best data reported for heterojunction bipolar transistors (HBTs) also include InP HBTs with $f_{\mathrm{T}} > 480$ GHz and $f_{\mathrm{max}} \approx 1$ THz [23], and gallium nitride (GaN) power amplifiers are rapidly emerging [24]. Gunn diodes, Tunnel injection Transit-Time (TUNNETT) diodes, and Impact Avalanche Transit-Time (IMPATT) diodes have surpassed their submillimeter-wave limits [25, 26], and resonant tunneling diodes (RTDs) can now deliver microwatts of power at 1 THz at room temperature [27]. However, the high-frequency performance of millimeter-wave solid-state devices is inherently limited by resistance-capacitance effects and transit time of carriers. Their output power rolls off to microwatts levels as they approach terahertz frequencies ($\propto 1/\nu^4$), which may be small for practical applications.

On the other hand, direct terahertz generation using conventional photonic approaches has its own limitations since the wavelength of the emitted photon

in a diode laser is determined, to the first order, by the bandgap energy of the material —the longest wavelength interband lasers are lead salt lasers emitting around 15 THz [28]. Solid-state terahertz laser sources based on impurity-doped germanium or silicon are also limited to pulsed operation, require extensive cryogenic cooling and deliver very low output powers [29]. In fact, until recently, the only direct sources of cw terahertz radiation were optically pumped gas lasers [30] or free electron lasers [31] which have their own limitations in terms of efficiency, size and complexity. The quantum-cascade laser [32] is a new solid-state source of far-infrared radiation that can deliver hundreds of milliwatts of cw power in the terahertz. In this thesis, I describe the successful development of novel GaAs terahertz devices and components based on terahertz quantum-cascade lasers [33] that operate below the semiconductor *Reststrahlen* band, i.e. $8-9$ THz in GaAs.

1.1 Terahertz Quantum-Cascade Lasers

Terahertz quantum-cascade lasers [33,34] are the longest wavelength semiconductor laser sources, with operation demonstrated from $1.2-5$ THz ($\lambda \sim 60-250\ \mu$m) [35,36] (and as low as 0.6 THz with application of a magnetic field [37,38]). Such sources have the potential to enable applications in terahertz imaging, sensing, and spectroscopy [39–41], in particular for security screening, radio astronomy, explosive detection, and non-destructive evaluation. Since their invention in 2001, rapid development has enabled demonstration of continuous-wave powers greater than 100 mW in some cases. However, challenges remain in the areas of operating temperature —cooling is still required with $T_{\max} \sim 200$ K [42]—, laser efficiency and power, beam quality, and frequency stability and tuning to name a few.

In a QC-laser, THz gain is obtained from *intra*band radiative transitions in two-dimensional coupled quantum-well GaAs/AlGaAs heterostructures. In-

traband optical transitions are inherently unipolar in nature and occur entirely between quantized states (subbands) of conduction band (or valence band). This allows one to cascade many repetitions of a superlattice heterostructure (module) to achieve a significantly large number of photons per carrier. Moreover, the energy of the emitted photon can be tailored to the desired long-wavelength regime by engineering the subband states eigenenergies —theoretically, $\hbar\omega$ as low as few meVs to as high as the heterostructure band offset ΔE_c (or ΔE_v). This is fundamentally different from *inter*band bipolar lasers in which radiative transition involves an electron-hole recombination. The photon energy of interband lasers is essentially determined by the bandgap E_g of the quantum well material (on the order of 1 eV). Hence, the extension of bipolar laser technology to the far-infrared is rendered impractical, as materials with bandgaps less than 40 meV would be required. For this reason, the quantum-cascade laser is often referred to as a prime example of bandgap engineering for which the wavelength of light is not determined by the material bandgap, but rather is chosen by engineering electronic states in "artificial molecules."

1.1.1 Active Regions

To obtain THz gain via stimulated emission, a population inversion ΔN between two subbands u and l is required whose energy separation is tailored to the energy of the photon they interact with ($E_{ul} = \hbar\omega_0$). The peak bulk gain for an intersubband transition between initial state $|u\rangle$ and final state $|l\rangle$ at frequency $\nu_0 = \omega_0/2\pi$ is given by the expression $g(\nu_0) \propto \frac{\Delta N f_{ul}}{\Delta\nu}$ where $\Delta\nu$ is the transition linewidth, and $f_{ul} = 2m^*\omega_0|z_{ul}|^2/\hbar$ is the intersubband oscillator strength normalized by the effective electron mass of the well material. The oscillator strength is the ratio of the quantum optical strength of the transition to that of

a classical electron oscillator and depends heavily on the overlap and symmetry of the initial and final wavefunctions ψ_u and ψ_l, which manifests itself via the dipole matrix element $z_{ul} = \langle\psi_l|z|\psi_u\rangle$.

Along with dipole matrix elements, various tunneling rates and scattering processes should be engineered to optimize the gain. When the appropriate electric field is applied, the MQW superlattice conducts current as the carriers transport through a one-dimensional (1D) periodic potential. Let us consider transport in a QCL using our simple two-level system. Electrons are injected into upper radiative state $|u\rangle$ with a current density J and an injection efficiency η. Let the total lifetime of electrons in state $|u\rangle$ be τ_u, where they either relax to state $|l\rangle$ with time τ_{ul}, or parasitically scatter out with time $\tau_{u,\text{para}}$, i.e. $\tau_u^{-1} = \tau_{ul}^{-1} + \tau_{u,\text{para}}^{-1}$. By solving for the standard rate equations, we obtain the steady-state subthreshold population inversion as given by $\Delta N \approx \frac{J}{et}\eta\tau_u(1 - \frac{\tau_l}{\tau_{ul}})$ where τ_l is the lifetime of the lower radiative state $|l\rangle$, e is the elementary charge, and t is the QCL module thickness. This simply reflects the intuitive fact that it is necessary to have $\tau_{ul} \gg \tau_l$ to obtain a population inversion. A long upper state lifetime τ_u is also desirable, as is efficient injection (ideally $\eta = 1$). The challenge at long-wavelength regimes is primarily due to small photon energy ($E_{ul} \approx 4 - 20$ meV). Small energy separation between subbands activates various scattering mechanisms such as electron-electron (e-e), electron-impurity, electron-interface roughness, and thermally activated longitudinally optical (LO)-phonon scattering. Each of these mechanisms reduces the upper radiative state lifetime and therefore the amount of achievable population inversion to a certain degree. Moreover, small E_{ul} makes it difficult to selectively depopulate the lower radiative level l without depopulating the upper level u as well. Additionally, it becomes hard to selectively inject carriers into level u by means of resonant tunneling from the previous module and not level l.

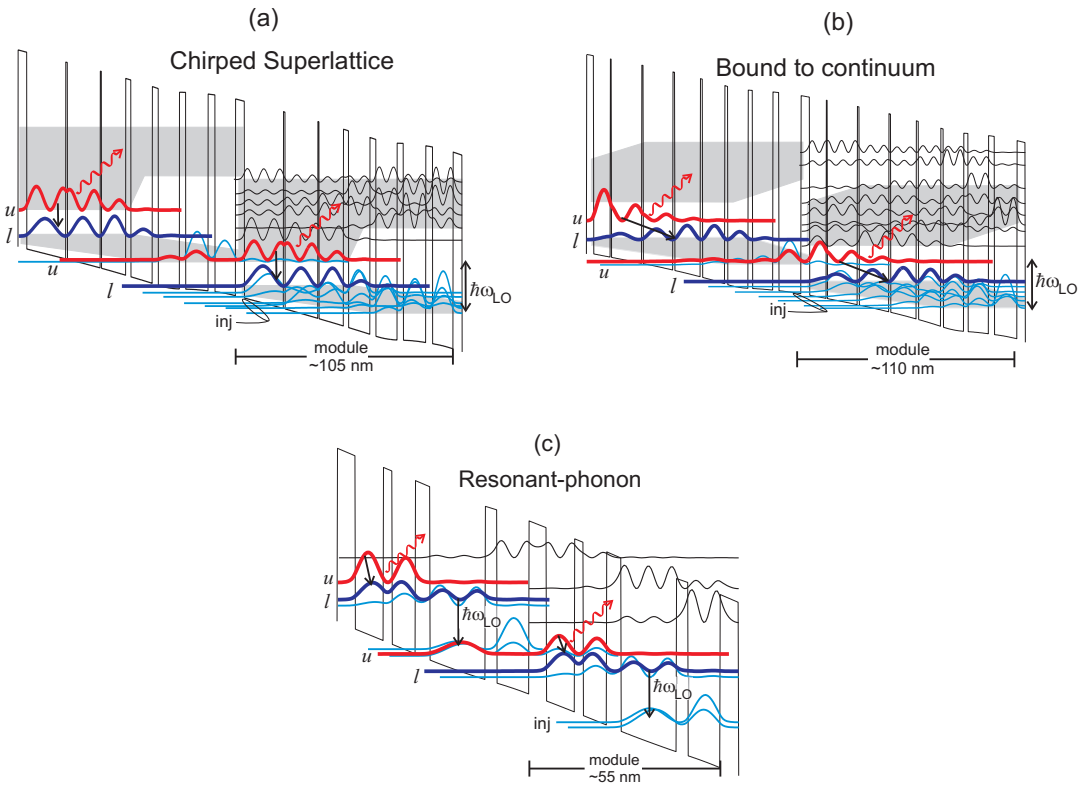

Figure 1.1: Conduction-band diagram for two modules of typical QC structures based on (a) chirped superlattice, (b) bound to continuum, and (c) resonant phonon design schemes. The squared magnitude of the wavefunctions for the various subband states are plotted, with the upper- and lower-radiative state shown in red and blue respectively and the injector states specifically labeled. The grey shaded regions correspond to minibands of states. Plot adapted from [34].

There are currently three major active region designs demonstrated for terahertz QCLs, namely: chirped superlattice, bound-to-continuum, and resonant phonon. The first terahertz QCL demonstrations were based on chirped superlattice designs [33,43] in which single well states couple together to form "minibands" separated by a "minigap." In superlattice QCLs inter-miniband radiative transitions occur at the miniband edge (see Fig. 1.1(a)) and a population inversion is established on the principle that intra-miniband scattering occurs much faster than inter-miniband scattering.

Soon after the first demonstration of terahertz QCLs, Scalari *et al.* [44] reported the bound-to-continuum design which displayed improved performance over the original chirped superlattice design. Like the chirped superlattice, this design also uses a miniband for depopulation of the lower radiative state. However, instead of an inter-miniband transition, the upper radiative state is a somewhat localized "defect" state in the middle of the minigap (Fig. 1.1(b)). The lowest frequency terahertz QCLs are based on bound-to-continuum designs [35, 45]. Compared to superlattice designs, bound-to-continuum designs tend to have a more spatially diagonal radiative transition, and a slightly reduced oscillator strength. However, this is accompanied by reduced nonradiative scattering of the upper state into the miniband, especially at higher temperatures where the upper state lifetime is decreased by thermally activated LO-phonon scattering. The diagonal nature also helps to reduce coupling from the injector into the lower radiative state, which improves injection efficiency.

The best temperature performance has been achieved using resonant-phonon active regions [42,46–48] which use a combination of resonant tunneling and direct electron-LO-phonon scattering for depopulation of lower radiative state rather than intra-miniband scattering (see Fig. 1.1(c)). Operation is based on an inter-well transport by resonant tunneling through the barriers. Electrons quickly relax from the lower radiative state $|l\rangle$ to the ground state $|inj\rangle$ via electron-phonon scattering. This is achieved by setting the separation between states $|l\rangle$ and $|inj\rangle$ within the quantum well to the LO-phonon resonance energy ($\hbar\omega_{LO} \approx 36$ meV in GaAs) as is common for most mid-infrared QC-lasers. This combination of intersubband scattering and resonant tunneling for electron transport in MQWs is often referred to as "sequential resonant tunneling" [49]. Light amplification at $\hbar\omega = E_{ul}$ may be obtained if a population inversion could be achieved between states $|u\rangle$ and $|l\rangle$ at the $inj^{'} - u$ resonance condition, i.e. when the ground state

of one module ($|inj'\rangle$) lines up with the excited state $|u\rangle$ of the adjoining module. The milestone of resonant phonon scheme was in bringing the lower radiative state into a broad resonance with the excited states of the adjacent quantum wells. As a result the lower radiative state is depopulated in a very selective and fast fashion (sub-picosecond LO-phonon scattering) while upper radiative state remains localized and preserves a long lifetime (few picoseconds). Another competing mechanism that ruins the population inversion is the thermal backfilling of the lower radiative state. This effect has also been minimized in the resonant phonon scheme due to the large voltage drop per period ($K_BT < E_{LO}$). Due to its superior temperature performance, this scheme has been the active region of choice in this thesis which will be discussed in greater detail in chapter 2 from a design point of view. The reader is directed to the cited publications to learn more about the chirped-superlattice and bound-to-continuum based designs.

THz QC heterostructures are almost exclusively grown in $GaAs/Al_{0.15}Ga_{0.85}As$ material system using molecular beam epitaxy (MBE) —albeit with two exceptions [50, 51]. The small conduction band offset for $GaAs/Al_xGa_{1-x}As$ ($\Delta E_c \sim$ 130 meV for $x = 15$) works well for terahertz QC-lasers due to a relatively small energy separation required between the subbands. However, some groups have reported terahertz QC-lasers in InGaAs/InAlAs/InP [52, 53] (widely used at mid-infrared wavelengths) and aluminum-free InGaAs/GaAsSb/InP material systems [54, 55] due to the larger ΔE_c and smaller effective mass of electrons in such material systems. The dipole matrix element as well as the upper state lifetime benefit from these low effective electron masses, which directly translates to higher bulk intersubband gain [56]. Despite the lower effective electron mass ($m^*_{\mathrm{InGaAs}} = 0.043m_e$ whereas $m^*_{\mathrm{GaAs}} = 0.067m_e$), the high conduction band offset of $In_{0.53}Ga_{0.47}As/In_{0.52}Al_{0.48}As$ ($\Delta E_c \sim 520$ meV) requires subnanometer thick

barriers which makes the growth very sensitive to variations. The clear advantage of Sb-based material system for terahertz QCLs, however, is the moderate conduction band offset ($\Delta E_c \sim 360$ meV for $In_{0.53}Ga_{0.47}As/GaAs_{0.51}Sb_{0.49}$) and the low effective electron mass of wells and barriers ($m^*_{\mathrm{GaAsSb}} = 0.045m_e$), which allows for designs with thicker barriers.

1.1.2 Waveguides

An equally, if not more, challenging task is designing a low-loss waveguide for terahertz mode confinement. Conventional dielectric cladding waveguides are impractical at long-wavelength regimes (λ_{GaAs} at 3 THz is ~ 30 μm) since the cladding would need to be prohibitively thick (tens of microns). Furthermore, in GaAs/AlGaAs material system, the GaAs substrate has a higher refractive index than AlGaAs. Thus substrate cannot confine the mode in the vertical (growth) direction. For these reasons, the so called "plasmon waveguides" are typically preferred for THz QCLs where the optical mode is confined between two heavily doped semiconductor or metallic contact layers. Losses are mostly due to free carrier absorption. Therefore, any modal overlap with doped regions must be minimized in these waveguiding schemes.

There are currently two types of waveguides used for terahertz QCLs: semi-insulating surface-plasmon (SISP), and metal-metal (MM) waveguides. The first terahertz QCL was demonstrated in the semi-insulating surface-plasmon waveguide [33]. A schematic of the structure and a typical mode pattern for SISP waveguide is shown in Fig. 1.2(a). In this waveguide, the mode is confined between the upper metallic layer and a thin heavily doped semiconductor (n^+) contact layer grown directly below the MQW active region on a semi-insulating GaAs substrate. Lateral electrical contacts are required (SI GaAs substrates used

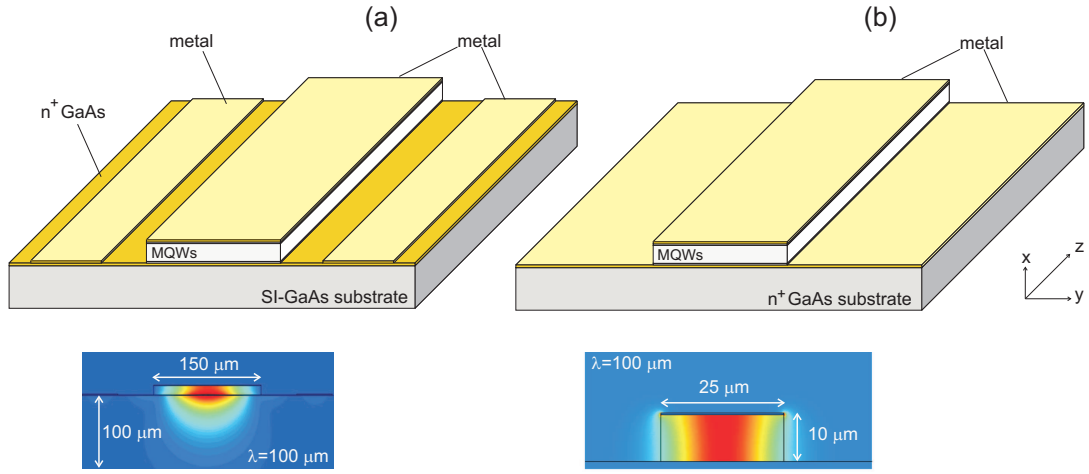

Figure 1.2: Schematic and two-dimensional electromagnetic mode profiles for (a) semi-insulating surface-plasmon waveguide, and (b) metal-metal waveguide at $\nu = 3$ THz.

to avoid free-carrier loss in the substrate) and commonly placed adjacent to the waveguide ridge. Due to the small thickness of the n^+ layer (thinner than its own skin depth) the mode leaks substantially into the substrate and thus have a small overlap with active material resulting in confinement factors $\Gamma \sim 0.2 - 0.5$. Waveguide losses (α_w) are mainly associated with the lower contact layer, however, free carrier absorption in the core active region becomes significant at longer wavelengths ($\alpha_{fc} \propto \lambda^2$).

An alternative to the SISP waveguide is the so-called metal-metal waveguide [57–59] in which the lower n^+ GaAs layer is replaced by a metallic sheet as shown in Fig. 1.2(b). This type of waveguiding scheme is very similar, in concept, to microstrip transmission line technology at microwave frequencies. Owing to very small skin depth in metal ($\sim$ several hundred Angstroms) the waveguide losses are even more minimized as compared to SISP waveguide. Moreover, the double surface-plasmon mode is sandwiched between two metallic layers (typically Cu or Au) resulting in near unity confinement factors. Such a structure can be

readily fabricated using metallic thermocompression wafer bonding followed by substrate removal, leaving an epitaxial thin film bonded to metal that can be processed using conventional microfabrication techniques [47].

In general, MM waveguides demonstrate superior performance in terms of overall waveguide loss (α_w/Γ), lasing threshold ($J_{\rm th}$) and maximum operating temperature ($T_{\rm max}$) compared to SISP waveguides (see Fig. 1.3). Record highest temperatures have been demonstrated in MM waveguides ($T_{\rm max} \sim 200$ K in pulsed operation [42] and ~ 117 K in continuous-wave operation [47]). This is while the highest temperatures reported for SISP waveguides are ~ 110 K in pulsed and < 70 K in cw operation [60]. An enabling component in cw operation of THz QCLs at temperatures well above liquid nitrogen is the feasibility of subwavelength mode confinement with MM waveguides. THz QCL ridges as thin as $2-5$ μm and as narrow as $13-20$ μm have been demonstrated in metal-metal waveguide technology [61–63] which made the heat removal from the core active region easier and dramatically reduced power dissipation. This is not feasible in SISP technology as the mode would totally leak into the substrate. For the same virtue, the metal-metal technology has enabled demonstration of THz QC-lasers below 2 THz (1.69 THz in resonant phonon [61] and as low as 1.2 THz in bound-to-continuum active regions [35, 45]).

Despite their worse temperature performance due to a higher waveguide loss, significantly greater output power (> 100 mW) can be obtained from SISP waveguides in comparison with MM waveguides (< 10 mW). Record peak optical power output with a value of 248 mW in pulsed operation and 138 mW in cw operation has been demonstrated in SISP waveguides [64]. This is attributed to the substantial mode leakage into substrate in SISP waveguides which provides a large radiating aperture, hence efficient outcoupling of terahertz power and directive

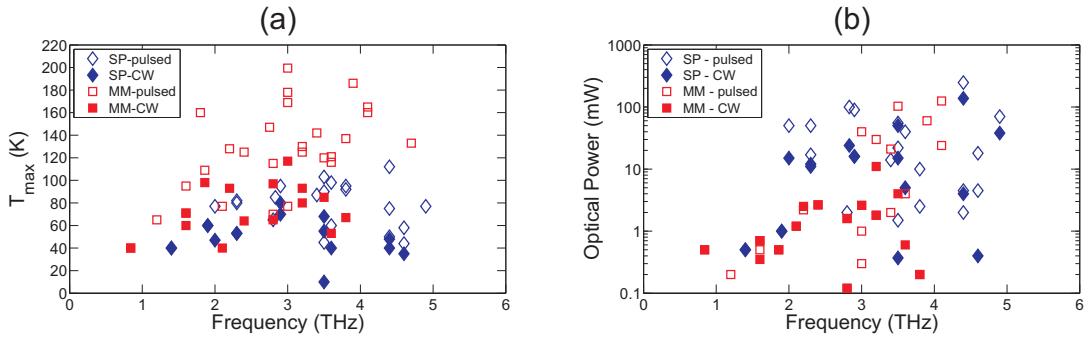

Figure 1.3: State of the art for THz QC-lasers: (a) Maximum operating temperature and (b) maximum THz power versus frequency.

beam patterns. For Fabry-Pérot MM waveguide cavities with cleaved facets, however, radiation is through a subwavelength aperture. The guided terahertz mode, which is highly confined in between the two metal clads, experiences a large modal mismatch at the radiating aperture, yielding high facet reflectivity, poor outcoupling efficiency, and extremely divergent beam pattern with strong interference fringes in the far field [65]. As a result, MM waveguides are generally characterized by facet reflectivities much greater than those of SISP waveguides ($R_{\mathrm{MM}} \sim 0.7 - 0.9$ whereas $R_{\mathrm{SISP}} \sim 0.32$) and an order of magnitude smaller mirror losses ($\alpha_{m,\mathrm{MM}}/\Gamma \sim 0.5 - 2$ cm^{-1} per facet while $\alpha_{m,\mathrm{SISP}}/\Gamma \sim 15 - 30$ cm^{-1} per facet for a 1 mm long cavity) [66].

1.2 Rationale

Owing to superior temperature performance of MM waveguides, there are efforts currently underway to improve their power outcoupling efficiency and radiation patterns. For a MM waveguide operating in its fundamental mode, the facets are the primary source of laser emission, even for laser cavities with subwavelength dimensions and substantial evanescent field in the air [67]. Hence the poor outcoupling of the terahertz power and non-directional beam patterns are

attributed to radiation through a subwavelength aperture and far-field rings in the beam pattern are deemed to originate from the interference of the facets, i.e. two dipole sources separated by distance ℓ (ℓ being the cavity length) as shown in Fig. 1.4(a).

One relatively straightforward solution, at least in concept, is to micromachine mode-matching devices such as the horn antennas widely used in microwave and millimeter-wave regime to launch near Gaussian beams. Facet-mounted antennas provide a smooth transition from waveguide to free-space serving as an impedance transformer which compensates for the large modal mismatch at the facet. By reducing the facet reflectivity (equivalently, increasing the mirror losses) much higher optical coupling efficiencies are achievable at very little penalty in device threshold current density $J_{\rm th}$. Moreover, the radiating aperture of the horn can, in principle, be made desirably large enough to achieve highly directive beam patterns. This approach is particularly promising because it would allow the narrow ridge geometry of the Fabry-Pérot MM QC-laser to be preserved along with its advantages for low power dissipation and high temperature of operation. While fabrication is challenging, several groups have reported preliminary results [68–70] with significant improvements to the collected power and beam patterns even with very crude implementations. For instance, Faist's group at University of Neuchâtel demonstrated a factor of 10 increase in collected power by employing pyramidal structures —inspired by microwave horn antennas— in front of the QCL facet [68]. Later, Maineult *et. al.* demonstrated a metal-metal THz quantum-cascade laser with a micro-transverse electromagnetic (TEM) horn antenna [70]. Lee *et. al.* showed 5 times enhancement in collected power using a silicon hyperhemispherical lens abutted next to the facet of a MM waveguide which served for both index matching and beam collimation purposes. This scheme has so far set the record for peak collectable optical power from a MM-

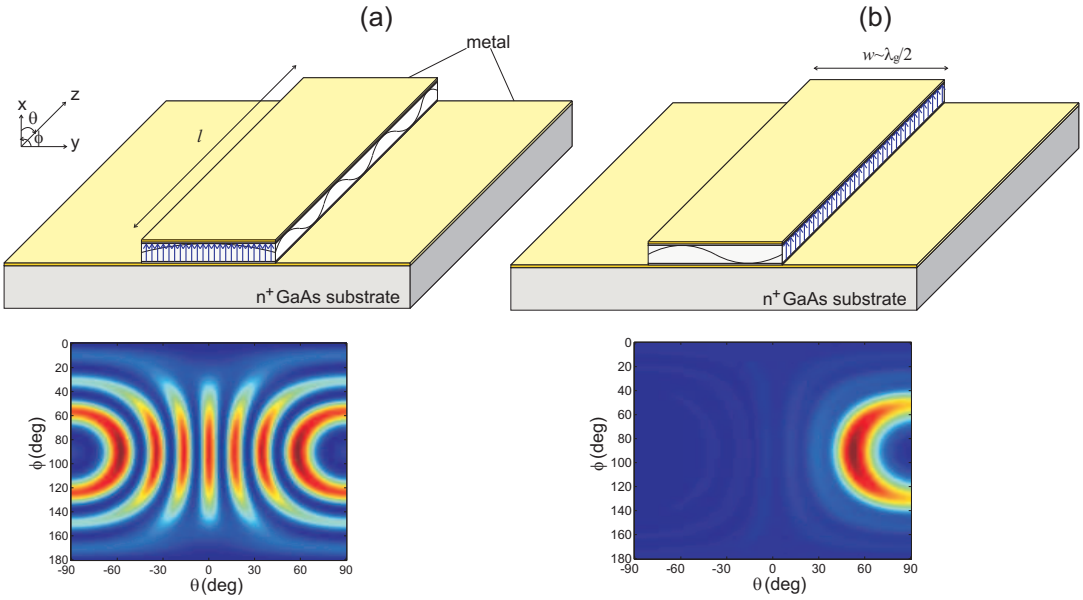

Figure 1.4: Schematic drawing showing the switchover between dominant radiating dipoles in metal-metal waveguides with effective mode index and the corresponding far-field radiation patterns for two representative cases: (a) A narrow-ridge metal-metal waveguide operating in its fundamental mode with an effective index $n_{\text{eff}} \sim 3$ where facets are dominantly radiating, and (b) the same structure operating in its higher-order lateral mode with an effective index $n_{\text{eff}} \sim 0.5$ where radiation is dominantly due to sidewalls. Plot adapted from [67].

waveguide THz QC-laser (145 mW at 5 K) [69].

Another attractive approach to this problem is to use monolithically integrated waveguides and cavities designed to couple radiation in surface or endfire directions. This includes second-order [71–73] and third-order [74–76] distributed feedback (DFB) structures, and two-dimensional photonic crystals [77–79] all of which are fundamentally based on Bragg scattering of propagating waves. Probably, the most appealing demonstration in this category is due to Amanti *et. al.* [74] —a "wire" laser that was designed based on third-order DFB gratings in metal-metal waveguides. In [74], the grating structure scatters propagating waves into a radiating mode with $n_{\text{eff}} = 1$ and operates as an end-fire antenna which results in narrow beam divergence in both directions. Until quite recently,

this scheme held the record slope efficiency of 150 mW/A in MM waveguides. In early 2012, Raffaele Colombelli's group at Université Paris Sud demonstrated efficient power extraction from surface-emitting structures using graded photonic heterostructures (GPH) with record peak surface emission power (> 100 mW) and differential efficiencies (230 mW/A) [80]. Unlike conventional second-order DFBs which operate based on a low-loss antisymmetric bandedge mode, the GPH is forced to operate on a symmetric bandedge mode with much higher radiation efficiency. A major advantage of the third-order DFB over two-dimensional photonic crystal/second-order DFBs is that low-divergence (in both directions) single beam radiation can be achieved even for very narrow laser ridges [75] which is extremely crucial for cw operation of THz QCLs. For a detailed survey of various beam engineering methods used so far in the community to address the problem of poor outcoupling efficiency and beam patterns of MM-waveguide THz QCLs refer to Table 1.1.

This thesis introduces an alternative design approach: a terahertz waveguide based on composite right/left-handed (CRLH) transmission-line metamaterial concepts [90]. CRLH behavior is obtained by loading a metal-metal waveguide/transmission line (typically described by distributed series inductance L_R and shunt capacitance C_R) with shunt inductance L_L and series capacitance C_L elements on a scale much smaller than guided wavelength. Addition of these distributed elements allows the engineering of the transmission line dispersion characteristics to support modes with zero or near zero effective phase indices. Such modes that propagate within the leaky-wave bandwidth ($|n_{\text{eff}}| < 1$) will radiate efficiently into a directive beam in the surface (broadside) direction due to their large emitting aperture and small phase variation between radiating dipoles (Fig. 1.4(b)). Moreover, as the direction of emission is dictated by the dispersion characteristic, the beam can in principle be steered either by varying the

Table 1.1: Survey of various beam engineering approaches for MM-waveguide THz QC-lasers

Design	Peak power	$T_{\max}$	Comments
Cleaved-facet FP [48]	63 mW	186 K	Easy to fabricate, poor beam pattern
Facet-mounted horn [68]	1.2 mW (cw)	?	50° FWHM, crude implementation
Hemispherical Si lens [69]	145 mW	160 K	4.8° FWHM (H-plane), diffraction patterns
Micro-TEM horn [70]	?	?	two main radiation lobes
Monolithically integrated horn [81]	25 mW	?	4×11° FWHM
Spoof surface plasmon [71]	1.5 mW	135 K	11.7° × 16° FWHM, Designer spoof SP collimator engraved on QCL facet
2^{nd}-order DFB [71]	39 μW	63 K	6° FWHM (along one axis), surface emission
2^{nd}-order DFB —π-phase shifter [72]	6 mW (cw)	147 K	5° FWHM, single-lobed far-field beam
2^{nd}-order DFB —arrays [82]	1 mW	30 K	10° FWHM (transverse direction)
2^{nd}-order DFB —dual slit [73]	22 mW	?	High power extraction, 40 mW/A slope efficiency
Quasi-periodic DFB [83]	6 mW	?	Asymmetric (Fibonacci sequence), lases at both bandedge modes
Graded photonic heterostructure [80]	103 mW	120 K	230 mW/A slope efficiency, 9 × 20° FWHM Operation on symmetric bandedge mode
Microdisk DFB [84]	250 μW	100 K	No truncated boundaries, Ring-like beam 50 mW/A slope efficiency
Ring resonator DFB —dual slit [85]	10 mW	100 K	25 mW/A slope efficiency, concentric far-field rings
Photonic crystal —BCB tile [86]	300 nW	105 K	very low threshold current density
Photonic crystal —perforated metal [77]	5 mW	95 K	two-lobe radiation pattern
Photonic crystal —deeply etched [78]	2 mW	91 K	surface emission, two-lobe radiation pattern
Photonic crystal [79]	?	62 K	two-lobe radiation pattern, 10 × 10° FWHM
Photonic crystal [87]	300 μW	39 K	CW operation, 10 × 10° FWHM
3^{rd}-order DFB [74]	15 mW	?	10 × 10° FWHM, single-beam low-divergence endfire emission
3^{rd}-order DFB —narrow ridge [75]	1.5 mW (cw)	110 K	150 mW/A slope efficiency, 15 × 18° FWHM
3^{rd}-order DFB [76]	13 mW	?	6 × 11° FWHM, increased DFB length by perfect phase matching
3^{rd}-order DFB —slot antenna [88]	2.5 mW	140 K	4× improvement in output power, 15 × 25° FWHM
Leaky-wave antenna (this work) [89]	200 μW	77K	10° FWHM (E-plane), wideband, steerable beam

frequency or transmission line characteristics.

Apart from beam quality engineering, CRLH transmission-line metamaterial concepts can enable novel functionalities for THz quantum-cascade structures. This includes realization of active terahertz metamaterials with dispersive characteristics not normally achievable by conventional (purely right-handed) metal-metal waveguides/transmission lines, such as left-handed (negative index or "backward wave") propagation where the propagation constant $\beta < 0$ and group and phase velocities are anti-parallel, zero phase shift (infinite wavelength) propagation with uniform phase and amplitude along the line with non-zero group velocity, or full beam scanning from backfire to broadside to forward endfire directions by frequency tuning. Unlike resonant metamaterials such as split-ring resonators, which intrinsically have a narrow bandwidth and high losses [91], left-handed transmission lines are non-resonant, and have a broad bandwidth. Metamaterials are fundamentally different from photonic crystals, as the unit cell in a metamaterial is much smaller than the wavelength ($< \lambda/5$) so that the properties of the metamaterial are refractive (not diffractive) and are determined by the nature of the unit cell (not the periodicity).

1.2.1 Thesis Overview

This thesis presents the design theory, fabrication techniques, and experimental characterization of active terahertz CRLH transmission-line metamaterials realized in quantum-cascade structures with metal-metal waveguide technology. Chapter 2 describes the design and fabrication of operational terahertz quantum-cascade lasers based on resonant-phonon active regions and metal-metal waveguides which served as the foundation for development of terahertz QC-CRLH transmission-line metamaterials. In chapter 3, the theoretical models used to de-

sign the terahertz CRLH transmission-lines are described and their feasibility for use as laser resonators and/or traveling-wave antennas is investigated. Chapter 4 surveys many of the preliminary designs that failed to operate. In chapter 5, an active leaky-wave transmission-line metamaterial antenna fed by a master oscillator terahertz QC-laser is demonstrated which operates in its fast-wave region (right-handed only) and exhibits directive single beam far-field radiation pattern with frequency-dependent direction of radiation. Finally, chapter 6 describes the successful design of a terahertz QC-CRLH transmission-line metamaterial that exhibits left-handed (backward waves or negative index) behavior in addition to conventional right-handed propagation. Future prospects and as well as recommendations for a modified design are also discussed.

CHAPTER 2

Terahertz Quantum-Cascade Lasers

Like any other laser, a THz QC-laser is composed of two integral components: an active (gain) medium and a resonant optical cavity. The purpose of the gain medium —in this case a semiconductor heterostructure— is to provide amplification of radiation via stimulated emission to equalize inherent absorptive losses whereas the the cavity provides electromagnetic mode confinement/feedback to sustain oscillations. Moreover, the cavity determines the ultimate frequency-selectivity properties of the laser.

Treating the laser as a classical oscillator, the oscillation condition is a round trip power gain of unity with accumulated phase of $2\pi \times$ integer. Therefore, the lasing threshold for a particular cavity mode is given by

$$g_{\text{mat}} = \alpha_{\text{mod}}/\Gamma_{\text{mod}} \tag{2.1}$$

where Γ_{mod} is the mode confinement factor and α_{mod} is the modal loss coefficient per unit length determined by the cavity properties. The "available" material gain g_{mat}, however, is proportional to the imaginary part of the dielectric susceptibility of the medium [92], completely independent of the cavity boundary conditions. That is $g_{\text{mat}} = \chi''\omega/n_{\text{bulk}}c$ where $\chi = \chi' + \imath\chi''$ is the complex dielectric susceptibility that accounts for the induced polarization due to intersubband radiative transitions, n_{bulk} is the bulk refractive index of semiconductor and c is

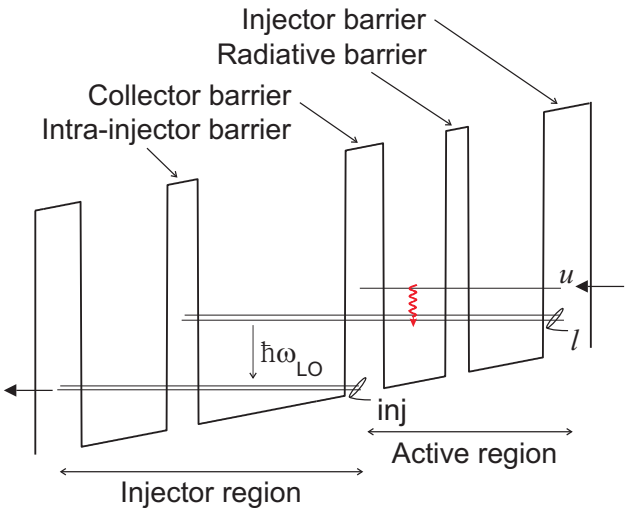

Figure 2.1: Schematic diagram showing one module of the FL designs with four wells per module and LO-phonon depopulation. Each of the four barriers, as labeled in this drawing, play an important role in the optical and electrical characteristics of the QCL.

the velocity of light in vacuum.

This chapter deals with different aspects of Equation (2.1) as relevant to terahertz quantum-cascade lasers. Theoretical background as well as practical considerations for design, fabrication, and characterization of THz quantum-cascade lasers are presented. Terahertz QC-lasers based on resonant-phonon active regions and metal-metal waveguides were demonstrated throughout the course of this thesis which would serve as the foundation for development of active terahertz transmission-line metamaterials.

2.1 Resonant-Phonon Active Regions

The multiple-quantum-well active region designs employed in this thesis were all based on the use of resonant LO-phonon scattering in a three-level system to achieve population inversion between subbands. This type of depopulation

is usually accomplished by placing a third subband (or group of subbands) one LO-phonon energy below the lower radiative state. A schematic overview of the families of designs (referred to as FL series) described in this section is shown in Fig. 2.1. The FL series of devices were originally introduced by Williams *et. al.* [46] which held the record for maximum operating temperature of any THz QCL for quite a while [47]. Sushil Kumar further studied such designs and an extensive discussion on the evolution of FL series is provided in his thesis [61]. FL series of devices are four-well designs with two-well injector and two-well active region per module where resonant tunneling in combination with LO-phonon scattering are used to selectively depopulate the lower radiative state while maintaining a long upper state lifetime. Many of these modules are cascade connected, and when an appropriate electric field is applied, electrons are injected from the previous module into the excited state via resonant tunneling. After transit through the module, the electrons collect in the collector/injector state and are injected into the excited state of the next module. Structures are designed such that THz emission occurs between two radiative states u and l, ($E_{ul} \approx 10-20$ meV), and rapid LO-phonon scattering occurs between lower radiative level and injector state ($E_{li} \approx E_{LO}$). Since $E_{ul} < E_{LO}$ ($E_{LO} = 36.25$ meV in GaAs), LO-phonon scattering is nominally suppressed if the electrons are cold, and one obtains a large lifetime ratio $\frac{\tau_{ul}}{\tau_{li}}$. Ideally, this leads to a population inversion $\Delta n_{ul} > 0$.

Nevertheless, the goal of each design is to maximize bulk gain g_{mat} through optimizing achievable population inversion Δn_{ul} and/or oscillator strength of the radiative transition between the two subbands f_{ul} ($g_{\text{mat}} \propto \Delta n_{ul} f_{ul}$ as discussed in § 1.1.1). Knowledge of the bound state wavefunctions and their eigenenergies for the multiple-quantum-well (MQW) problem is, therefore, required. A one-dimensional Schrödinger solver "Semiconductor Electrostatics by QUantum

AnaLysis" (SEQUAL) was used for all numerical analysis of semiconductor heterostructures in this thesis. SEQUAL was originally written by McLennan and Datta at Purdue University [93] to simulate tunneling-diode types of quantum effect devices. It is a self-consistent numerical solution between Schrödinger equation and Poisson equation. The use of self-consistency is not necessary in this case, however, as for the terahertz QCLs, electron and dopant impurity densities are relatively low and band bending due to space charge effects may safely be neglected. The electronic wavefunctions are computed within the framework of effective mass theory using a slowly-varying envelope function approximation in the MQW growth direction (z). In this treatment the varying material composition is represented by a spatially varying effective mass $m^*(z)$ and the potential $E_c(z)$, which govern the electron energy dispersion in the conduction band and the band edge profile, respectively. In conjunction with an energy dependent effective mass, the 1D Schrödinger equation

$$\left[-\frac{\hbar^2}{2}\frac{d}{dz}\frac{1}{m^*(z)}\frac{d}{dz}+E_c(z)\right]\psi_n(z)=E_n\psi_n(z) \tag{2.2}$$

is numerically solved for bound state wavefunctions ψ_n and eigenenergies E_n using a finite-difference method, where the structure of interest is divided into nodes with position-dependent constant material parameters. Moreover, the conduction band non-parabolicity is neglected due to close proximity of subbands to the conduction band edge (most energies of interest are within an order of 10 meV) with accordingly small in-plane wavevector $\mathbf{k}$ values. Also coupling of electronic wavefunctions in the MQW layers are neglected. This is particularly justifiable for terahertz QCLs due to the close effective mass of electrons in wells and barriers.

In our group we focused on GaAs/$Al_xGa_{1-x}As$ material system with 15% Aluminum content in barriers ($x = 0.15$). The potential barrier height for the

heterostructure was taken to be $\Delta E_c = 0.894x$ eV [94] which corresponds to a 72% band offset, i.e. $\Delta E_c = 0.72\Delta E_g$, where $\Delta E_g = 1.247x$ eV is the difference in the bandgaps of GaAs and $Al_xGa_{1-x}As$ provided $x < 0.45$ [95]. Layer thicknesses are often expressed in the units of one monolayer (ML) which in this material system is equal to half the lattice constant of GaAs once grown on (100) substrates, i.e. $1\text{ML} = a_{\text{GaAs}}/2 = 2.825\text{Å}$.

FL178C

The FL178C design is based around 178 four-well modules which are cascaded to form a 10-μm-thick active region (growth NG-E14315). The conduction band diagrams and the corresponding anticrossing (energy differences) plots of various subband states for FL178C-M7 are shown in Fig. 2.2. The intrawell radiative transition (closely vertical in space) is designed to take place between states $n = 5$ and $n = 4$, with an energy separation of $E_{54} = 11.6$ meV ($\nu \cong 2.9$ THz) and a calculated oscillator strength of $f_{54} = 0.87$. At the design bias (~ 55 mV/module) states $n = 4$ and $n = 3$ are brought into resonance with an anticrossing gap of $\Delta_{34} = 4.06$ meV. The energy separation $E_{32} \approx 34$ meV is designed to be close to LO-phonon energy $E_{\text{LO}} = 36$ meV, enabling fast depopulation of the lower radiative state via LO-phonon scattering into states $n = 2$ and $n = 1$ ($\tau_{4\rightarrow(2,1)} = 0.46$ ps). Electrons collect in the collector/injector anticrossed 2-1 doublet ($\Delta_{21} = 3.9$ meV) where they resonantly tunnel into the upper radiative state $n = 5$ of the next module. Calculated scaled oscillator strength ($f_{i\longrightarrow f} = \frac{m^*}{m_0} f_{i\longrightarrow f,unscaled} = 2m^*(E_f - E_i)\left|z_{i\longrightarrow f}\right|^2/\hbar^2$), and LO-phonon scattering times τ_{LO} in bias space are shown in Fig. 2.2(e) and Fig. 2.2(f), respectively. Electrons lifetime in subband states were evaluated according to scattering rates due to

electron-phonon interactions using Fermi's golden rule:

$$W_{i\longrightarrow f}(\mathbf{k}_i,\mathbf{k}_f)=\frac{2\pi}{\hbar}\left|\langle f,\mathbf{k}_f|H'|i,\mathbf{k}_i\rangle\right|^2\delta(E_f(\mathbf{k}_f)-E_i(\mathbf{k}_i)\pm\hbar\omega_{LO}) \tag{2.3}$$

for an electron initially in state $|i,\mathbf{k}_i\rangle$ (subband i, in-plane wavevector $\mathbf{k}_i$) to the final state $|f,\mathbf{k}_f\rangle$ through an interaction Hamiltonian H'. The total scattering rate from an initial wavevector $\mathbf{k}_i$ can be obtained by integrating Equation (2.3) over all final states $\mathbf{k}_f$ that satisfy the conservation of energy and in-plane momentum, i.e.

$$k_f^2=k_i^2+\frac{2m^*(E_f(0)-E_i(0)\mp\hbar\omega_{LO})}{\hbar^2}, \tag{2.4}$$

$$q_\parallel^2=|\mathbf{k}_i-\mathbf{k}_f|^2=k_i^2+k_f^2-2k_ik_f\cos\theta, \tag{2.5}$$

where the angle θ is the angle between the in-plane wavevectors $\mathbf{k}_i$ and $\mathbf{k}_f$, assuming a parabolic subband dispersion, and $\mathbf{q}_\parallel$ is the in-plane component of the phonon wavevector. After summation over the phonon modes $\mathbf{q}$, the emission rate of an LO-phonon from an initial wavevector is given by [59]:

$$W^{em}_{i\longrightarrow f}(\mathbf{k}_i)=\frac{m^*e^2\omega_{LO}}{8\pi\hbar^2}\left(\frac{1}{\epsilon_\infty}-\frac{1}{\epsilon_{dc}}\right)(n_{\omega_{LO}}+1)\int_0^{2\pi}d\theta B_{i\longrightarrow f}(q_\parallel) \tag{2.6}$$

where the form factor $B_{i\longrightarrow f}$ is given by

$$B_{i\longrightarrow f}=\int_\infty^\infty dz\int_\infty^\infty dz'\psi_f^*(z)\psi_i(z)\psi_i^*(z')\psi_f(z')\frac{1}{q_\parallel}e^{-q_\parallel|z-z'|}. \tag{2.7}$$

and the Fröhlich interaction strength for electron-polar-optical-phonon scattering is assumed. ϵ_{dc} and ϵ_∞ are the static and high frequency permittivities, and $n_{\omega_{LO}}$ is the Bose-Einstein occupation. The total scattering time between two subbands $\tau_{i\longrightarrow f}$ can be obtained by averaging over all possible initial states $\mathbf{k}_i$ in the subband. Whenever the transition energy $E_{fi}<E_{LO}$, however, the approxi-

mate thermally activated expression $\frac{1}{\tau_{i\longrightarrow f}} \approx W_{i\longrightarrow f}^{(hot)} \exp\left(\frac{E_{fi}-E_{LO}}{K_B T_e}\right)$ has been used where $W_{i\longrightarrow f}^{(hot)}$ is the scattering rate at the lowest energy E_k in the subband where LO-phonon scattering is energetically allowed and T_e is the electron temperature [59]. At the design bias, a large lifetime ratio is obtained $\frac{\tau_5}{\tau_4} = 18.5$ which is the requirement for population inversion. Moreover, the oscillator strength of the $5 \rightarrow 4$ transition reaches its maximum. Selective depopulation of the lower radiative state $n = 4$ is insured by a large $\frac{f_{43}}{f_{53}}$ ratio.

A major goal of terahertz QCL design is to minimize injection of carriers into lower energy subbands at fields applied below the design bias. Such "parasitic current channels" can undesirably increase the threshold current density, and consequently decrease the laser dynamic range. In severe cases, when the parasitic current is stronger than the design bias current, an early negative differential resistance (NDR) can occur which causes current instability and prevents the device from reaching the design bias [96]. For this design, two dominant parasitic current channels corresponding to coupling of the injector states $n = 1^{'}$ and $n = 2^{'}$ to the phonon-depopulation state $n = 3$ are shown in Fig. 2.2. The parasitic bias condition of 31 mV/module is shown in Fig. 2.2(c), where level $2'$ is in resonance with the upper LO-phonon resonant state of the injector wells (level 3) in the next module. The parasitic bias condition of 39 mV/module shown in Fig. 2.2(d) corresponds to $1' - 3$ alignment. Such an alignment constitutes a strong parasitic current channel due to very fast LO phonon scattering from level 3 to 2 and 1 ($E_{32} \approx 32 - 39$ meV). In order to reduce the current conduction at such low biases one needs to reduce the coupling between the injector ground state(s) and the upper LO-phonon resonant state by adding more wells to the active or injector regions, or alternatively increase the thickness of the barriers between those states [97, 98].

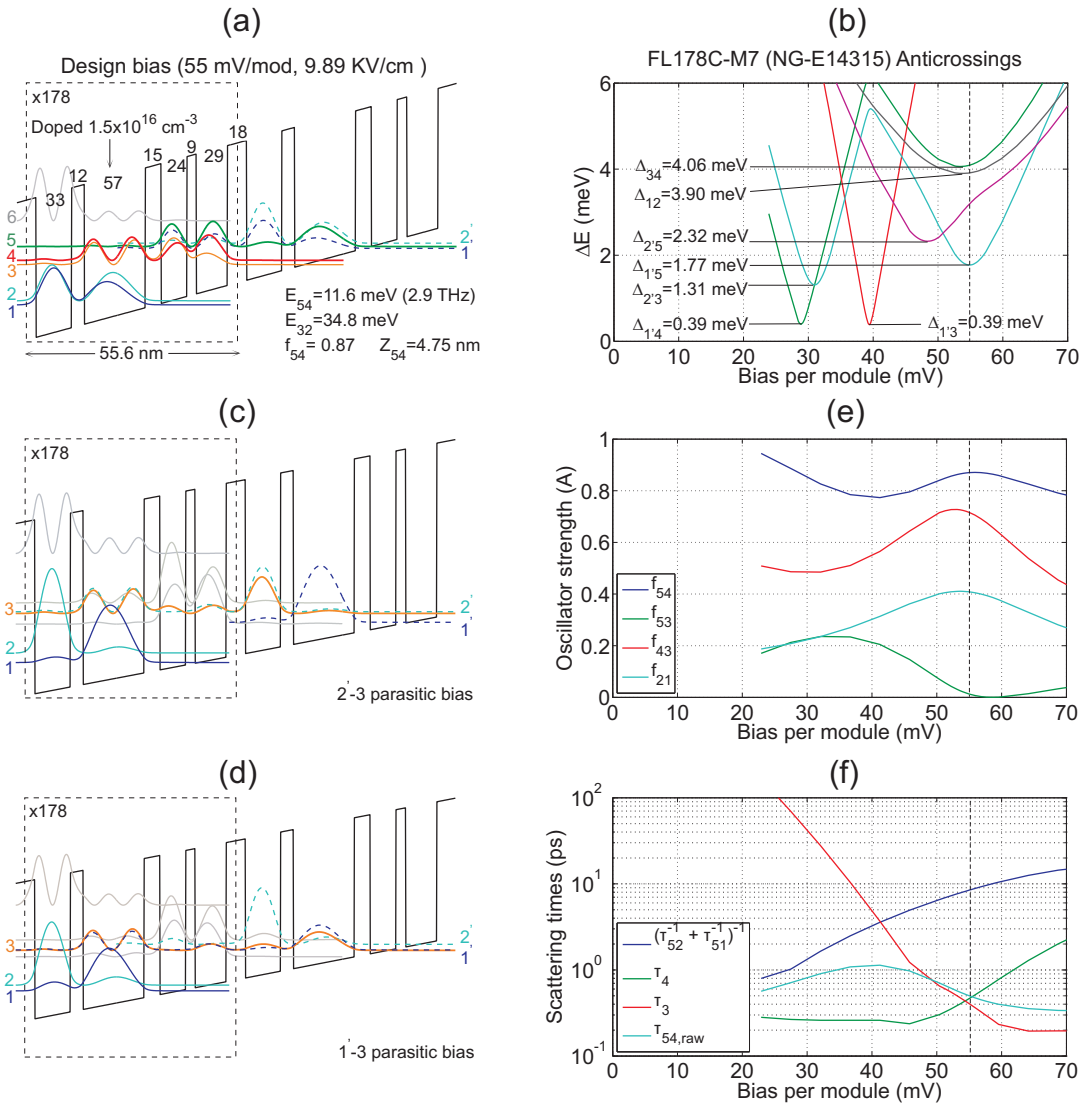

Figure 2.2: (a) Conduction band diagram at the design bias and (b) anticrossing plots for the design FL178C-M7. Square amplitude of the subband states wavefunctions and their eigenenergy differences are calculated based on a two-module simulation. (c),(d) Two dominant (lower-level) parasitic current channels corresponding to the $2^{'} \rightarrow 3$ and $1^{'} \rightarrow 3$ transport, respectively. (e),(f) Intersubband oscillator strengths and scattering times in bias space.

FL177Q

The FL177Q design is based around 177 repeats of 56-nm-thick modules to form a 10-μm-thick active region (growth NG-E14317). FL177Q was designed to be identical to FL178C, except with a 10 ML (28.3 Å) radiative barrier instead of a 9 ML (25.4 Å) radiative barrier. Since E_{54} depends strongly on the radiative barrier thickness, the center frequency of the gain bandwidth can be significantly changed by varying the thickness of the radiative barrier. Thickening the radiative barrier by 1 ML results in THz emission close to 2.5 THz ($E_{54} \approx 10$ meV). The conduction band diagram and the levels anticrossings for FL177Q-M11 are shown in Fig. 2.3(a), (b). While no significant change in Δ_{34} and Δ_{21} is observed compared to FL178C-M7, the 4-3 anticrossing is now in worse alignment with the 1′-5 design bias. The injection anticrossing was $\Delta_{1'5} = 1.58$ meV.

FL86Q

The FL86Q design was a redesign of the FL177Q in which the intra-injector barrier thickness was increased from 12 ML (33.9 Å) to 14 ML (39.6 Å). This made the injector doublet $1^{'}$-$2^{'}$ "tighter" as characterized by a smaller anticrossing energy Δ_{12}. As a result, the $1^{'}$-5 injection as well as $1^{'}$-3 parasitic anticrossings were also reduced ($\Delta_{1'5} = 1.48$ meV and $\Delta_{1'3} = 0.37$ meV). This should decrease the conduction of parasitic currents at biases below the design bias and consequntly lower the threshold due to minimized coupling between levels 1'-2' and 3 in this two-well injector design by preventing the injector states from aligning to form a doublet (or a miniband) until beyond the parasitic bias [99]. 86 modules of the FL86Q design were cascaded to form a 5-μm-thick active region (growth NG-B17952) for use in fabrication of metamaterial devices. The widest well of each module is doped with Si to $1.2\times10^{16}\text{cm}^{-3}$ as opposed to $1.5\times10^{16}\text{cm}^{-3}$ in

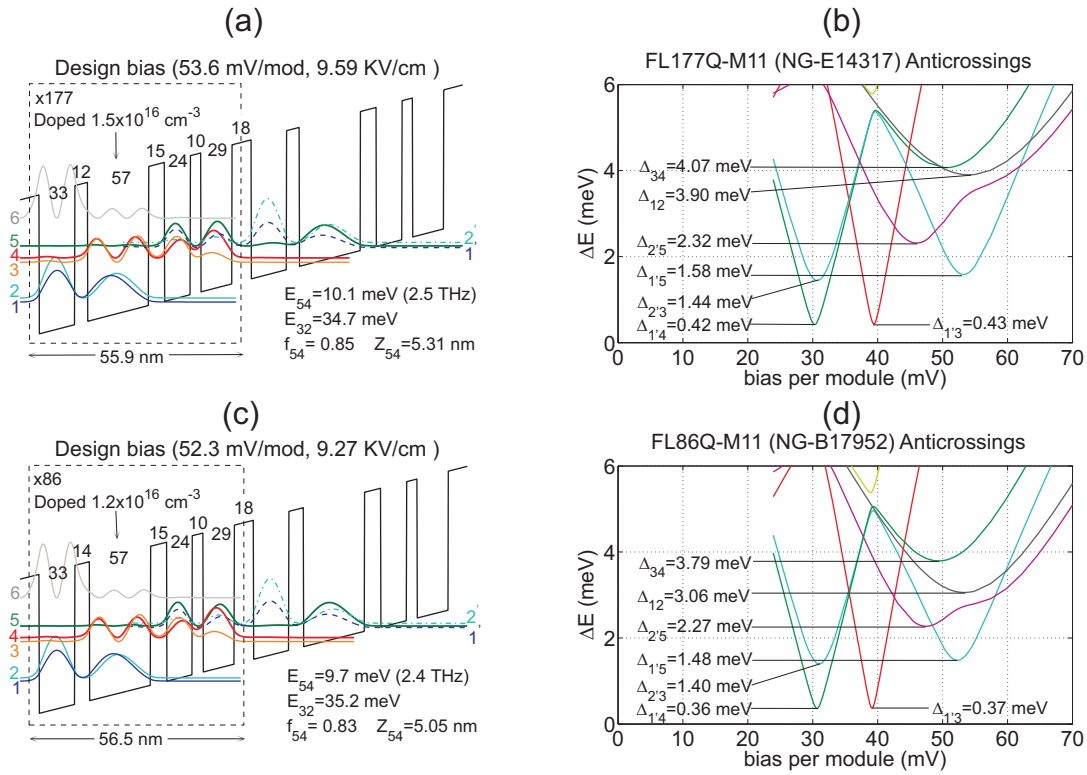

Figure 2.3: (a),(b) Conduction band diagram at the design bias and levels anticrossing plots for the design FL177Q-M11, and (c),(d) conduction band diagram at the design bias and levels anticrossing plots for the design FL86Q-M11. The radiative transition is from $5 \rightarrow 4$.

FL177Q design to reduce the contribution of free carriers to waveguide losses.

The aforementioned designs were epitaxially grown on (100) semi-insulating GaAs substrates using an MBE machine dedicated to GaAs/$Al_xGa_{1-x}As$ material system. All growths were performed by Dr. Qi-Sheng Chen of Northrop Grumman Aerospace Systems (NGAS) at Redondo Beach, CA. QC material was then processed in metal-metal waveguides for electrical and optical characterization. Table 2.1 summarizes critical parameters of the three active region designs presented in this section.

Table 2.1: Comparison of critical parameters for THz QCL active region designs

Design	FL178C-M7	FL177Q-M11	FL86Q-M11
E_{54} (meV)	11.6	10.1	9.70
E_{32} (meV)	34.8	34.7	35.2
f_{54}	0.87	0.85	0.83
$\Delta_{1'5}^{(inj)}$ (meV)	1.77	1.58	1.48
Δ_{43} (meV)	4.06	4.07	3.79
Δ_{21} (meV)	3.90	3.90	3.06
$\Delta_{1'3}^{(para)}$ (meV)	0.39	0.43	0.37
$\Delta_{2'3}^{(para)}$ (meV)	1.31	1.44	1.40
$\tau_{5\longrightarrow 2,1}$ (ps)	8.5	5.7	5.3
$\tau_{4\longrightarrow 2,1}$ (ps)	0.45	0.35	0.34
$\tau_{3\longrightarrow 2,1}$ (ps)	0.4	0.6	0.5
$\tau_{54}^{(raw)}$ (ps)	0.5	0.6	0.66

2.2 Metal-Metal Waveguides

While the initial demonstration of terahertz quantum-cascade lasers was done with the aid of a single-plasmon waveguiding scheme [33], the use of double-plasmon metal-metal waveguides [57] has proved critical for higher operating temperatures both in pulsed ($\sim$ 200 K) [42] and cw (117 K) [47] operation. This is due to the lower waveguide loss in metal-metal waveguides and high confinement of the mode to the active gain material which is sandwiched between metal cladding layers. Metal-metal waveguides preserve such characteristics even for very narrow ridges which makes them an excellent testbed for exploration of deep subwavelength lasers and transmission lines in the terahertz. Indeed such a waveguide is similar in concept to microwave microstrip transmission line albeit with distributed photonic gain within the dielectric.

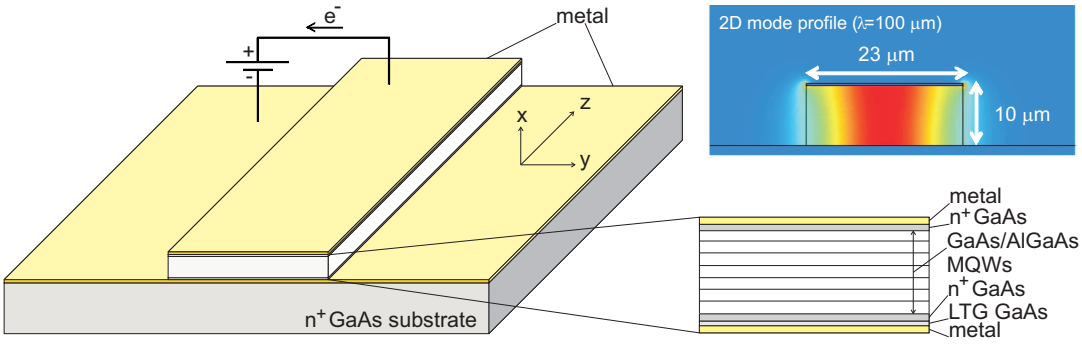

Figure 2.4: Schematic diagram showing a terahertz QCL with MM waveguide. A simulated 2D mode profile for an infinite ridge is shown in the upper right. The MBE growth sequence (from top to bottom) is indicated showing the highly-doped n^+ GaAs contact layers (typically doped to $\sim 5 \times 10^{18}\text{cm}^{-3}$) and a thin (35Å) low-temperature (250°C) grown (LTG) GaAs layer with midgap defect states which assists in low-resistance contact. Two metal clads provide mode confinement in the growth direction which would also serve as electrical contacts to the device.

2.2.1 Modeling and Design

Figure 2.4 shows the schematic of a terahertz QCL with Fabry-Pérot MM waveguide along with a two-dimensional (2D) mode profile. The metal-metal waveguide modes are indeed double surface-plasmon (SP) electromagnetic waves where the fields are bound to two metal cladding layers on either side. Surface-plasmon waves are electromagnetic waves supported at the interface of two dielectric media with finite conductivities associated with collective surface charge oscillations at the interface. SP electromagnetic modes are a set of solutions to the Maxwell's equations with transverse-magnetic (TM) polarization where field amplitudes peak at the interface and decay exponentially with distance from the interface into each of the media. The electromagnetic energy of a SP mode propagates along the interface and is said to be bound to the regions close to the interface, namely referred to as extinction length of the mode in each medium. The real part of the dielectric constants on either side of the interface has to

have opposite signs for the SP mode to exist. This condition can be satisfied at the interface of a highly conducting layer (such as a metal or a highly doped semiconductor) and a dielectric medium (such as a low-doped semiconductor, an insulator, or air).

2D Mode Solver

When dealing with metal-metal waveguides with subwavelength transverse dimensions, a two-dimensional (2D) mode solver is necessary. A 2D finite-element electromagnetic mode solver (COMSOL) was employed in this thesis for numerical calculation of waveguide losses. Figure 2.5 shows the effect of varying the MM waveguide ridge width w and/or height h on modal loss, mode confinement factor, effective phase index, and threshold gain values (Equation 2.1) for the fundamental (TM_{00}) and first higher-order (TM_{01}) lateral modes of the waveguide. Modal loss and effective index are related to the complex mode propagation wavevector k_z via $\alpha = 2\Im\{k_z\}$ and $n_{\text{eff}} = \Re\{k_z\}c/\omega$, respectively. First we note that α varies as $1/h$ as the epitaxial growth thickness is varied from 3-10 μm. This is due to the fact that at terahertz frequencies the extinction length of the SP mode in the semiconductor is much larger than in metal and the mode almost uniformly fills the semiconductor region. As a result any reduction in semiconductor thickness increases the fraction of mode overlap with metal, and proportionately the propagation loss α. For a given height, g_{th} monotonically increases as the width of the metal-metal waveguide decreases. This is accompanied by a reduction in effective mode index n_{eff} as well as 2D mode confinement factor $\Gamma_{\text{2D,mod}}$. Γ_{2D} is defined as:

$$\Gamma_{\text{2D,mod}} = \frac{n_{\text{g}}}{n_{\text{A}}} \frac{\int_{\text{act}} |E_x|^2 ds}{\int_{-\infty}^{+\infty} |\vec{E}|^2 ds} \tag{2.8}$$

which is a measure of the spatial overlap of the electromagnetic mode energy density with active QC gain material weighted by its confinement in time, i.e. the ratio of the group index n_{g} to the bulk GaAs refractive index n_{A}. This form of confinement factor accounts for dispersion of the guided mode and can be greater than unity if the group index is larger than the bulk refractive index in our metal-metal waveguide. The first term can be thought of as a confinement in time since increasing the real part of the group index ($n_{\mathrm{g}} = c/v_{\mathrm{g}}$) relative to the bulk index has the effect of slowing the propagation of the guided mode. Therefore for a given waveguide length, light can interact longer with the gain medium resulting in an enhancement of the modal gain per unit length [100].

For the sake of these simulations QC material was modeled as bulk lossless GaAs whereas contribution of "free" electrons to the complex relative permittivity of top and bottom conductors were incorporated according to Drude model [101]

$$\begin{aligned} \epsilon_{\mathrm{r}} &= \epsilon_{\mathrm{core}} + \imath \frac{ne^2\tau}{\epsilon_0 \omega m^* (1 - \imath\omega\tau)} \\ &= \epsilon_{\mathrm{core}} \left(1 - \frac{\omega_{\mathrm{p}}^2 \tau^2}{1 + \omega^2\tau^2} + \imath \frac{\omega_{\mathrm{p}}^2 \tau}{\omega(1 + \omega^2\tau^2)} \right) \end{aligned} \tag{2.9}$$

where ϵ_{core} is the background relative permittivity of the conducting material excluding the contribution of free electrons, m^* is the effective mass of electron, n is the electron density, τ is the Drude relaxation time for electrons, ω is the radian frequency of the electromagnetic wave, and ω_{p} is the plasma frequency of the conducting medium ($\omega_{\mathrm{p}}^2 = \frac{ne^2}{\epsilon_0 \epsilon_{\mathrm{core}} m^*}$). Plasma frequency for most metals is in the ultraviolet. For instance, for Au $\omega_{\mathrm{p}}/2\pi \sim 2000$ THz and for highly-doped GaAs ($n \sim 5 \times 10^{18}\mathrm{cm}^{-3}$) $\omega_{\mathrm{p}}/2\pi \sim 20$ THz. Below the plasmon frequency, $\Re\{\epsilon_{\mathrm{r}} < 0\}$ and therefore a surface plasmon mode can propagate at the interface. Also note that the effect of any doped contact layer is neglected in these calculations since

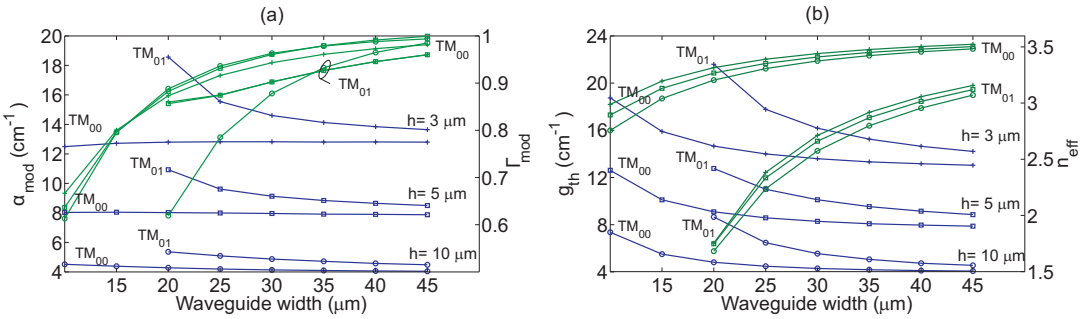

Figure 2.5: (a) Calculated modal loss (blue curves) and confinement factor (green curves), and (b) threshold gain value (blue curves) and effective mode index (green curves) at $\omega/2\pi = 2.7$ THz for metal-metal waveguide ridges of various width and heights. Calculations are solely due to free-carrier losses using a Drude model (equation 2.9) with the QC gain material modeled as bulk lossless GaAs with $\epsilon_{\text{GaAs}} = 12.9$ and Au metal claddings were considered with $n = 5.9 \times 10^{22}\text{cm}^{-3}$, $\tau = 60$ fs, $m^* = m_0$, $\epsilon_{\text{core}} = 1$ for the Drude parameters [103].

their contribution to the overall waveguide losses is an order of magnitude smaller as long as they are not exposed on the sides [59, 102].

2.2.2 Fabrication

Metal-metal waveguides advocate a very low-loss waveguiding scheme in the terahertz. However, fabrication of such waveguides is a challenging task which involves flip-chip wafer bonding followed by substrate removal of the MBE growth. In what follows I will provide a brief description of metal-metal waveguide processing. Chapter 5 of Williams [59] describes the fabrication procedure in detail. This process is standard for fabrication of Fabry-Pérot cavity metal-metal waveguides with cleaved facets and is followed throughout this thesis unless otherwise noted. All waveguide fabrication steps were performed at UCLA nano research facility. MBE-grown wafers as well as n^+ GaAs receptor substrate wafers are cleaved in 1 cm^2 pieces, metal coated (typically Ta/Cu::30/300 nm) in e-beam evaporator, and aligned and bonded in a Karlsuss SB6 wafer bonder. The Ta

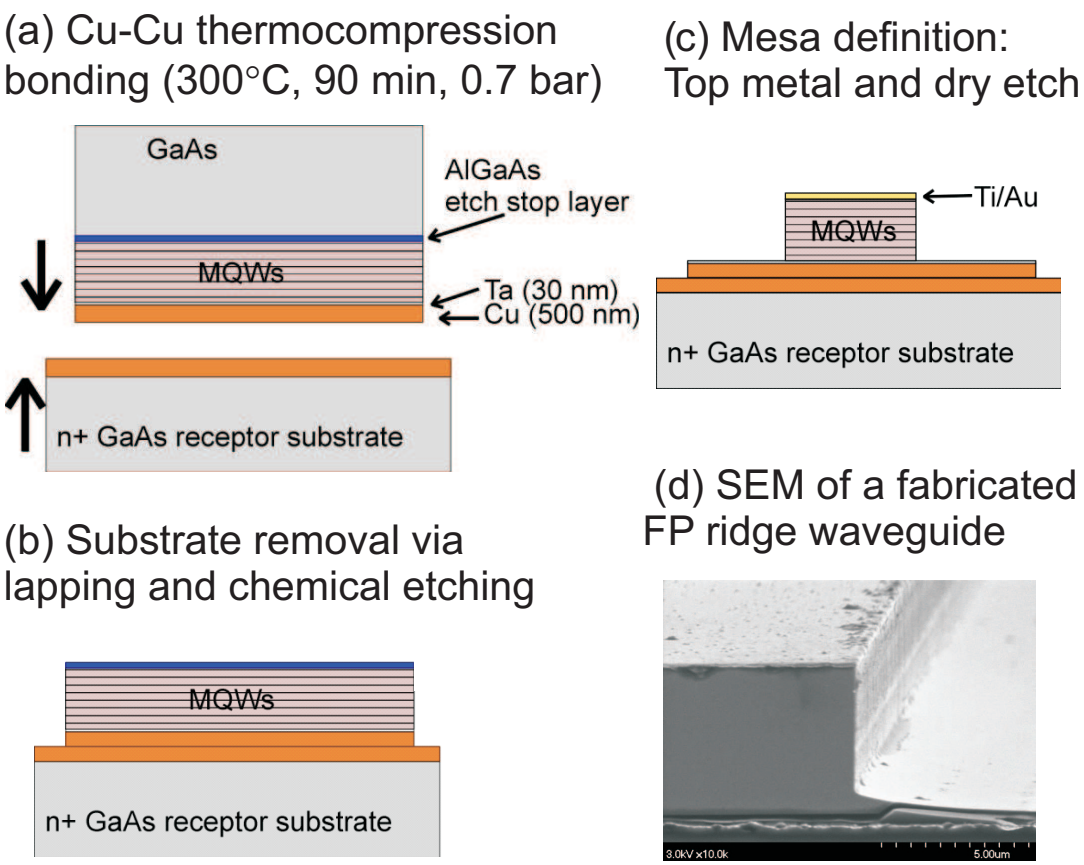

Figure 2.6: Fabrication process for terahertz QCLs with metal-metal waveguides based on Cu-Cu bonding technique. A scanning electron microscope (SEM) image of a cleaved facet from a Fabry-Pérot ridge waveguide is also shown. Active region is 5 μm-thick. Device is NG-B17952.

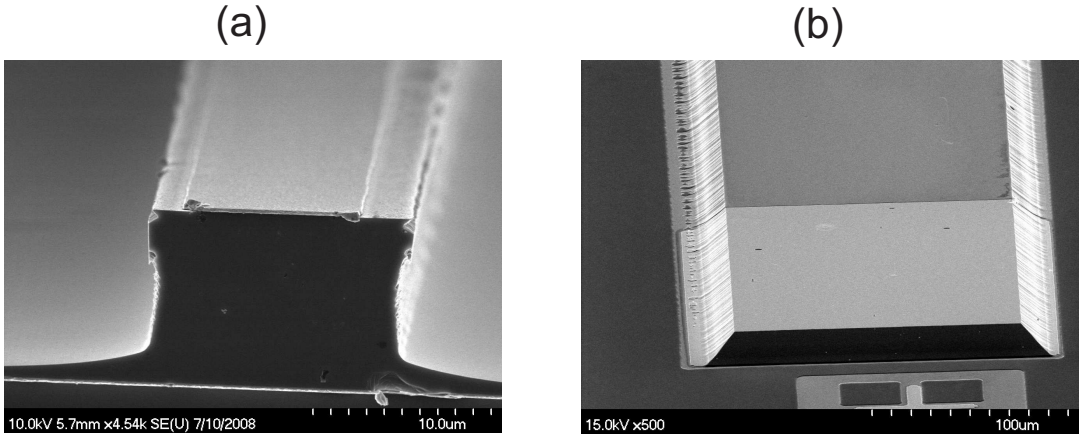

Figure 2.7: SEM images of typical metal-metal waveguide ridges fabricated by Cu-Cu bonding and (a) dry etching in BCl_3:Cl_2 (60:30 sccm) (device is NG-E14315), and (b) wet etching by H_3PO_4:H_2O_2:H_2O (10:10:250) (device is NG-E14317). Active regions are 10-μm thick.

layer serves both as adhesion layer and diffusion barrier of Cu into GaAs. A short (less than 15 seconds) buffer oxide etch (BOE) was normally performed right before evaporation of the Ta/Cu layer to remove any native oxide from the surface of the GaAs/AlGaAs epilayer. Thermocompression wafer bonding was performed in vacuum at a temperature of 300°C and under a tool pressure of 0.7 bar for 90 mins. A post-bond anneal was also carried out in purged nitrogen at 300°C for 30 min to relax any strain in the copper layer.

Following the Cu-Cu wafer to wafer bonding, the GaAs substrate on the MBE-grown wafer is removed by a combination of mechanical lapping (down to a total thickness of $\sim$ 50 μm) and chemical polishing using an Ammonium hydroxide and hydrogen peroxide solution (NH_4OH:H_2O_2::1:19). This etchant has extreme selectivity on $Al_xGa_{1-x}As$ ($x \leq 0.4$) and practically stops at the $Al_{0.55}Ga_{0.45}As$ layer. The etch-stop $Al_{0.55}Ga_{0.45}As$ layer is subsequently removed in HF acid (approximately one minute) which leaves behind a 5-10 μm epitaxial layer with a shiny surface. A short clean-up etch in dilute peroxide ammonia (PA) solu-

tion (NH_4OH:H_2O_2:H_2O:5:3:490) is usually performed after this step to (partially) remove the highly-doped GaAs top contact layer buried underneath the $Al_{0.55}Ga_{0.45}As$ etch-stop layer in the MBE growth sequence. The PA solution has an etch rate of 100-150 nm/min depending on the solution age. After this step the epitaxial layer is ready to be processed in waveguide mesas of various widths using dry or wet etching techniques.

During the initial development phase of the metal-metal waveguide devices, Ti/Au top metal contacts were evaporated using lift-off technique and mesas were defined in an ICP-RIE dry etcher in a BCl_3:Cl_2::60:30 sccm gaseous plasma using thick ($\sim 1\mu$m) oxide masks. This method requires two photolithography steps which allows fabricating very wide MM waveguides ridges with single lateral mode by exposing the top highly-doped layer on the sides [102]. However, it turned out that the etch recipe was not optimized which resulted in severe undercut and roughness in mesa sidewalls (see Fig. 2.7(a)). As of November 2009, Ti/Au/Ni top metal contacts were evaporated with Ni used as self-aligned dry etch mask. Mesas were then defined in BCl_3 only gaseous plasma which yielded much smoother sidewalls of $\sim 90^\circ$ slope (Fig. 2.6). Occasionally, mesa definition was performed using wet chemical etching. Ti/Au metal contacts were evaporated first and a diluted Phosphoric acid and Hydrogen Peroxide solution (H_3PO_4:H_2O_2:H_2O::10:10:250) was used with a photoresist mask (Shipley SPR770) to etch waveguide mesas with very smooth sidewalls. The etch profile, however, is a $45-60^\circ$ slant as can be seen in Fig. 2.7(b). Once mesas are defined, Ti/Au back metal contact is evaporated on the backside of the wafers. At this stage wafers are cleaved into pieces of desired length to obtain Fabry-Pérot cavities.

2.3 Experimental Results

For testing, devices were indium soldered onto a copper chip carrier and mounted on the cold stage of a cryostat. The electrical and optical behavior of devices were characterized by performing current-voltage ($I-V$) and light intensity-current ($L-I$) measurements. All measurements were performed in vacuum at cryogenic temperatures using Infra-Red Laboratories (IR Labs) emission dewar. The dewar output window was a 0.25-mm-thick polypropylene sheet (2.0-inch diameter) with $80-90\%$ transmissivity in the $1-5$ THz range. Electrical contacts were made from a bonding pad mounted on the chip carrier to lasers with aluminum or gold wire bonds. Electrical bias was provided by a pulse generator from Agilent (model 8114A). Current was measured using a inductive current sensing loop for fast pulsed measurements, and in some cases, using current-sensing resistors for long pulsed measurements. Continuous-wave measurements were performed using a Keithley 2400/2420 sourcemeter. Pulsed measurements were taken using calibrated boxcar averagers, and the data was collected electronically using LabView.

A liquid-helium (LHe) cooled Ge:Ga photodetector, also from IR Labs, was normally used for face-to-face optical characterizations. $L-I$ Measurements were usually performed in pulsed mode and lock-in detection (using SR830 lock-in amplifier from Stanford Research Systems) was used to reduce the noise bandwidth. Calibrated power measurements were performed using an S310 AC2500-H Scientech Calorimeter (Thermopile). Far-field beam pattern measurements were performed using a broadband P4-42 pyroelectric detector from Coherent Molectron. If needed, however, 1D cuts of beam patterns were taken using the Ge photodetector. Radiation spectrum of lasers were measured with the aid of a Nicolet 8700 Fourier-Transform Infra-Red (FTIR) spectrometer. The heart of the FTIR

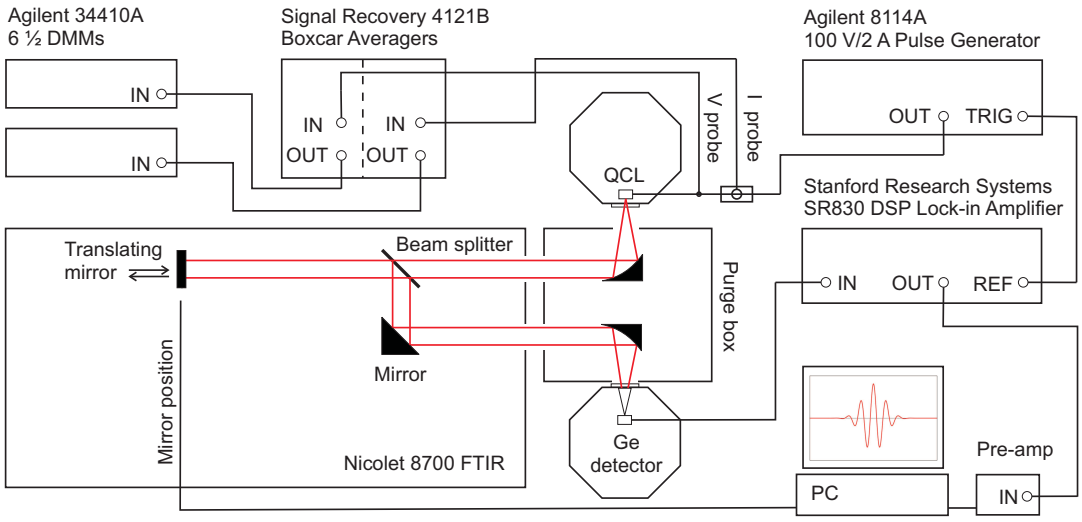

Figure 2.8: Experimental setup.

consists of a Michelson interferometer that traces out an interferogram, which is Fourier transformed to yield the power spectrum of the emitted radiation. Laser emission spectrum measurements were performed using the Nicolet far-infrared "Solid Substrate" beam splitter with the FTIR operated in linear-scan mode (typically with a 0.158 cm/sec mirror velocity), where the moving mirror of the Michelson interferometer translates smoothly. Figure 2.8 details the experimental setup for emission measurements.

NG-E14315 (design FL178C-M7)

We obtained lasing from a terahertz QCL for the first time on July 18, 2008 from the wafer labeled NG-E14315 (based on the design FL178C-M7) that was processed with Cu-Cu MM waveguides. The experimental results for NG-E14315 are summarized in Fig. 2.9. Devices were tested for both pulsed and continuous-wave (cw) operation. THz power was detectable up to a heatsink temperature of $T_{\mathrm{max,pulsed}} = 120$ K in the pulsed mode with the frequency of radiation measured at 3.08 THz corresponding to a photon energy of 12.32 meV, close to the

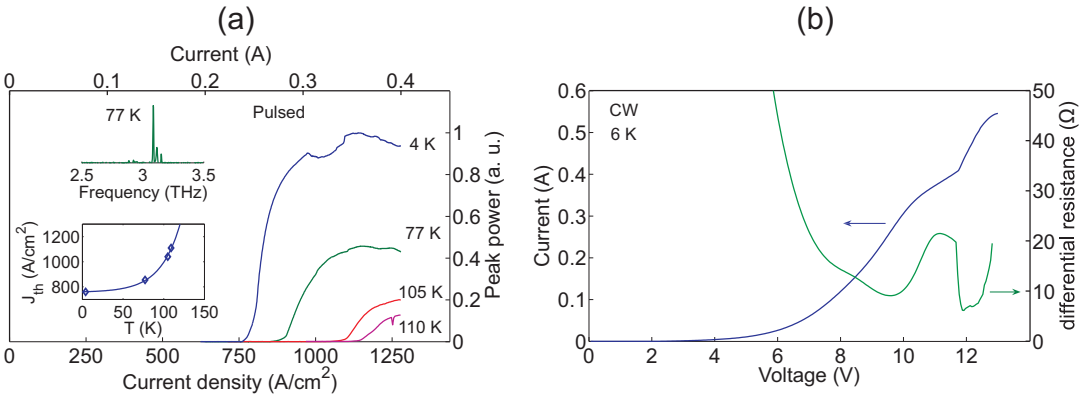

Figure 2.9: (a) Pulsed $L-I$ characteristics measured from a NG-E14315 MM (Cu-Cu) Fabry-Pérot laser ridge of dimensions 46 μm×700 μm with cleaved facets, and (b) cw $I-V$ characteristics measured from a Fabry-Pérot laser ridge of dimensions 46 μm×1.1 mm with cleaved facets. The $L-I$s were recorded using a LHe-cooled Ge:Ga photodetector and device was biased with 200-ns-long pulses of repetition frequency (PRF) 1 KHz (duty cycle= 0.02%). Typical pulsed spectrum at 77 K for bias currents close to maximum optical power $J_{\max}$ is shown in the inset of plot (a).

calculated value of 11.6 meV. Lasing threshold was also observed in cw operation accompanied by a step change in device differential resistance $R = \frac{\mathrm{d}V}{\mathrm{d}I}$ which is caused by the reduction of the upper state lifetime due to the onset of stimulated emission. Nevertheless, no signs of lasing in cw mode were observed above liquid nitrogen temperature. While this initial demonstration did not break any records in $T_{\max}$ or J_{th} of THz QCLs, it was still a milestone for our lab. The threshold current density was 760 A/cm^2 and continued to increase with temperature (see Fig. 2.9(a) inset). This is believed to be caused by the reduction of the upper state lifetime due to thermally activated LO-phonon scattering. A phenomenological fit $J_{\mathrm{th}} \propto \exp(T/T_0)$ often used to characterize this temperature dependance in terms of a figure of merit T_0 is also indicated with $T_0 = 24.5$ K.

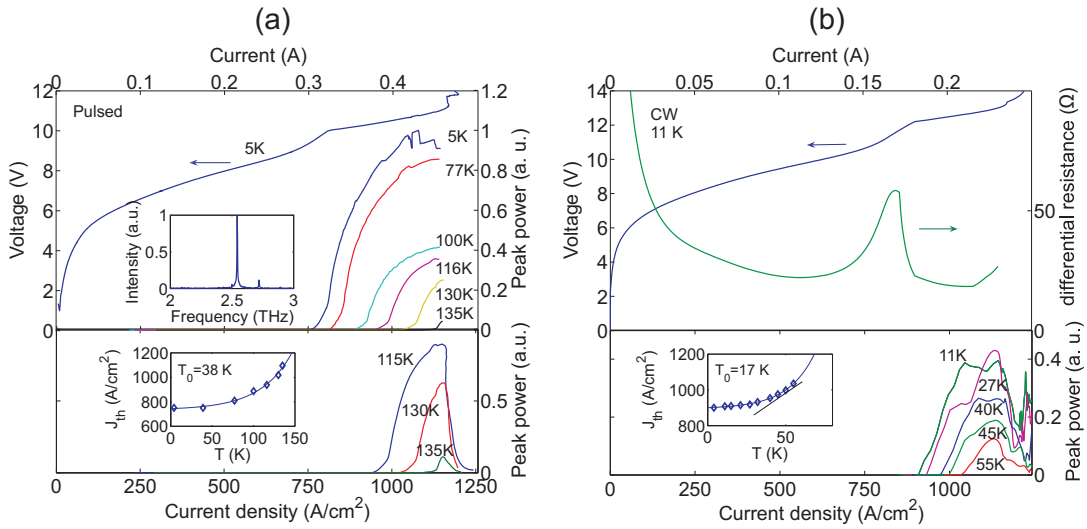

Figure 2.10: (a) Pulsed (duty cycle $< 0.05\%$) $L-I$ and $I-V$ characteristics measured from a NG-E14317 MM (Cu-Cu) Fabry-Pérot laser ridge of dimensions 46 μm$\times$865 μm with cleaved facets, and (b) cw $L-I$ and $I-V$ characteristics measured from a Fabry-Pérot laser ridge of dimensions 36 μm$\times$560 μm with cleaved facets. The temperature-dependant $L-I$s in the lower panel were recorded using a He-cooled Ge:Ga photodetector. Typical pulsed spectrum at 5 K is shown in the inset of plot (a).

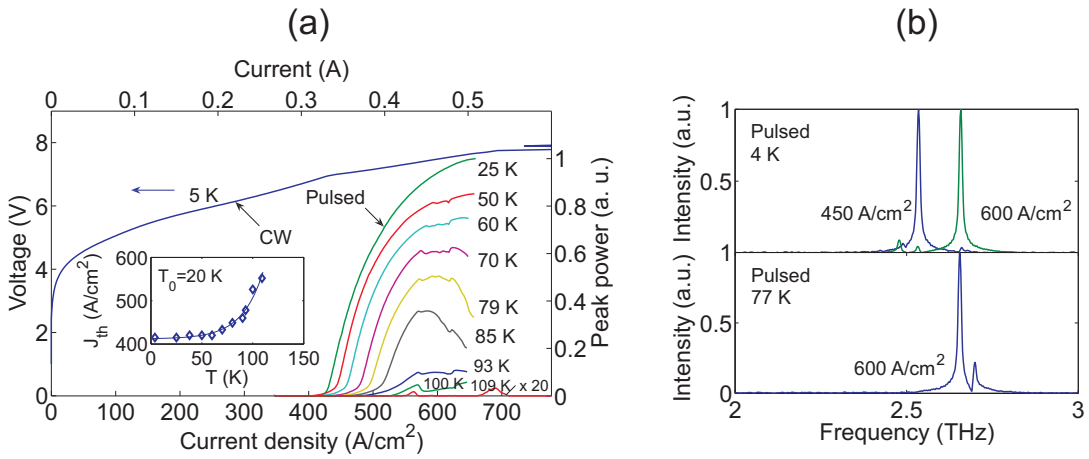

Figure 2.11: Experimental results for NG-B17952 measured from a MM (Cu-Cu) Fabry-Pérot laser ridge of dimensions 76 μm$\times$1.02 mm with cleaved facets. Pulsed $L-I$s were recorded using a He-cooled Ge:Ga photodetector and the device biased with pulses of 10 KHz PRF and 200 ns duration (0.2% duty cycle).

NG-E14317 (design FL177Q-M11)

The NG-E14317 growth was based on FL177Q-M11 designed to operate close to $\lambda = 120\mu$m. Terahertz QC-lasers with metal-metal waveguides (Cu-Cu) were demonstrated from this wafer that operated both in pulsed mode ($T_{\mathrm{max,pulsed}} =$ 136 K) and cw mode ($T_{\mathrm{max,cw}} = 56$ K). At liquid nitrogen temperature, lasing was observed in pulsed operation only with pulses of up to 75% duty cycle. The experimental data for NG-E14317 is reported in Fig. 2.10. Measured spectrum at 10 K indicates the QCL operation at 2.55 THz ($\lambda = 117\mu$m).

NG-B17952 (design FL86Q-M11)

The 5-μm-thick active material NG-B17952 was grown based on the design FL86Q-M11 and processed for metal-metal waveguides (Cu-Cu waferbond) with dry-etched ridges. Figure 2.11(a) shows the temperature-dependant LIV characteristics and spectrum of radiation for pulsed operation. THz power was detectable

up to a heatsink temperature of $T_{\max,\text{pulsed}} = 110$ K and lasing threshold was observed at 5 K for cw operation. The threshold current density at 5 K was 420 A/cm^2 significantly lower than that of the growth NG-E14317. Typical spectra measured at 4 K and 77 K are plotted in Fig. 2.11(b) which show a blue shift with increasing bias. This is due to the Stark shift of the intersubband gain versus voltage in such structures.

2.4 Horn Antennas for THz QC-Lasers

For a MM waveguide terahertz QC-laser operating in its fundamental mode, the facets are the primary source of laser emission, even for laser cavities with sub-wavelength dimensions and substantial evanescent field in the air. This leaves conventional cleaved-facet Fabry-Pérot ridge cavities with a highly divergent beam pattern, characterized by concentric rings in the far-field [65, 67]. The poor outcoupling of the terahertz power and non-directional beam patterns are attributed to radiation through a subwavelength aperture. Far-field rings in the beam pattern are deemed to originate from the interference of the facets, i.e. two dipole sources separated by distance ℓ (ℓ being the cavity length). For the rest of this chapter, I will focus on the integration of a micromachined horn antenna with MM waveguide terahertz QCLs that could potentially address both issues. The purpose of this study is to investigate achievable improvement in outcoupled power and beam quality of terahertz QC-lasers without paying too much penalty in loss (or equivalently threshold current) and/or maximum operating temperature of Fabry-Pérot MM waveguides. A micromachined horn antenna provides a smooth transition from a subwavelength (in vertical dimensions) metal-metal waveguide to a large radiating aperture (multiples of lambda). Once abutted at the facet of the QCL, the horn acts as an impedance transformer, matching the

impedance of the guided terahertz mode to that of the free-space propagating mode. One advantage of this approach compared to resonant DFB structures is that scalar horns are inherently broadband and not tailored for a specific frequency or design. As a result, mode matching (or equivalently reducing facet reflectivity) can be obtained over a much wider bandwidth. Moreover, the radiating aperture of the horn can, in principle, be made desirably large enough to launch highly directive Gaussian beams even from metal-metal waveguides with subwavelength transverse dimensions.

Section 2.4.1 presents a monolithic fabrication process for pyramidal horn antennas realizable in silicon by a combination of dry- and wet-etch microfabrication techniques. The performance of terahertz QC-lasers with integrated horn antennas were evaluated both theoretically and experimentally. Finite element simulations were performed to estimate achievable power enhancement using this approach. Experimental results including absolute power and far-field beam pattern measurements are presented in section 2.4.2.

2.4.1 Horn Micromachining

Bulk micromachining has traditionally been used for patterning three-dimensional micro-electro-mechanical systems (MEMS) in Silicon [104]. Sub-millimeter wave range of electromagnetic spectrum has particularly benefited from such well-established microfabrication techniques for manufacturing of passive terahertz components where conventional machining techniques proved costly or inadequate [105, 106]. Extensively used in sub-millimeter systems are hollow rectangular and diamond waveguides [107], and diagonal horn antennas [108, 109] realized by wet anisotropic etching of silicon. Octagonal antenna designs have been demonstrated by employing a combination of wet etching techniques and

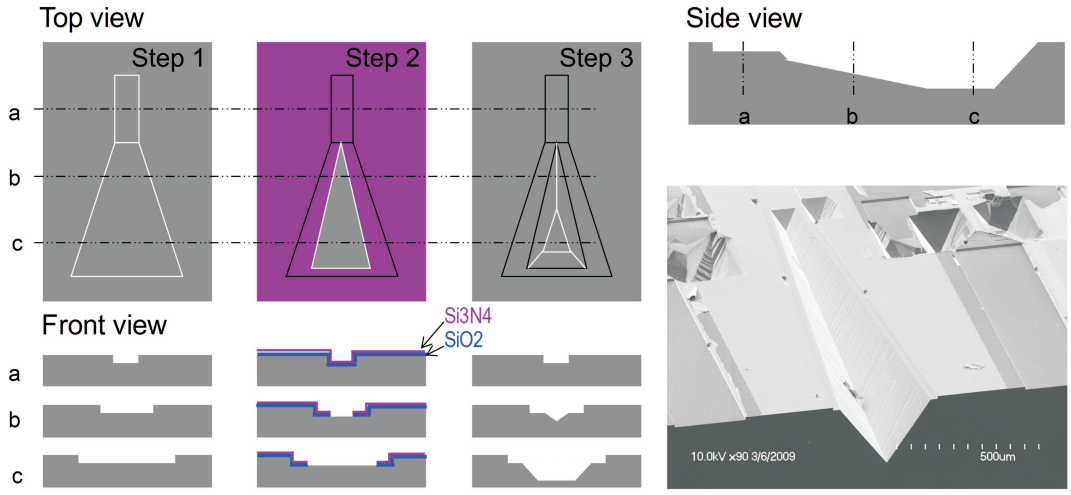

Figure 2.12: Microfabrication of the horn antenna in silicon. An SEM image of a fabricated half-block horn is shown in the lower right.

thick resist (SU-8) lithography which simplified the waveguide-to-antenna transition [110]. Biber *et. al.* [111], demonstrated a monolithic approach to the design of a 600 GHz octagonal horn antenna in silicon using dry and wet etching techniques. Here, we resort to a similar fabrication technology to realize a THz pyramidal horn in silicon.

Figure. 2.12 schematically shows the fabrication process for the pyramidal horn antenna. Boron-doped p-type <100> silicon wafers were used for this purpose. The first step involved a deep (~ 9 μm) dry-etch of longitudinal trenches that would eventually serve as hollow rectangular waveguides encompassing the Fabry-Pérot MM waveguide on the sides. The depth of this etch has to be slightly smaller than the thickness of the active material in the MM waveguide (typically ~ 10 μm) to ensure good electrical contact of the horn to the top metal of the QC-laser. Consequently the current waves propagating on the top conductor would not experience a discontinuity at the QCL-horn transition. Horizontal flare of the horn (along y-direction) was also introduced during this step. For the vertical flare

to be introduced in the z-direction, wet anisotropic etching of silicon in hot Potassium Hydroxide (KOH) solution was chosen. A mask material of high-resistivity to prolonged KOH etching is required to etch very deep ($\sim 200-300\ \mu$m) grooves in silicon. For that purpose, a bi-layer hard mask of silicon dioxide (1000 Å) and silicon nitride (1500 Å) was deposited using low pressure chemical vapor deposition (LPCVD) furnaces. The mask material was patterned in an STS advanced oxide etcher (AOE) machine using CF_4 and O_2 gaseous plasma. Etch rates of Si in KOH along different crystal orientations vary with solution temperature and concentration (in general $r_{<110>} > r_{<100>} \gg r_{<111>}$). A 30% KOH solution at 80°C was used, which has an etch rate of $\sim 1.3\ \mu$m/min along <100> direction and practically stops at <111> planes. As a result, anisotropic V-shaped profiles were obtained with the depth of groove determined by the opening width in the mask and where <111> etch-stop planes met. Indeed a flare in the mask opening provides the required vertical flare in etched silicon. Mask materials were eventually removed in hot Phosphoric acid and Hydrofluoric (HF) acid and the silicon wafers were metal coated in e-beam evaporator (Ti/Au::20/200 nm). An SEM image of one block of the fabricated horn antenna is shown in Fig. 2.12. The structure was cleaved at a short distance from the waveguide-to-horn transition resulting in a diamond-shaped aperture for the horn. Figure 2.13 shows a few more SEMs, with close ups of the the waveguide, and antenna, and roughness inherent in both dry and wet etching of Silicon.

2.4.2 Integration with QC-Laser

Once integrated with a QC-laser, the silicon block and the ground plane of the QC-laser form a hollow waveguide/antenna serving as a mode matching device in front of the QCL facet. Much of the success of this method relies on precise

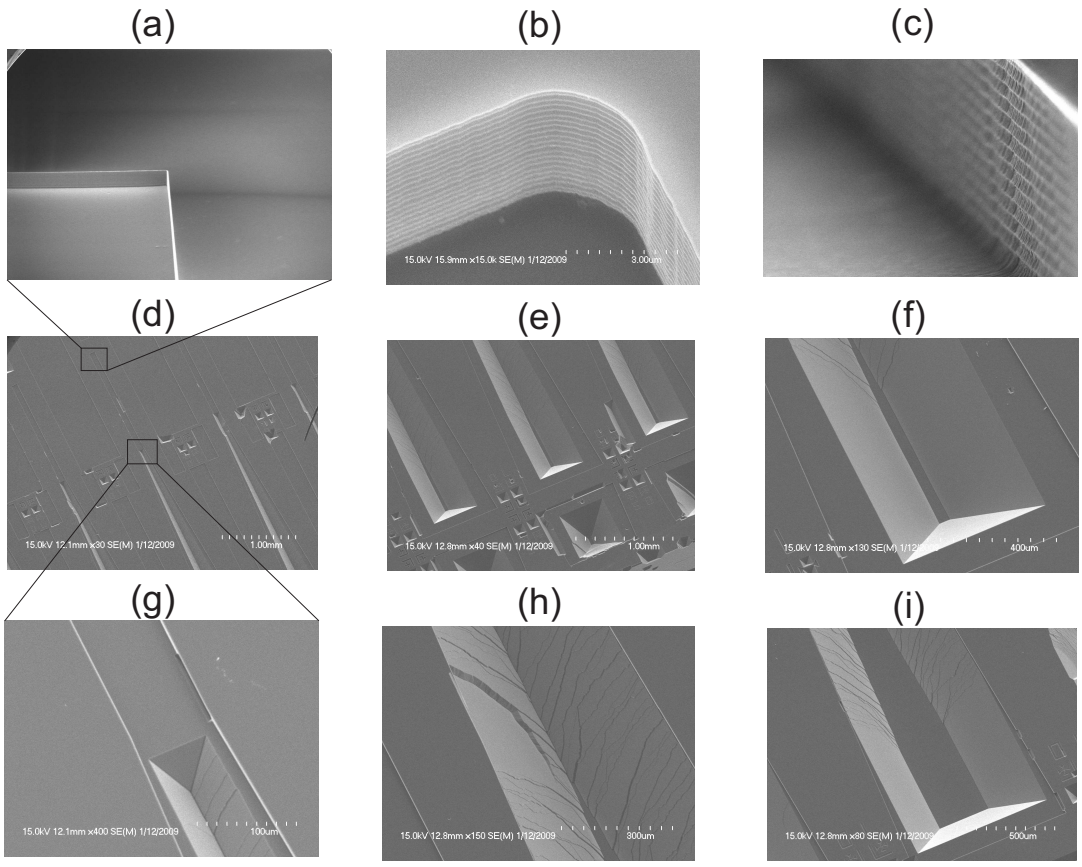

Figure 2.13: Close ups of the waveguide, and antenna, and sidewall roughness due to dry and wet etching. (a)-(c) Shows the undulating profile of the dry-etched waveguide typical of the Bosch process used for reactive ion etching (RIE) of Silicon. (d)-(f) V-groove shape of the horn antenna defined in Silicon using wet anisotropic etching (KOH solution). (g) Close up of the waveguide to horn transition. A trapezoidal step change in height due to undercut during wet etch is obvious. (h), (i) Roughness and horn termination for a representative case with more aggressive horizontal flare in the etch mask.

alignment/mounting of the Si block onto the GaAs die with QC-laser ridges. "Female" alignment marks were monolithically etched in the Si wafer during the dry-etch step so that it can "lock-in" to its correct position on top of the QCL wafer relative to the metal-metal waveguide facet (refer to QCLs fabrication section). Moreover, a smooth transition from the rectangular waveguide to the diamond-shaped horn aperture is required so that the antenna does not introduce additional loss due to reflections.

Another important aspect of this integration is the effect of horn on the laser threshold as governed by Equation. 2.1 ($g_{\mathrm{th}} = \alpha_{\mathrm{tot}}/\Gamma = (\alpha_w + \alpha_m)/\Gamma$) where both waveguide losses (α_w) and mirror losses (α_m) of the QC-laser are modified by the presence of the horn antenna. The "in-waveguide" QCL exhibits higher waveguide losses (to a lesser degree) and reduced facet reflectivities (higher mirror losses) compared to a conventional Fabry-Pérot metal-metal waveguide cavity. Calculated waveguide loss for the fundamental and higher-order lateral modes of a 60 μm-wide metal-metal QCL in waveguides of various heights and widths is presented in Fig. 2.14(a). These results were obtained from 2D finite element simulations and include the contribution of free carrier losses in both metal and active QC gain material. A gap in the vertical direction between the horn block and the MM waveguide ground plane is necessary to avoid DC shorting of the MQW modules. In general, the waveguide losses decrease as the horizontal gap between the QCL and waveguide sidewalls increases. Moreover, smaller vertical gaps are desirable to avoid drastic increase in waveguide losses especially for the fundamental lasing mode.

Figure. 2.14(b) shows calculated mirror losses for the lateral modes of the QCL with a horn antenna abutted at the radiating facet. Facet reflectivities were obtained from 3D finite element simulations for a 60 μm wide QCL and a

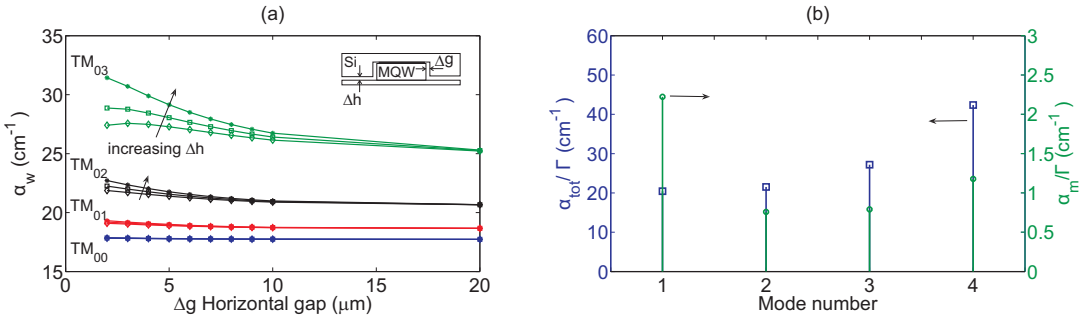

Figure 2.14: Calculated waveguide and mirror losses for lateral modes of an in-waveguide MM QCL. Finite-element simulations were performed at $\omega/2\pi = 3$ THz assuming a fixed 60 μm width and 10 μm height for the metal-metal QCL. A 100 μm width for the rectangular waveguide of the horn and a 2 μm vertical gap between the horn block and the QCL ground plane was assumed in plot (b). Loss calculations are solely due to free-carrier losses as calculated using Drude parameters given in Fig. 2.5 caption for the Au and $n = 5 \times 10^{15}\text{cm}^{-3}$, $\tau = 0.5$ ps, $m^* = 0.067m_0$, $\epsilon_{\text{GaAs}} = 12.9$ for the active gain material.

100 μm waveguide, i.e. a horizontal gap of 20 μm from the sidewalls, assuming 2 μm vertical gap between top block of the horn and the QCL ground plane. Simulations show a factor of three increase in the mirror loss ($R \sim 44\%, \alpha_m/\Gamma \sim 2.25$ cm^{-1}) for the fundamental mode while reflectivities for the higher-order modes remain close to the original value of $R \sim 70-80\%, \alpha_m/\Gamma \sim 0.72$ cm^{-1}. In all mirror loss calculations the metal-metal waveguide Fabry-Pérot ridge cavity was assumed to be 2 mm long. The total loss is also plotted on the same graph and is obviously still dominated by the waveguide losses, that is without waveguide $\alpha_{\text{tot}}/\Gamma \sim 22$ cm^{-1} while total in-waveguide losses are about $\alpha_{\text{tot}}/\Gamma \sim 24$ cm^{-1}. As a result, one might expect a factor of ~ 3 improvement in the slope efficiency ($\frac{dL}{dI} \propto \frac{\alpha_m}{\alpha_w+\alpha_m}$) for the fundamental mode of the QCL.

Experiments

QCL devices of various widths were fabricated in metal-metal technology (Au-Au) from the 10-μm-thick MBE growth NG-E14315 (resonant phonon design

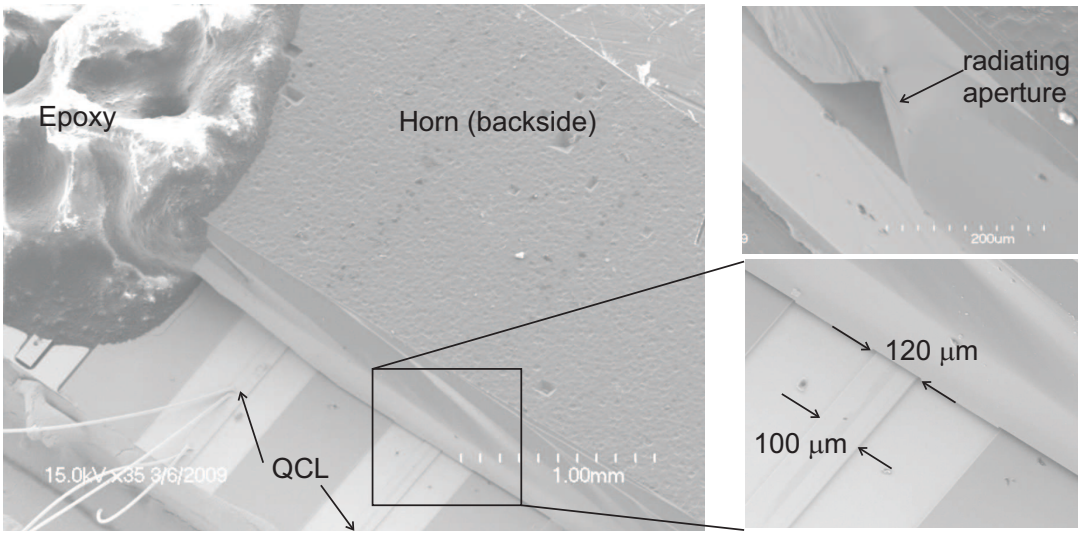

Figure 2.15: SEM images of the metal-metal waveguide ridges with integrated horn antenna. The triangular radiating aperture of the horn is also shown in the upper right.

based on FL178C-M11 aimed at 2.9 THz). Mesas were defined in Chlorine-based gaseous plasma (BCl3:Cl2::60:30 sccm) using PECVD SiO_2 mask (~ 1 μm thick) which left behind dry-etched facets with a long (typically $\sim 2-3$ mm) ground plane in front of the QCL radiating facet. In lieu of our standard Cu-Cu thermocompression waferbonding, Au-Au waferbonding was employed to avoid oxidation of ground plane. "Male" alignment marks (of opposite sense to those of the Si horn block) were defined during the dry-etch step to hold the horns in place. Lastly, an extra metal evaporation/lift-off (Pt:In::500 nm:2 μm) was performed to deposit thick stripes of indium on top of the QCL mesas. Platinum serves as diffusion barrier, to avoid formation of indium-gold alloys. The purpose of In evaporation was to allow soldering of the horn to the laser ridges after alignment was done. Nevertheless, in most cases, the horn was held in place by some additional epoxy stycast. The GaAs wafers were then cleaved in approximately 3 mm-long dies which would yield Fabry-Pérot MM waveguides of ~ 2 mm length with cleaved back facet and dry-etched radiating facet. The horn antenna was

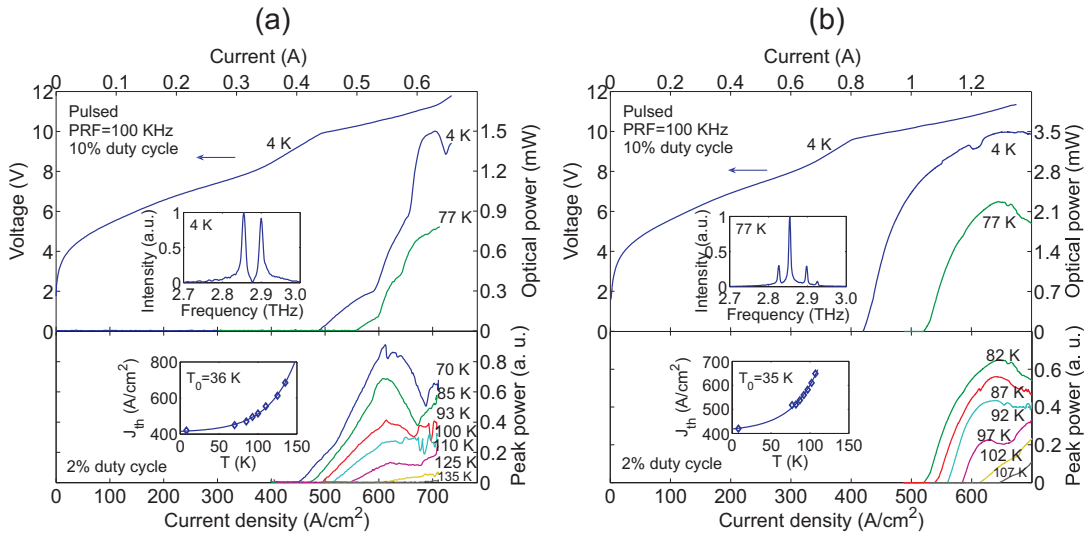

Figure 2.16: Pulsed $I-V$ and $L-I$ characteristics measured from (a) a NG-E14315 MM (Au-Au) Fabry-Pérot laser ridge of dimensions 60 μm×1.5 mm with a 2 mm long ground plane in front of the dry-etched radiating facet, and (b) a NG-E14315 MM (Au-Au) Fabry-Pérot laser ridge of dimensions 100 μm×2 mm with integrated horn antenna. The lower panel temperature-dependent $L-I$s in plot (a) are from a NG-E14315 MM (Au-Au) Fabry-Pérot laser ridge of dimensions 100 μm×2 mm with a 2 mm long ground plane in front of the dry-etched radiating facet. The width of the rectangular waveguide of the horn antenna was 120 μm and the length over which the horn flares to a 300-μm-wide aperture was 1 mm. $L-I$ characteristics were measured using a room-temperature pyroelectric detector, and the peak power was calibrated using a room-temperature thermopile detector. Typical spectra are shown in the insets which are measured with a Nicolet FTIR spectrometer in linear scan mode using a room-temperature deuterated triglycine sulfate (DTGS) pyroelectric detector.

cleaved from Si wafers with a length slightly shorter than the length of the ground plane in front of the QCL. Horns were mounted by mechanically tapping the silicon block on top of the GaAs wafer using the tip of a die bonder. Many attempts were made at early stages of the project which led to severe damages to laser ridges and/or facets. This emphasizes the importance of skilled and steady hands for mounting. Figure 2.15 shows an SEM image of a MM QCL with a horn mounted on top of the ridge at the radiating facet.

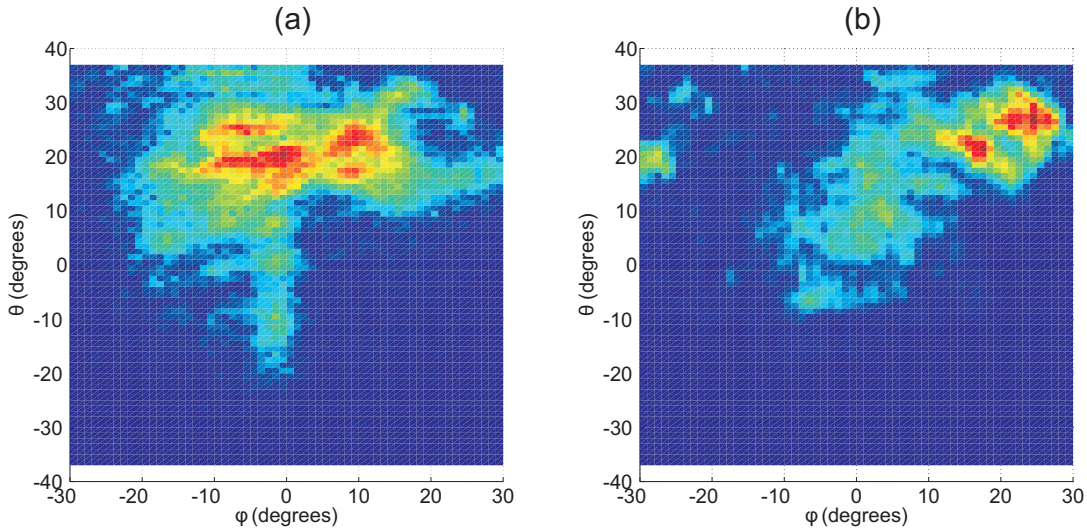

Figure 2.17: Measured far-field beam patterns of two MM terahertz QCLs with integrated horn antenna. Data was collected at 77 K using a room-temperature broadband pyroelectric detector at a distance of 3 in away from the emission dewar. (a) Terahertz QCL was a 100 μm×2 mm MM (Au-Au) Fabry-Pérot ridge laser with a 1 mm long ground plane in front of the radiating facet, biased with 1 μs pulses of 100 KHz PRF (10% duty cycle). (b) Terahertz QCL was a 100 μm×1.4 mm MM (Au-Au) Fabry-Pérot ridge laser with a 2 mm long ground plane in front of the radiating facet, biased with 2 μs pulses of 100 KHz PRF (20% duty cycle). In both cases, the width of the rectangular waveguide of the horn antenna was 120 μm and the length over which the horn flares to a 300-μm-wide aperture was 1 mm.

$L-I-V$ characteristics of the MM devices with and without the horn antenna are presented in Fig. 2.16. MM waveguide Fabry-Pérot cavities of this batch of fabrication lased up to a heatsink temperature of 135 K in pulsed mode (as opposed to $T_{\mathrm{max,pulsed}} = 120$ K for the first generation devices) and exhibited lower threshold currents (J_{th} as low as 420 A/cm^2 was measured from some devices). Addition of the horn antenna resulted in moderate reduction of $T_{\mathrm{max,pulsed}}$ to 107 K without significantly changing the characteristic temperature T_0 (see Fig. 2.16 insets). Threshold current densities were approximately 100 A/cm^2 greater than a standing alone MM waveguide of nearly identical dimensions. Nevertheless, 3.5 mW of power was detectable at 4 K which has so far been the highest peak power measured from a metal-metal waveguide in our lab. Far-field radiation pattern of the device with integrated horn was examined at 77 K. A peak optical power of ~ 2 mW was detectable at 77 K with a thermopile detector placed face to face to the emission dewar. For far-field beam pattern measurements a room-temperature pyroelectric detector was used in a beam-pattern measurement setup put together by the author. The detector was approximately 3 inches away from the device and the surface of a sphere centered at device position in the emission dewar was examined. The device was biased at 630 A/cm^2 —peak power point on the $L-I$ curve— with pulses of 10% duty cycle and 10 KHz repetition rate. While devices exhibited less divergent beam patterns compared to a Fabry-Pérot metal-metal waveguide ridge cavity with cleaved facets (beam divergence $\sim 20^\circ$), a conclusive argument regarding power enhancement and/or beam quality improvement could not be made. This was partly due to multimode lasing of the QCLs which manifested itself in the measured far-field beam patterns of Fig. 2.17. For instance, the device whose 77 K beam pattern is presented in Fig. 2.17(a) exhibited a multimoded behavior (see Fig. 2.16(b) inset) with a center frequency of 2.85 THz and satellites at 2.82, 2.9, and 2.925 THz. The free spectral range

in between these modes is not uniform which suggests that the QCL is lasing in multitude of longitudinal and lateral modes. This is further evidenced by multiple "hot spots" present in the far-field measurements. The maxima at $\phi = 0°$ and $\phi \approx \pm 10°$ suggest that the device is lasing in both fundamental and higher-order lateral modes, simultaneously. This is consistent with our calculations of overall losses for such an in-waveguide MM QCL (see Fig. 2.14) where the higher-order lateral mode exhibits threshold gain values comparable to those of the fundamental mode(s). Although asymmetric with respect to $\phi = 0$ plane, the null at the center of the beam pattern from a different device (shown in Fig. 2.17(b)) is also indicative of device operation in a higher-order lateral mode. This may also explain the lower peak detectable power from this device —only ~ 1 mW at 77 K as apposed to 2.1 mW in Fig. 2.16(b).

Laterally corrugated distributed feedback terahertz QCLs, similar to the ones demonstrated in [112], would be ideal for such an integration so that the waveguide and the horn antenna are only fed with a single THz mode. Alternatively, one can implement a true rectangular waveguide with a gap above the MM waveguide contact by etching rectangular waveguide trenches deeper than the MM QCL active region thickness, or using LIGA techniques [113, 114]. If the output radiation from a THz QCL can be efficiently coupled into a single-mode rectangular waveguide, then the propagation, transmission, and manipulation of the terahertz radiation can entirely be controlled by well-established rectangular waveguide techniques. Much of the success of this scheme, however, relies on efficient coupling of the THz power into the rectangular waveguide which is still suffering from a large impedance mismatch at the QCL-to-waveguide transition, mostly due to the discontinuity seen by the terahertz "current" wave in the QCL top contact. In an effort to address this issue, our group in collaboration with NASA's JPL have attempted integrating a radial probe in the QCL waveguide design for an

efficient transition to a rectangular waveguide TE_{10} mode [18]. Nonetheless, fabrication of such a MM waveguide QCL with integrated waveguide probe rendered extremely challenging. Other mode converters such as adiabatic tapers or grating couplers may also be integrated into the metal-metal QCL waveguide design to further improve the coupling efficiency at the transition point. Quantum-cascade lasers with facet reflectivities as low as $1 - 3\%$ have been demonstrated in the mid-infrared range [115] where focused ion beam (FIB) has been used to mill subwavelength antireflection (AR) gratings on the radiating facet of a mid-IR QCL. This idea can be extended to the terahertz, albeit with a different implementation, where subwavelength grating structures at the facet are incorporated in the metal-metal waveguide fabrication to realize an effective medium that acts as an impedance/index matching transformer. Nonetheless, such a design is vulnerable to excitation of higher-order lateral modes in the QCL metal-metal waveguide that can never couple into the rectangular waveguide as the reflectivity of higher-order modes are not comparably affected by the AR grating.

2.5 Summary

This chapter discussed many different aspects of the design, fabrication, and characterization of terahertz quantum-cascade lasers. Operating principles of the active region designs based on resonant-phonon depopulation in a four-well module were discussed. Designs based on LO phonon depopulation have so far set the record maximum operating temperatures for THz QCLs. While the first terahertz QCL was demonstrated with a single-plasmon waveguide [33], the use of double-plasmon metal-metal waveguides has proved critical in obtaining the existing record temperature performance and operation at longer wavelengths. Design and fabrication of metal-metal waveguides with a robust copper-to-copper

thermocompression bonding technique was presented in section 2.2. THz QC-lasers with resonant-phonon active regions and metal-metal (Cu-Cu) waveguides were demonstrated at $2.4-3.3$ THz by the author which operated up to a heatsink temperature of 136 K. Despite their superior temperature performance, Fabry-Pérot MM waveguide cavities with cleaved facets suffer from inefficient power outcoupling and poor radiation patterns. Development of a micromachined horn antenna for integration with MM waveguide terahertz QCLs was discussed. The antenna acts as a facet-mounted mode-matching device that allows launching near Gaussian beams while the narrow ridge geometry of the Fabry-Pérot MM waveguide is preserved along with its advantages for low power dissipation and high temperature of operation. Nevertheless the fabrication and integration of the horn antenna with QCLs turned out to be extremely challenging. Consequently, a radically different approach based on transmission-line metamaterial concepts — discussed in the subsequent chapters— was pursued by the author and coworkers which is monolithic in fabrication and could potentially have higher impact on the field.

CHAPTER 3

Active Terahertz Transmission-Line Metamaterials

In the past decade there has been a dramatic surge of interest in electromagnetic metamaterials that allow one to engineer material properties not found in nature —such as negative refraction [116], optical magnetism [117], or near-zero permittivity and permeability [118]. This is typically performed by embedding a material with dielectric, plasmonic, or metallic inclusions that are sufficiently small compared to the wavelength of interest so that wave propagation occurs according to refraction through an effective medium, rather than by diffraction as in a photonic crystal. However, many metamaterials are plagued by strong losses associated with the resonant character of these inclusions. For example, material losses limit one's ability to obtain subwavelength resolution with a superlens [119, 120]. It has been proposed that this problem could be alleviated by integrating active material to provide gain via stimulated emission or optical parametric amplification [121–124]. Beyond compensating losses, active metamaterials may enable entirely new classes of devices, such as subwavelength laser resonators, zero-index lasers that resonate with uniform phase (i.e. infinite wavelength), low-divergence leaky-wave laser antennas, emitters with arbitrary wavefront engineering, and novel nonlinear optical devices.

The terahertz frequency range is well suited to the exploration of active meta-

material concepts: metals are good conductors with relatively low losses, structures with subwavelength dimensions can be readily obtained using modern microfabrication techniques, and semiconductor photonic gain is available via THz QC-lasers. To date, most of the metamaterial demonstrations in the THz range have been based upon planar split-ring resonator designs, which have been used for novel demonstrations of terahertz magnetism, tunable resonators, perfect absorbers, and amplitude/phase modulators [91, 125–128]. Composite right/left handed (CRLH) transmission line metamaterials, however, comprise an alternative design approach (first demonstrated in the microwave range [90, 129–131]), where introduction of distributed series capacitance and shunt inductance elements into a conventional transmission line allows left-handed (negative index or "backward wave") propagation. The transmission-line metamaterial concept is scalable from microwave to terahertz frequencies and perhaps even to infrared and visible wavelengths [132]. At mid-infrared frequencies and beyond, however, metals becomes more inductive and the inductance of subwavelength inclusions is dominated by kinetic energy of electrons rather than geometry [133]. This is accompanied by a penalty in loss and extra challenge in realizing deep subwavelength dimensions. Nonetheless, availability of higher photonic gain at mid-infrared wavelengths, at least at present, may prove an advantage over the terahertz QC gain medium.

In this chapter, I propose several novel terahertz CRLH transmission-line metamaterial designs realizable in quantum-cascade structures, and investigate their feasibility for laser resonators and traveling-wave antennas. Full-wave finite element simulations as well as circuit simulations were performed to design and verify the feasibility of a one-dimensional CRLH transmission line in the terahertz range.

3.1 Terahertz CRLH Transmission Lines

The proposed active terahertz CRLH transmission-line metamaterial is shown in Fig. 3.1. The foundation of the structure is a 5 μm-tall narrow-width (~ 10 μm) metal-metal waveguide. These waveguides are ideally suited for this integration scheme as they are, in principle, terahertz microstrip transmission lines with distributed photonic gain within the dielectric. Distributed subwavelength inclusions in a metal-metal QC structure are realized by introducing gaps in the top metal contact layer (equivalently introducing capacitive lumped elements in the series branch of the line's circuit model) and virtual current paths from top contact to the ground (equivalently introducing inductive lumped elements in the shunt branch of the line's circuit model).

Such a structure can be considered as an infinite cascade of CRLH unit cells (with the cell size much smaller than the guided wavelength) whose dispersion characteristics is determined by the interplay of various resonances that occur in the shunt and series branches of the unit cell's LC network (see Fig. 3.1). Of particular importance are the so-called shunt and series resonance frequencies, defined as $\omega_{\rm sh} = (C_R L_L)^{-1/2}$ and $\omega_{\rm se} = (C_L L_R)^{-1/2}$ respectively. Conventional right-handed (RH) propagation along a transmission line is typically described by distributed shunt capacitance C_R and series inductance L_R, while C_L and L_L represent the series capacitive and shunt inductive elements that allow left-handed (LH) wave propagation.

The propagation constant along the line is given by (see [134] for instance)

$$\beta(\omega) = \frac{s(\omega)\omega_L}{a}\sqrt{\left(\frac{\omega}{\omega_R\omega_L}\right)^2 + \frac{1}{\omega^2} - \frac{1}{\omega_{se}^2} - \frac{1}{\omega_{sh}^2}} \tag{3.1}$$

where ω is the radian frequency, $\omega_R = (C_R L_R)^{-1/2}$ and $\omega_L = (C_L L_L)^{-1/2}$ are

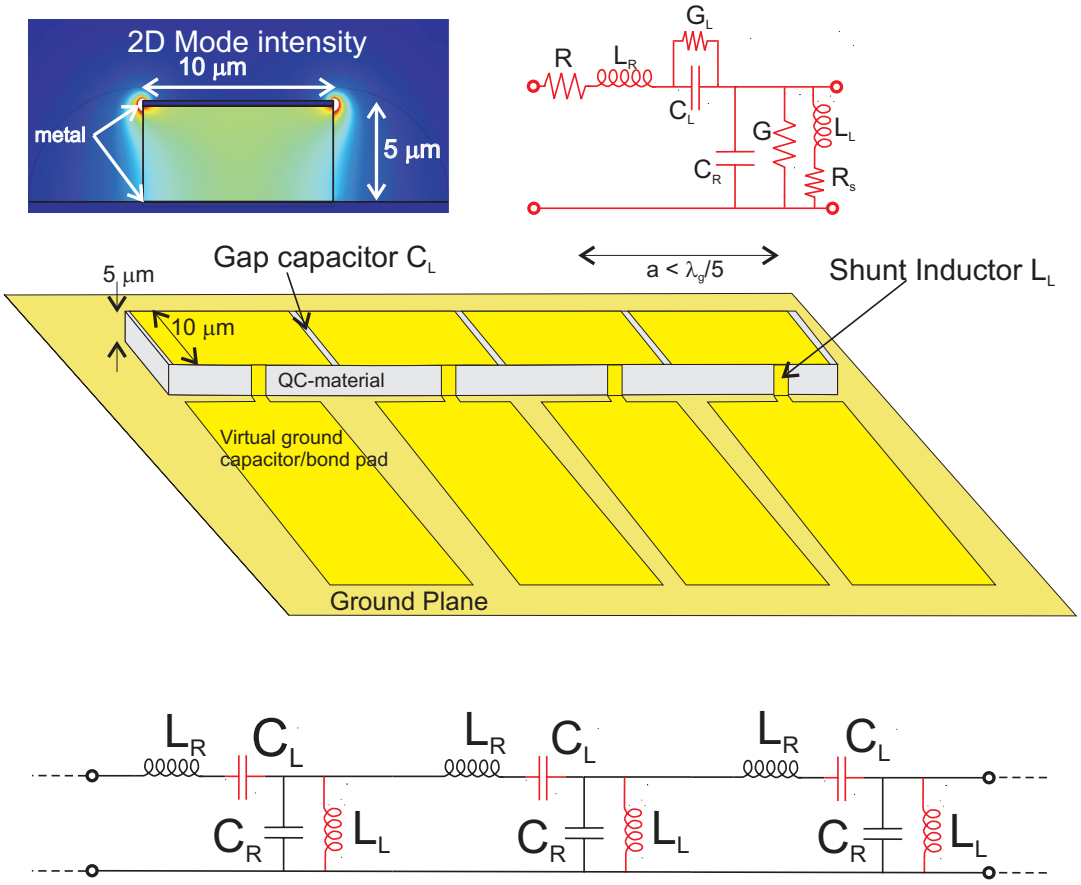

Figure 3.1: Schematic of the proposed QC-CRLH transmission line metamaterial. Distributed subwavelength inclusions in a metal-metal THz QC structure are realized by introducing gaps in the top metal contact layer and virtual current paths from top contact to the ground. Insets: (top right) equivalent transmission line model for one unit cell of the QC-CRLH metamaterial showing series capacitances and shunt inductances in the lines circuit model, respectively. Also included are the shunt and series resistive elements due to radiative and ohmic losses (or gains) in the QC material and conductors. (top left) 2-D mode profile for an unperturbed metal-metal THz QC-laser of the same cross-sectional area at 2 THz.

resonances due to purely right- and left-handed transmission-line elements, respectively, and $s(\omega)$ is a sign function defined as

$$s(\omega) = \begin{cases} -1 & \text{if } \omega < \min(\omega_{se}, \omega_{sh}), \text{ LH range} \\ +1 & \text{if } \omega > \max(\omega_{se}, \omega_{sh}), \text{ RH range.} \end{cases} \tag{3.2}$$

In deriving equation (3.1), I have assumed a lossless line where contribution of resistive elements due to ohmic and radiation losses is neglected. For a weakly lossy CRLH transmission line, the propagation constant and characteristic impedance of the line does not alter drastically. However, as shown in [134], introduction of losses reduces group velocity over a given bandwidth, which increases as the amount of loss increases.

First we note that, $\beta(\omega) = 0$ for $\omega = \omega_{\text{sh}}$ or $\omega = \omega_{\text{se}}$. If $\omega_{se} \neq \omega_{sh}$ (an unbalanced design), there exists a stopband between ω_{se} and ω_{sh} which separates the left-handed range, where the propagation constant $\beta < 0$ and group and phase velocities are anti-parallel, from the right-handed range with $\beta > 0$ and group and phase velocities are in parallel. On the contrary, a balanced CRLH design ($\omega_{sh} = \omega_{se}$) has a seamless transition from the left-handed to right-handed region with the transition frequency occurring at $\omega_0 = \omega_{\text{sh}} = \omega_{\text{se}}$. A balanced CRLH line supports "propagation" with infinite wavelength, corresponding to zero phase shift ($\beta(\omega_0) = 0$) across the unit cell, due to nonzero group velocity at the transition frequency ω_0.

Figure 3.2 shows the dispersion diagram for the proposed QC-CRLH transmission line metamaterial. A commercial finite element electromagnetic solver (Ansoft's HFSS) was used to perform full-wave simulation of the metamaterial. A single CRLH unit cell embedded in a conventional RH line was excited with the THz mode using port boundary conditions, and the s-parameters were ex-

tracted. Per-unit-length values of phase shift for an infinitely long 1D structure were calculated by assuming a Bloch-periodic wavefunction for the traveling wave and applying periodic boundary conditions to the unit cell of the line represented by its s-parameters or equivalently its [ABCD] matrix. Results are plotted in Fig. 3.2(b) where the dispersion diagram of the QC-CRLH structure is also obtained from circuit simulations using the lossless transmission line model given in its inset. Both the circuit model and full-wave simulation shows that below 1.9 THz ($\omega_{\rm sh}/2\pi = 1.9$ THz) the structure supports backward waves (left-handed branch) while above 2.23 THz ($\omega_{\rm se}/2\pi = 2.23$ THz) forward waves are supported (right-handed branch). At each given frequency, the dispersion diagram of Fig. 3.2, defines an effective mode index for the CRLH transmission line according to $\beta(\omega) = n_{\rm eff}\frac{\omega}{c}$. The modes that lie above the light line have absolute effective mode indices smaller than one ($-1 < n_{\rm eff} < 1$) and couple into free-space radiative modes. The dispersion characteristics, and particularly shunt and series resonances at the stopband edges, are well fit using a lossless circuit model using extracted parameters from 3-D finite element simulations. Inclusion of metal losses is perturbative, and does not significantly affect the dispersion relation.

The design strategy proceeded as follows. 2-D finite element simulations were performed initially to estimate equivalent transmission line parameters for purely RH metal-metal waveguides. Per-unit-length values of $C_{R'} = 2.71 \times 10^{-10}$ F/m and $L_{R'} = 3.17 \times 10^{-7}$ H/m were calculated for a 10-μm wide and 5-μm tall waveguide, resulting in line characteristic impedances and effective mode indices $Z_c = \sqrt{L_{R'}/C_{R'}} \approx 34$ ohms and $n_{\rm eff} \approx 2.8$, respectively. Values of the C_L and L_L were then chosen so as to obtain nominally balanced operation. The lumped element parameters extracted from a full 3-D finite element simulation (shown in Fig. 3.2 inset) are slightly different, which demonstrates the need for full-wave simulation for final optimization. A series of full-wave simulations were performed

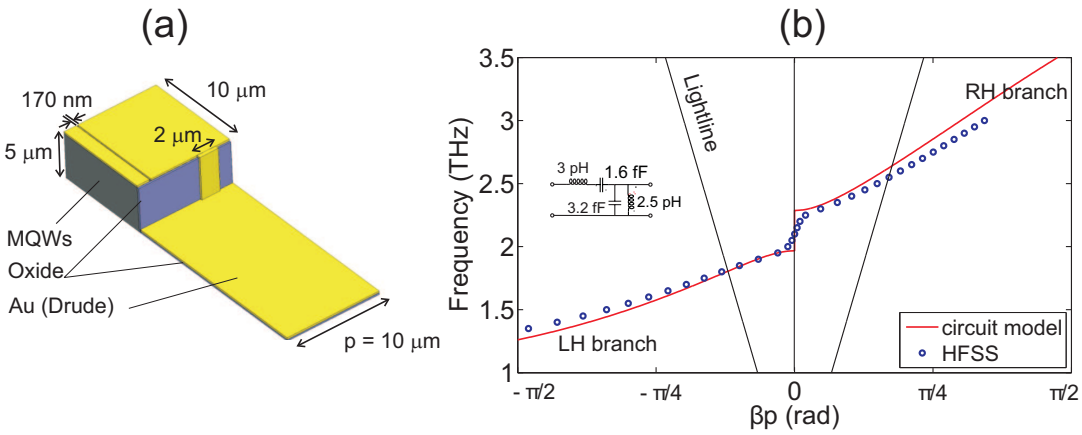

Figure 3.2: Dispersion characteristic of the 1D QC-CRLH transmission line structure obtained by finite element method and circuit theory. Also shown is the simulated unit cell geometry, and extracted values of CRLH parameters used to fit the circuit model to the full-wave simulations.

to tweak the unit cell design until a nearly balanced CRLH transmission line was achieved. The optimized design had a 0.17 μm gap and a 2 μm-wide stub. Such submicron dimensions can be realized in practice using electron beam lithography or focused ion beam etching.

3.2 Zero-Index Terahertz Quantum-Cascade Laser

Let us consider the feasibility of laser resonators formed by a section of zero-index metamaterial line with open terminations. Because the condition for resonance is a round trip accumulated phase of $2\pi \times$ integer, in addition to the usual standing wave Fabry-Pérot resonances, zeroth-order resonances will appear. Having a balanced CRLH line is not necessary for this purpose, as the unbalanced line will resonate at either of the band-edge frequencies $\omega_{\rm sh}$ and $\omega_{\rm se}$ depending upon the termination. A zeroth-order resonator (ZOR) shorted at both ends has a strong electric field component along the longitudinal direction and oscillation occurs in its series resonance $\omega_{\rm se}$ (equivalent to a series $L_R R C_L$ circuit). An

open-ended ZOR, on the other hand, has a strong electric field component in the transverse direction associated with the shunt capacitance and oscillates in its shunt resonance ω_{sh} (equivalent to a shunt $L_L G C_R$ circuit) [134]. The latter mode is most appropriate for implementation of a zero-index QC-laser, since the intersubband transitions only exhibit nonzero dipole matrix elements along the epitaxial growth direction. Hence, the vertically polarized E-field associated with the shunt resonance will couple strongly to the QC intersubband gain, whereas the series resonance will couple poorly, as most of the E-field is localized in the series gaps with the incorrect polarization.

A zero-index laser is interesting partly because of its potential to suppress the phenomenon of spatial hole burning —a cause of multi-mode lasing, dynamic instabilities, and gain nonlinearities in semiconductor lasers that has been theoretically and experimentally documented in mid-infrared and terahertz quantum cascade lasers [135, 136]. When a laser is pumped to reach threshold, the modal gain coefficient is clamped at its threshold value g_{th}, which is nearly equal to the total modal loss coefficient. The physical reason for this is the onset of stimulated emission which reduces the population inversion, a process known as gain saturation. Owing to the formation of standing waves in Fabry-Pérot cavities and distributed feedback cavities, interaction of the gain medium with electric field is non-uniform and is effectively zero at the nulls of the sinusoidal standing wave. Additional current injection will continue to increase gain at these nulls, often causing other modes with different spatial profiles to oscillate, resulting in mode hopping or multi-mode lasing. This problem is particularly acute for long-wavelength terahertz QC-lasers since the length scale of the mode variation is large ($\beta^{-1} \sim 5 - 10$ μm), and the non-radiative intersubband lifetimes are short ($\tau \sim 1$ ps), which results in a relatively short diffusion length for population inversion (i.e. gain) within a quantum-cascade module ($\sqrt{D\tau} \sim 100 - 400$ nm).

Thus carrier diffusion is not able to smooth gain variations in THz or mid-IR QC-lasers. In principle, a ZOR metamaterial laser can be made to have a uniform field, an attractive prospect to alleviate the problem of longitudinal spatial hole burning.

An additional advantage of a ZOR laser is improved conversion efficiency of electrical pump power to THz photons and reduced gain compression due to the improved mode uniformity, as there is no wasted electrical power used to pump parts of the active region that do not interact with the desired mode. This enhancement can be expressed in terms of the so-called modal-uniformity η_u as given by the expression:

$$\eta_u = \frac{\left[\int_{\text{act}} |E_x|^2 dv\right]^2}{\text{V}_{\text{act}} \int_{\text{act}} |E_x|^4 dv} \tag{3.3}$$

which is defined for the electric field component E_x that interacts with active material. As described in [137], the effect of this parameter is seen in the output power, as the laser slope efficiency is proportional to η_u. For example, one would expect a factor of $\frac{3}{2}$ improvement in the slope efficiency in a single mode laser with a uniform mode compared to a single mode Fabry-Pérot standing wave laser. Of course, this is only advantageous if the metamaterial does not introduce excessive loss. Moreover, this argument only holds up if there is no lateral field variation for the metamaterial mode. For instance, if the metamaterial mode undergoes a half sinusoid variation in the transverse direction, e.g. when width of the inductive stubs on the sidewall becomes equal or comparable to the unit cell size p, it can only function as well as a fundamental Fabry-Pérot standing wave laser mode.

In this section, I investigate the feasibility of a zero-index terahertz quantum-cascade laser based upon CRLH zeroth-order resonators by calculating the bulk intersubband gain coefficient g_{mat} required to balance all losses and reach lasing threshold for various modes. This approach naturally includes all ohmic and ra-

diative losses, and does not require explicit calculation of any modal confinement factors, i.e. $g_{\mathrm{mat}} = \alpha_{\mathrm{mod}}/\Gamma = (\alpha_{\mathrm{ohm}} + \alpha_{\mathrm{rad}})/\Gamma$. This form is chosen as it is readily understood by the quantum-cascade community, and can be compared to calculated and measured gain coefficient values for various lasers in the literature. We consider a terahertz QC resonator consisting of five unit cells of the proposed CRLH transmission line (see Fig. 3.3(a) inset). This size is chosen as a compromise between computation time and accuracy. 3-D finite element simulations were performed to identify the resonant modes of the cavity and to estimate their required lasing threshold intersubband gain. To that goal, the five-cell CRLH resonator was placed in a two-port device and transmission through the cavity was probed by examining s-parameters of the device. Weak coupling was ensured by employing large gaps in between the resonator and ports. Photonic gain was incorporated in the QC material using a general purpose anisotropic dielectric loss tangent

$$\tan\delta_{xx} = \frac{\epsilon^{''} - (n_{\mathrm{bulk}} g_{\mathrm{mat}} c/\omega)_{xx}}{\epsilon^{'}} \tag{3.4}$$

where c is the speed of light in free-space, and $\epsilon^{'}$ and $\epsilon^{''}$ are the real and imaginary parts of the relative permittivity of the dielectric medium ($\epsilon_r = \epsilon^{'} - \imath\epsilon^{''}$). This form is not intended to accurately represent the dispersive lineshape for intersubband gain, but is rather intended solely to evaluate the necessary material gain value to reach lasing threshold for a particular mode.

Figure 3.3(a) shows the simulated transmission through the "cold" and "active" Fabry-Pérot cavity based on zero-index CRLH resonator. Cold cavity simulations indicate enhanced transmission at resonant frequencies of the resonator. Resonances occur at $\omega_{\mathrm{m}=0} \approx \omega_{sh}$ ($\beta = 0$), $\omega_{\mathrm{m}=\pm1}$ ($\beta = \pm\frac{\pi}{\ell}$), and $\omega_{\mathrm{m}=\pm2}$ ($\beta = \pm\frac{2\pi}{\ell}$) with ω_{+2} falling out of the considered frequency range here. Although first-order and higher-order resonances are still determined by the cavity length, zeroth-

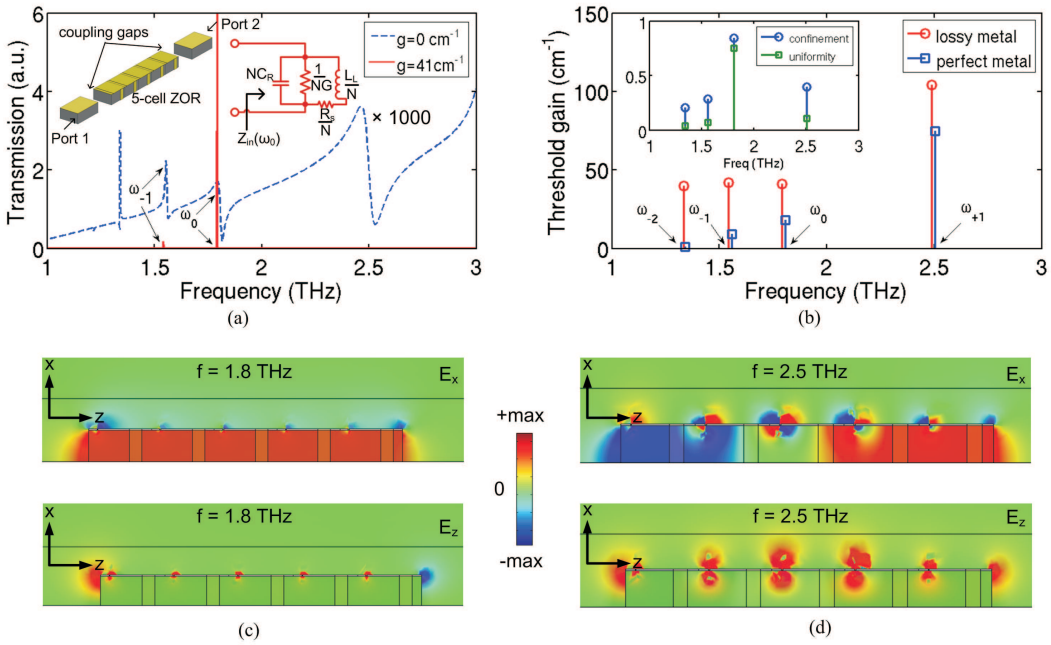

Figure 3.3: A terahertz quantum cascade laser consisting of five unit cells of the proposed CRLH transmission line. (a) Simulated transmission through the "cold" (blue curve) and "active" (red curve) cavity –that is given sufficient bulk gain beyond QC-material transparency (41 cm^{-1}) to bring the zeroth order mode close to oscillation. Insets: (top left) Simulation setup showing a two-port device weakly coupled to the resonator. (top right) Equivalent circuit for the open-ended zero-index CRLH resonator ($m = 0$ mode only) which assumes $N = 5$ unit cells. (b) Threshold gain values for each resonant mode of the QC-CRLH resonator. Inset: 3D confinement factor (blue circles) and modal uniformity (green squares) calculated for all resonant modes of the cavity. (c) and (d) E-field plots for $m = 0$ and $m = +1$ resonances. Note that the $m = 0$ mode has a uniform electric field across the entire CRLH resonator at $\omega_0 = 1.808$ THz with only a very small longitudinal component across the gap capacitors.

order resonance occurs at the band-edge frequency ω_{sh} independent of the cavity length which is unique to zero-index CRLH resonators. The slight deviation from ω_{sh} is due to loading effects of radiation from facets. Lasing threshold of each mode is obtained by sweeping the gain values; as the gain coefficient approaches its threshold value g_{th} for a given mode, the transmission amplitude approaches infinity and the linewidth collapses to zero. In a physical device, saturation of the gain medium would limit the ultimate field intensity and linewidth.

Three primary sources of loss in the active metamaterial are expected: radiation losses, ohmic losses in the metallic lines, and quasi-free-carrier losses due to n-type doping of GaAs/AlGaAs heterostructures in the active region. Ohmic losses in the metal were implemented using an ac Drude model for the complex relative permittivity ϵ_r. In these simulations I used a value of $\tau_{\text{gold}} = 60$ fs. This value of τ corresponds to operation at 77 K — this reflects the fact that at present THz QC-lasers are limited to cryogenic operation. QC active material was modeled as bulk GaAs with an average doping level of 5×10^{15} cm^{-3} and a 0.5 ps Drude relaxation time (at 77 K) as is common for terahertz quantum cascade lasers with resonant-phonon active region designs. This doping level is sufficiently low that our frequencies of interest are well above the semiconductor plasma frequency of 680 GHz; hence the primary effect of the doping is a perturbative loss. While I have included this last contribution for the sake of completeness, I must emphasize that the Drude approximation for loss within the active region is only approximately accurate, as these losses result from cross-absorption of THz radiation by carriers that reside in the quantum-cascade injector reservoir. Furthermore, this component of the loss depends upon the details of the particular QC design, doping level, and temperature, and therefore can likely be reduced by engineering either the active region or the geometry/structure of the series gap capacitor.

A threshold gain value of 74 cm^{-1} is calculated for the zeroth-order resonance. These simulations were repeated with conductor and semiconductor free-carrier losses "switched off" so that power loss due to radiation could be distinguished from ohmic losses in metal and QC-material. Simulation results indicate radiative losses of 18 cm^{-1}, ohmic losses of 23 cm^{-1} in metal, and free-carrier absorption of ~ 33 cm^{-1} in the QC material for the zeroth-order resonant mode. One beneficial effect of the free-carrier loss in the doped semiconductor is that it may provide a selection mechanism for the zeroth-order mode among all resonant modes of the CRLH resonator (see Fig. 3.3(b)). This is partly due to the enhanced longitudinal field strength within the QC-material across the series gap capacitors for non-zero-order resonances. This is a parasitic effect, represented by the conductance G_L in the unit cell circuit diagram in Fig. 3.1. Moreover, the free-carrier absorption increases with wavelength ($\alpha_{fc} \propto \lambda^2$) which further increases the losses at lower frequencies.

Plotted in the inset of Fig. 3.3(b) are 3D confinement factors Γ for each resonant mode of the CRLH cavity, defined as:

$$\Gamma = \frac{\int_{\text{act}} |E_x|^2 dv}{\int_{-\infty}^{+\infty} |\vec{E}|^2 dv} \tag{3.5}$$

where E_x is the x-component of the total electric field $\vec{E}$. Γ is a measure of the terahertz mode overlap with the QC gain medium that contribute to the stimulated emission via intersubband radiative transition. As expected, of all resonant modes of the CRLH resonator, the zero-index resonance has the largest overlap ($\Gamma = 0.85$) with the quantum-cascade gain medium. This fact is corroborated by the E-field plots depicted in Figs. 3.3(c) and (d) for the CRLH resonator at $m = 0$ and $m = +1$ resonances. Vector field plots indicate uniform electric field across the entire structure corresponding to zero phase shift (infinite lambda)

resonance at $\omega_0 = 1.808$ THz. At $m = 0$ resonance, E-field has a strong transverse component (uniform along the cavity length) with very small longitudinal component across the gap capacitors as opposed to $m = +1$ resonance which has a half-wavelength variation along the resonator length and is associated with much stronger E_z component across gap capacitors. Also plotted in the inset of Fig. 3.3(b) are 3D modal uniformities, η_u, for each mode of the CRLH cavity at resonance. Among all resonant modes, the zero-index mode has the most uniform profile throughout the cavity ($\eta_u = 0.75$).

To put these gain and loss values into context, I compare these thresholds to those from a conventional Fabry-Pérot resonator of nearly identical dimensions. A standard MM waveguide QC-laser of similar cross-sectional area (5 μm $\times$ 10 μm) and comparable length (65 μm) was considered which supports non-zero positive resonances, one of which coincides with the CRLH resonator zeroth-order resonance at 1.804 THz. Such a resonator exhibits ~ 7 cm^{-1} radiative losses, ~ 11 cm^{-1} conductor losses, and ~ 32 cm^{-1} free-carrier loss in semiconductor, yielding threshold gain values ~ 50 cm^{-1}. Compared to a 65 μm-long RH Fabry-Pérot cavity, a CRLH-based QC resonator shows a factor of $1.5 - 2$ increase in its threshold gain value. This results from both an increase in absorption associated with conduction currents through the stub inductors, and an increase in the radiative coupling of the zeroth-order mode. Nonetheless the threshold gain should be achievable for high quality QC-laser material, which can achieve material gain values of $g_{\mathrm{mat}} \sim 50 - 100$ cm^{-1} [138, 139]. While the dimensions of this design are smaller than typical, they are not unprecedented; lasers as narrow as 13 μm and as thin as $3 - 5$ μm have been demonstrated in metal-metal waveguides [61, 62].

Lastly, the effect of resonator length on the zeroth-order resonance was stud-

Table 3.1: Threshold gain values for the zeroth-order resonant mode for different ZOR lengths

ZOR length (μm)	30	50	70	100
Lossless g_{th} (cm^{-1})	14	18	20	22
Lossy metal g_{th} (cm^{-1})	38	41	43	44
Lossy metal/GaAs g_{th} (cm^{-1})	71	74	76	77
Lossless ω_0 (THz)	1.818	1.808	1.802	1.798
Lossy ω_0 (THz)	1.802	1.792	1.785	1.784

ied. The longest structure simulated was 100 μm (10 unit cells), limited by our computational capacity. The results are tabulated in Table 3.1. As expected, the resonant ZOR frequency (ω_0) is largely independent of the resonator length, although there is a slight shift in frequency ($\sim$ tens of GHz) due to the varying loading effect of radiation from facets. While ohmic and free-carrier losses are insensitive to the ZOR length ($\sim$ 23 and 33 cm^{-1} respectively), the radiative losses go up as the length increases. This reflects the increased radiation efficiency of the ZOR as its length begins to approach that of the free space wavelength ($\lambda_0 \sim 166$ μm).

3.3 Active Leaky-Wave Metamaterial Antenna

Another potential application is the use of a zero-index metamaterial as a resonant or leaky travelling-wave antenna that radiates in the surface (broadside) direction. Travelling-wave modes with effective indices less than unity allow leaky-wave radiation, and the uniform phase and magnitude of the zero-index laser mode will result in a directive beam pattern with a large effective aperture compared with a typical antenna resonating in its first mode [134]. The coupling efficiency of such structures will depend sensitively upon the strength of

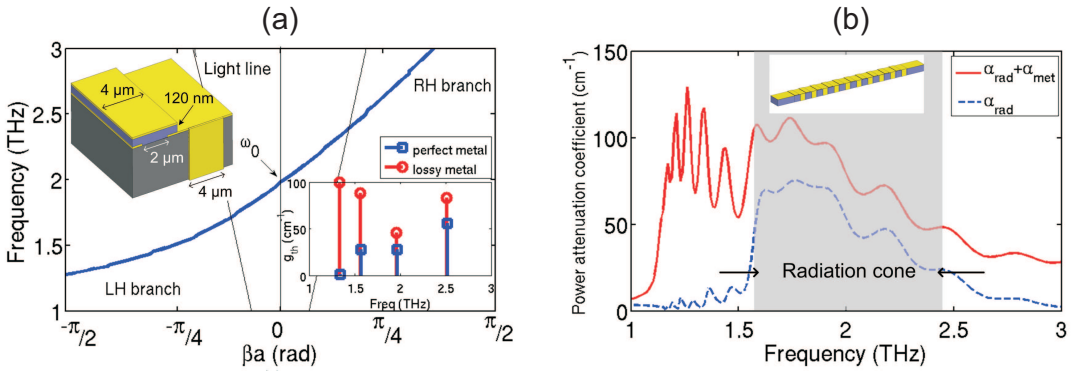

Figure 3.4: (a) Dispersion characteristic of the 1D balanced QC-CRLH structure obtained by finite element method. Insets: (Top left) the simulated geometry; (bottom right) calculated threshold gain values for a five-cell ZOR based on the balanced CRLH design. (b) Attenuation per unit length of a 10 unit cell long, QC-CRLH transmission line. Shaded region corresponds to frequency range where the dispersion curve lies within the fast wave region. Inset shows the simulated geometry. At the transition frequency of 1.95 THz, a zero phase shift and constant amplitude across each unit cell is observed.

the radiative coupling relative to other losses.

While a balanced CRLH design is not required to demonstrate a ZOR laser, balanced operation is preferred for traveling wave applications, such as leaky wave antennas, power-dividers, and zero-index lenses. Employing the proposed unit cell of Fig. 3.2 as starting point, I present an alternate design for a THz QC-CRLH transmission line that exhibits balanced operation. This design was originally introduced in [140] and has no features smaller than ~ 2 μm so that it can be more readily fabricated using optical contact lithography (See Fig. 3.4(a) inset). Instead of a ~ 200 nm gap capacitor, a capacitive patch (overlay) design for the series capacitance is considered. While the gap size was increased to 2 μm, a metal plate insulated by a 120 nm thick layer of silicon dioxide was introduced on top of the gap capacitor to produce a larger series capacitance. The width of the shunt inductance was increased to 4 μm which pushes the shunt resonant frequency ω_{sh} upwards.

The dispersion characteristic of the 1D balanced QC-CRLH design is plotted in Fig. 3.4(a). The dispersion curve was obtained in a similar fashion explained in section 3.2, except that instead of one, 10 CRLH unit cells were embedded in a conventional RH line to model the inter-element coupling more accurately. This reveals that the stopband has been closed, and there is a seamless transition between the backward and forward wave regions with propagation (non-zero group velocity) supported at the transition frequency of $\omega_0 = 1.95$ THz, i.e. zero phase index (infinite wavelength).

In particular, we wish to quantify the radiative losses as a function of frequency —a relevant quantity for leaky-wave antennas. An analysis of a 10 unit cell (100 μm long) segment was carried out to estimate per-unit-length values of these losses in an infinite periodic structure, while lending itself to a reasonably sized simulation space. Although a 10 unit cell segment clearly falls short of the infinite transmission-line case, it nonetheless proved instructive to approximately quantify the radiative power loss for propagation within the light cone. Figure 3.4(b) shows the power loss coefficient for such a CRLH transmission line. It should be pointed out that the oscillating component of the power attenuation coefficient is not intrinsic to the metamaterial. Rather it originates from resonances associated with the finite length of the simulated structure, and imperfect impedance matching between the CRLH line and the ports. Nonetheless, this simulation identifies the major trends and provides approximate values for the traveling wave loss coefficients.

The balanced QC-CRLH transmission line structure exhibits a noticeable increase in radiative loss between 1.65 THz and 2.45 THz. This is to be expected, as the modes that lie above the light lines ($-1 < n_{\text{eff}} < 1$) will couple into free-space radiating modes. Non-zero radiation loss appears to persist for modes below the

light line due to the finite length of our simulated structure —for an infinite line this mode will be guided and should not suffer from radiative losses at all. With the conductive losses "switched on", there is a greater loss over all frequencies, particularly in the LH region where the group velocity is low. In such a traveling wave structure, the availability of the QC gain is critical to compensate for the losses, which would otherwise limit useful lengths of the line to $\alpha^{-1} \sim 100 - 200$ μm. This is particularly important for a leaky-wave antenna, where the directivity of the radiation is dictated by either the physical length of the structure, or the attenuation of the mode (whichever is shorter).

Let us consider the utility of this transmission line for use as a leaky-wave antenna. If such a balanced CRLH transmission line is excited with a frequency within its leaky-wave bandwidth, the antenna is capable of launching directive beams due to the small phase variation between radiating elements. Furthermore, the main beam angle of radiation along the propagating (longitudinal) direction is determined by the dispersion characteristics according to:

$$\theta = \sin^{-1}(\beta(\omega)/k_0) \tag{3.6}$$

where θ is the angle measured from broadside, k_0 is the free-space wave vector, and $\beta(\omega)$ is the propagation constant. Such an antenna is capable of achieving beam scanning from backward ($\theta = -90^\circ$) to broadside to forward endfire ($\theta = +90^\circ$) as the excitation frequency is changed. Alternatively to scanning the frequency, if the lumped elements of the CRLH line are made tunable, the entire dispersion curve can be shifted, and beam steering can be obtained at fixed frequency.

Figure 3.5(a) shows 1-D cuts of the far-field beam pattern at three discrete frequencies within the leaky-wave bandwidth. The far-field beam patterns were extracted from HFSS simulations.Due to computational limitations, only a 20

unit cell (200 μm) long structure was simulated. Because this length (20 unit cell 200 μm) is comparable to the free-space wavelength ($\sim 1.3\lambda_0$ at 2.0 THz), the radiated beam exhibited a large beamwidth in the longitudinal direction (full width at half maximum (FWHM) $\sim 40°$). Nonetheless, backward to forward scanning is still observed. The short length of the simulated line also limits the achievable beam steering. For instance, even though the frequencies 1.75 THz and 2.2 THz are close to the light line, they do not exhibit as large a scan angle away from broadside as one might expect given the dispersion relation. Use of a longer line (many wavelengths) will result in much narrower far-field beam and large range of scan angles. The radiation pattern in the lateral direction is expected to be broad, since the lateral dimension of the waveguide is 10 μm, much smaller than the free space wavelength ($\lambda_0 \sim 150$ μm at 2 THz). Close examination of the calculated beam patterns reveals that the far-field polarization changes as a function of the frequency and scan angle. Figure 3.6 illustrates the far-field radiating components $|E_\theta|$ and $|E_\phi|$ along the longitudinal cut of the structure. At 1.85 THz, the polarization is primarily along the longitudinal direction (E_θ), with the cross polarization component suppressed by 9 dB. Near the zero-index point at 1.95 THz the polarization shifts, with the lateral component (E_ϕ) comparable to the longitudinal component. At 2.15 THz, the dominant component is once again along the longitudinal direction, but still with a significant cross polarization. Looking at the ratio of the major and minor axes of the polarization ellipse (axial ratio), it is noted that the polarization is elliptical at these frequencies, with axial ratio ~ 10 dB at 1.85 THz (essentially linear). However, at 1.95 THz and 2.15 THz, the axial ratio changes to 1.2 and 2.5 dB, respectively, corresponding to an elliptically polarized wave with a left handed sense of rotation. The change in polarization with frequency results from the varying contributions of various radiating elements. For example, resonance in the shunt branch is asso-

ciated with displacement currents within the shunt capacitor C_R and conduction currents in the shunt inductor L_L. In this geometry, this current loop radiates as a magnetic dipole oriented along the waveguide, resulting in radiation with an E-field polarized in the lateral direction (ϕ). Resonance in the series branch is associated with longitudinal currents in the inductor L_R and across the series capacitor C_L, which radiate as laterally oriented magnetic dipoles to produce a far-field polarized longitudinally. Thus, the overall polarization results from the relative contributions of each of these branches, which depends both on the dispersion characteristic, and the fundamental radiative strength of the various elements.

Lastly, we consider the use of the active CRLH transmission line as a power amplifier. For the sake of these simulations the far-field intensity of the antenna radiation was examined for several bulk intersubband gain values incorporated in the QC material. In practice this corresponds to different injection current densities above threshold. The QC gain material was modeled similar to section 3.2 with an anisotropic dielectric loss tangent (Equation 3.4). Figure 3.5(b) shows the far-field beam of the antenna at 2.05 THz which grows in intensity as the g_{mat} on the antenna is increased. This is to be expected as the addition of gain in the antenna section would amplify the field intensity inside the leaky-wave antenna which determines the far-field amplitude directly.

3.4 Summary and Conclusion

In this chapter, I have presented the design and analysis of a new active CRLH transmission-line metamaterial based upon terahertz QC structures in subwavelength metal waveguides. While the dimensions required to achieve backward-wave operation in the $1-2$ THz range are aggressive, they are achievable with

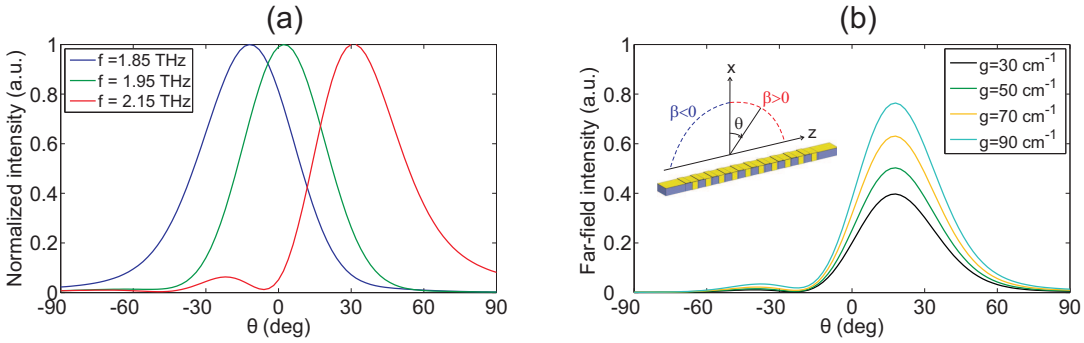

Figure 3.5: (a) Simulated far-field beam patterns of the leaky-wave metamaterial antenna at three discrete frequencies within its leaky-wave bandwidth showing the scanning of the main beam angle with frequency, and (b) amplification of the far-field intensity at 2.05 THz due to the addition of gain (active biasing) in the antenna.

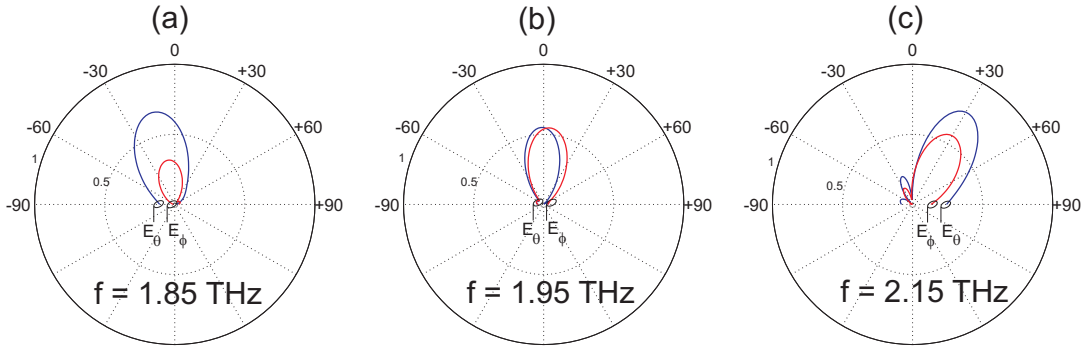

Figure 3.6: Polar representation of the simulated far-field beam patterns of the leaky-wave metamaterial antenna at three discrete frequencies (a) 1.85 THz, (b) 1.95 THz, and (c) 2.15 THz. Components of the electric field along the longitudinal ($|E_\theta|$) and transverse ($|E_\phi|$) directions are shown for each frequency.

modern microfabrication techniques. Full-wave electromagnetic simulations demonstrate the feasibility of a new type of laser based upon a 1-D metamaterial cavity: a zero-index quantum cascade laser. The highly uniform field profile throughout the cavity should provide immunity to spatial hole burning, a phenomenon which can limit the power and stability of single-mode lasers. The zero-index devices described can be used to implement surface-emitting resonant and traveling-wave laser antennas, as well as subwavelength "circuit" laser resonators. The implementation of a zero-index laser is accompanied by a penalty in loss, both due to more efficient radiative coupling, and increased metal and semiconductor free-carrier losses. Compared to a conventional metal-metal waveguide QC-laser, the loss increases by a factor of $1.5 - 2$ for comparable dimensions, although it is likely that these losses can be improved with optimized designs. The required gain to reach threshold should be readily achievable using high quality THz QC-laser material. Furthermore, this disadvantage may be partially alleviated by an increased slope efficiency, and a large optical coupling efficiency —which can be difficult to achieve for the current generation of THz QC-lasers. One can readily envision extending the THz CRLH concept to two-dimensional planar structures for large aperture emitters. Because of the availability of photonic gain and its unique spectral position between the optical and microwave regime, the terahertz frequency range may prove to be an excellent testbed for exploring active photonic metamaterials.

CHAPTER 4

Survey of Early Designs

This chapter surveys a number of attempted ideas/designs in the initial phase of the development of terahertz metamaterials. Despite the fact that none of these devices lased, a great deal of insight for design, fabrication, and testing operational devices was obtained throughout the course of these experiments. Designs introduced in this chapter are all based on narrow-ridge metamaterial transmission lines operating in their fundamental lateral mode (TM_{00}). These devices were all designed around the original idea proposed in chapter 3 which required photolithography on the mesas' sidewall to realize inductive stubs.

4.1 Generation I: Wet-Etched Mesas

In order to be able to perform lithography on the mesas' sidewall(s), metal-metal waveguide ridges with slanted sidewalls of positive slope are required. A natural way of achieving this is to use the wet etching method discussed in section 2.2.2 for mesa definition. The advantage of this approach is two-fold. First, contribution of sidewall roughness to the overall waveguide losses α_w is nearly minimized due to very little roughness introduced during wet etch. Second, for active metamaterials bonding pads are required to DC bias the devices. To further that goal large wirebond pads are normally introduced which would also serve as coupling capacitors for the inductive stub "vias" to the ground plane. The ground planes

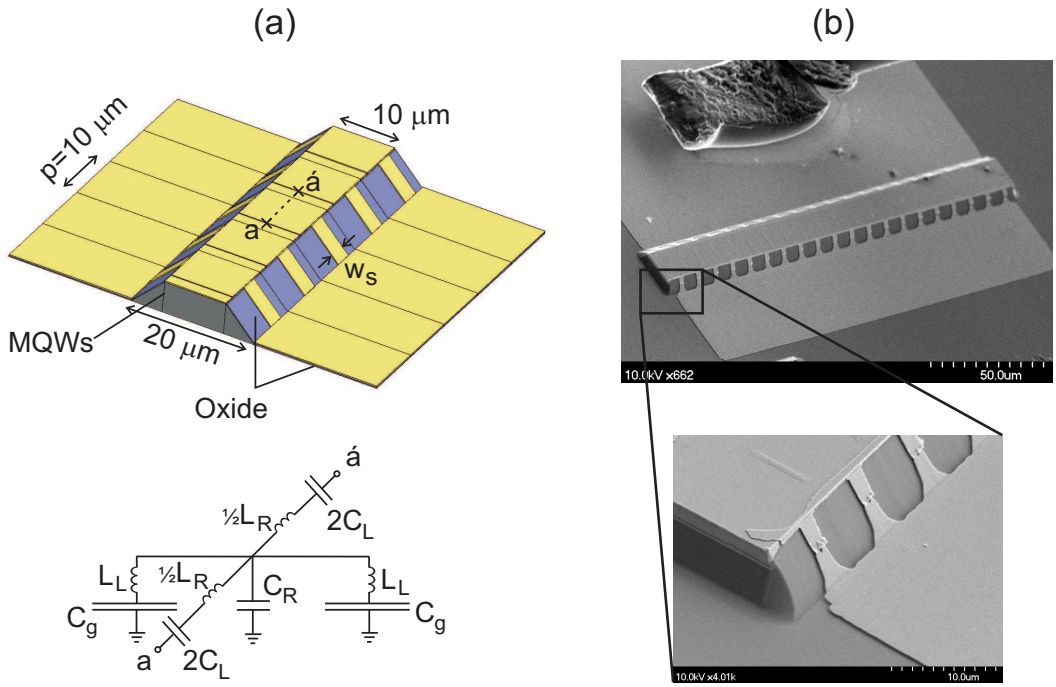

Figure 4.1: (a) Schematic diagram showing a terahertz metamaterial realizable in MM waveguides with inductive stubs on both sides along with its transmission-line model, and (b) SEM image of a fabricated prototype with mesas defined by wet etching H_3PO_4:H_2O_2:H_2O (10:10:250). Active region is 5-μm thick. A 45° slanted sidewall is characteristic of this etch [141] which results in 10 μm variation in ridge width from the top to the bottom.

resulting from wet etching are generally much cleaner and suffer less from "grass-like" imperfections introduced by dry etching. Therefore wet etching was chosen in our first attempt at fabricating terahertz metamaterial devices.

4.1.1 Design and Fabrication

A schematic and an SEM image of a fabricated prototype is shown in Fig. 4.1. In this design stubs on both sides of the mesas were employed to further push the zero-index resonance up in frequency. A double-sided-stub design would have half the shunt inductance L_L per unit cell and exhibits higher shunt resonance frequency $\omega_{\text{sh}} \cong \sqrt{2}\frac{1}{\sqrt{C_R L_L}}$ (assuming $C_g \gg C_R$) as opposed to a design with stubs

Table 4.1: Tuning of the zeroth-order resonance frequency with stub widths

Stub width w_s (μm)	Shunt resonance $\omega_{sh}/2\pi$ (THz)
2	2.240
3	2.394
4	2.460

on one side. This was necessary as the peak gain bandwidth of our active QC material was within $2.4 - 2.7$ THz. Moreover, a double-sided-stub design would result in a symmetric radiation pattern which is more desirable. Static tuning of the shunt resonance frequency is achievable by varying the width of the stubs as reported in table 4.1.

The 5-μm-thick epitaxial growth NG-B17952 was used for fabricating metamaterial devices. Following the standard waferbonding (Cu-Cu) and substrate removal explained in section 2.2.2, waveguide mesas were first defined using a diluted Phosphoric acid and Hydrogen Peroxide etch (H_3PO_4:H_2O_2:H_2O::10:10:250) and a photoresist mask (Shipley SPR770). A thin PECVD oxide layer ($80 - 100$ nm) covering the sidewalls and the ground plane was deposited prior to top contact evaporation to isolate bonding pads from the ground plane and avoid DC shorting the MQW modules. Windows were opened in the oxide layer on top of the ridges for electrical contact to the devices using BOE etch. Top metal contact (Ti/Au::30/200 nm) as well as stubs metallization were then introduced by a single metal evaporation using lift-off process. A short clean-up etch (NH_4OH:H_2O_2:H_2O::5:3:490 for 30 seconds) was performed right before metal evaporation for surface cleaning and to promote better adhesion of the top metallization. It should be noted that the last two photolithography steps were done on non-flat surfaces which required resist spinning at lower speeds (2000 rpm) for uniform coverage specially on the sidewalls of the 5-μm-tall mesas. Two fabricated prototypes are shown in Fig. 4.2. Note the 45° slope of the sidewalls.

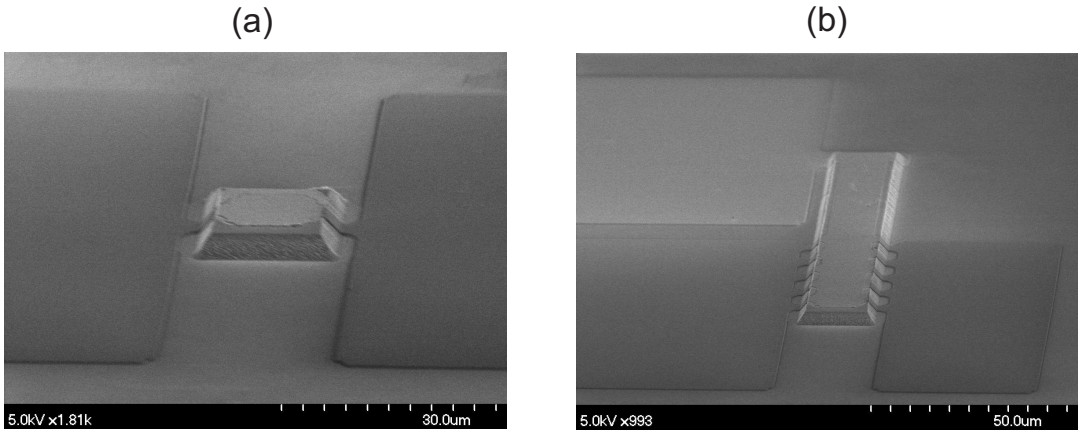

Figure 4.2: SEM image of (a) a single unit cell LC resonator, and (b) a compound metamaterial-MM waveguide cavity fabricated by wet etching H_3PO_4:H_2O_2:H_2O (10:10:250). Active region is 5-μm thick.

Mesas should be aligned to the major flat (110) direction in the wet-etch step to obtain such outward slopes that makes metallization on the sidewalls possible.

4.1.2 Experiments

The first device tested from this batch was a Fabry-Pérot laser ridge of dimensions 150 μm$\times$1.1 mm with cleaved facets to verify the fabrication quality. Experimental results are summarized in Fig. 4.3. Compared to the QCLs fabricated with dry etching, this device exhibited a relatively lower $T_{\max}$ of 98 K in pulsed mode and slightly higher threshold current densities (Fig. 2.11). Several metamaterial devices of various lengths, similar to the one shown in Fig. 4.1, were tested subsequently. Nonetheless, no signs of lasing threshold in collected $L-I$s and/or $I-V$s was observed from any of the devices (see Fig. 4.4). Indeed the smallest device from which lasing was observed was an 85μm$\times$630 μm metal-metal Fabry-Pérot laser ridge with 4-μm-wide stubs on one side. This indicated that for metamaterial devices, with approximately 25 times smaller sizes, there was not nearly enough gain in the active QC material to equalize ohmic losses. To rule out the

effect of extra ohmic loss due to conduction currents in the stubs and/or coupling capacitor pads, Fabry-Pérot metal-metal microcavities of identical dimensions to the metamaterial devices (10 μm$\times$200 μm) with no metallization on the sidewalls were also tested that did not lase. Since it would only take an extra $1-2$ cm^{-1} of bulk intersubband gain to bring the microcavity structure to lasing threshold as compared to a wide-ridge metal-metal waveguide, the question was what could be the source of additional loss in the structure. For narrow-ridge waveguides, the variation in ridge width from the top to the bottom of the wet-etched mesa can in fact contribute significantly to loss of gain within the QC-structure. Since current I has to be continuous throughout the QC structure (in the growth direction), current density J varies from module to module (up to a factor of 2) which at a given bias may cause an early onset of NDR, hence loss of gain, in MQW modules close to the top of the ridge. This is of course not an issue for wide-ridge ($\geq$ 100 μm) metal-metal waveguides where a 10 μm variation in ridge width would only translate to a maximum of 10% difference in J from module to module. It turned out that wet-etched design was misguided by the ease of fabrication process and high-aspect ratio sidewalls ($80-90^{\circ}$) were indeed required for a 10-μm-wide mesa to obtain lasing with achievable QC material gains —verified in our group via numerical simulations [142].

4.2 Generation II: Dry-Etched Mesas

While the sidewall slope in GaAs/AlGaAs wet etching is dictated by the crystallographic planes, this slope can be adjusted in a controllable fashion in a dry etch by varying RF power(s). In an ICP-RIE dry etch machine the ratio of the ICP to RIE powers mainly determines the aspect ratio of the etch independent of the orientation of etch mask with respect to crystal axes. Figure 4.5 summarizes

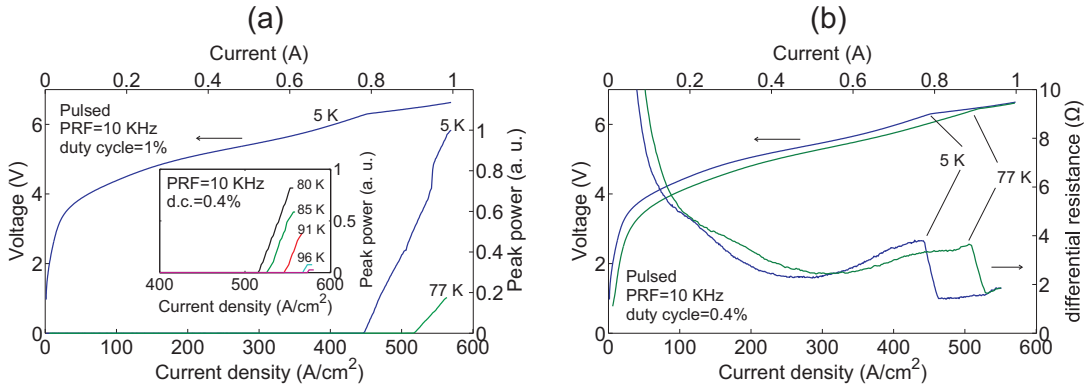

Figure 4.3: Experimental results for NG-B17952 measured from a wet-etched MM (Cu-Cu) Fabry-Pérot laser ridge of dimensions 150 μm×1.1 mm with cleaved facets. Temperature-dependent pulsed $L-I$s were recorded using a He-cooled Ge:Ga photodetector.

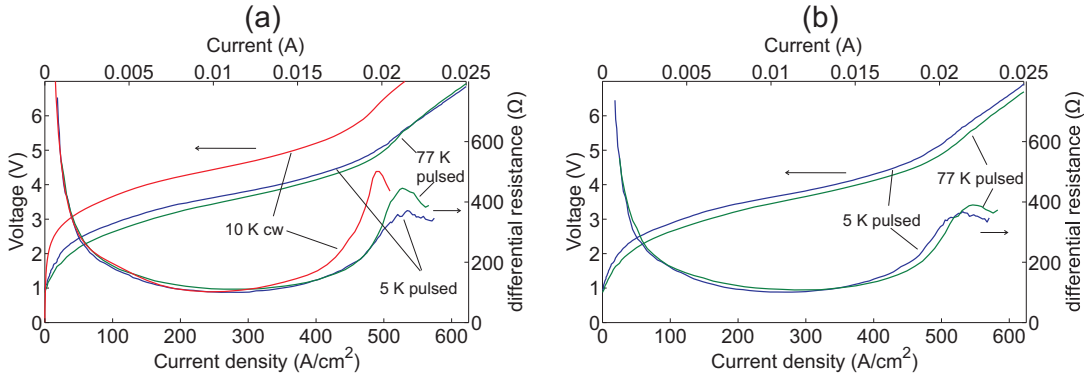

Figure 4.4: Pulsed (duty cycle = 0.4%) and cw $I-V$s for (a) a metamaterial device of dimensions 10 μm×200 μm and 3-μm-wide stubs on both sides, and (b) a metal-metal Fabry-Pérot ridge of identical dimensions (10 μm×200 μm) with no metallization on the sidewalls. Current densities were calculated based on the width of the devices at the bottom of the mesa (20 μm).

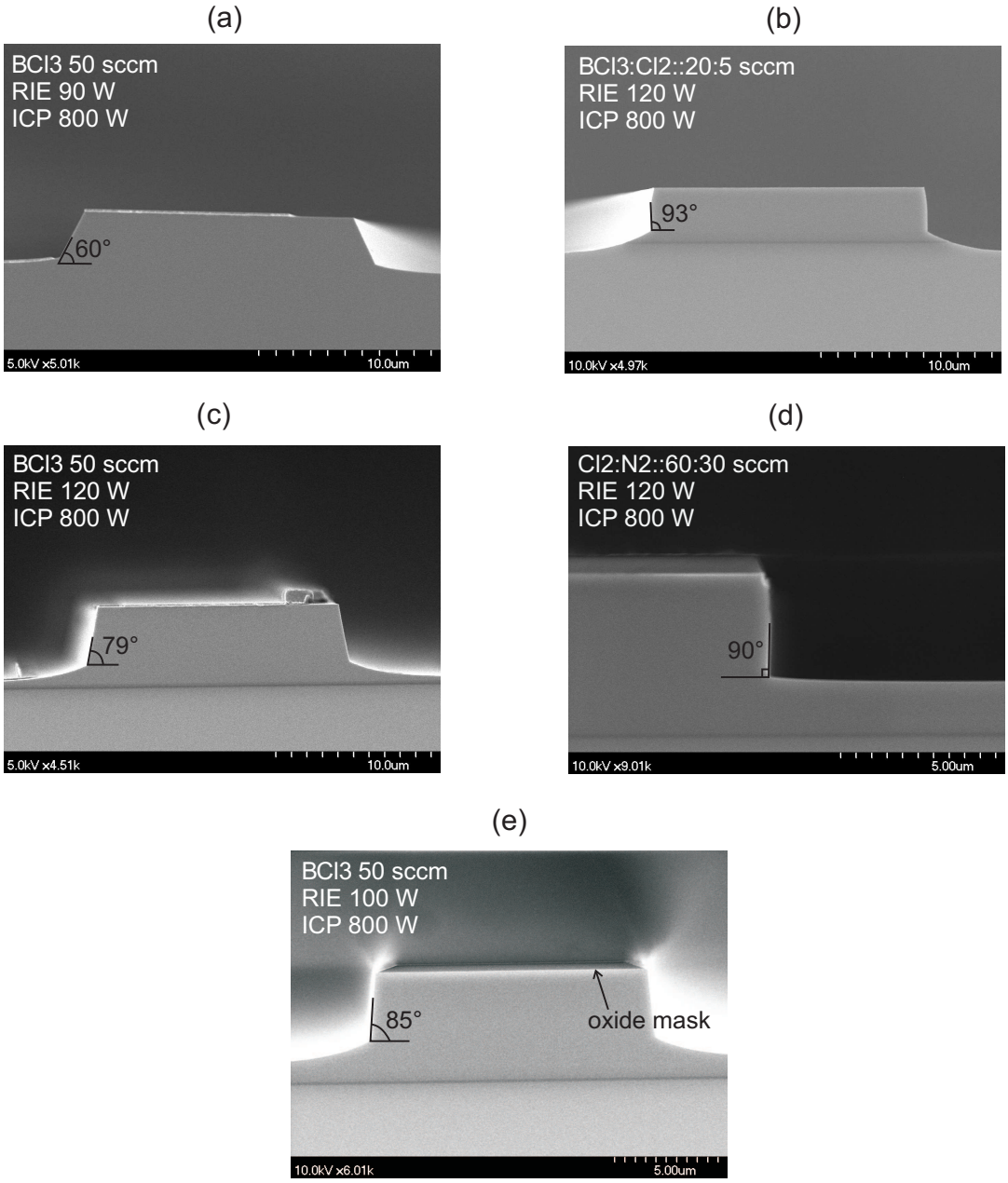

Figure 4.5: SEM images of dry-etched mesas in Chlorine-based gaseous plasma. All etches were performed with the chuck temperature and chamber pressure set to 21°C and 10 mT, respectively. Mask material was a 9000 Å PECVD oxide defined by wet BOE etch.

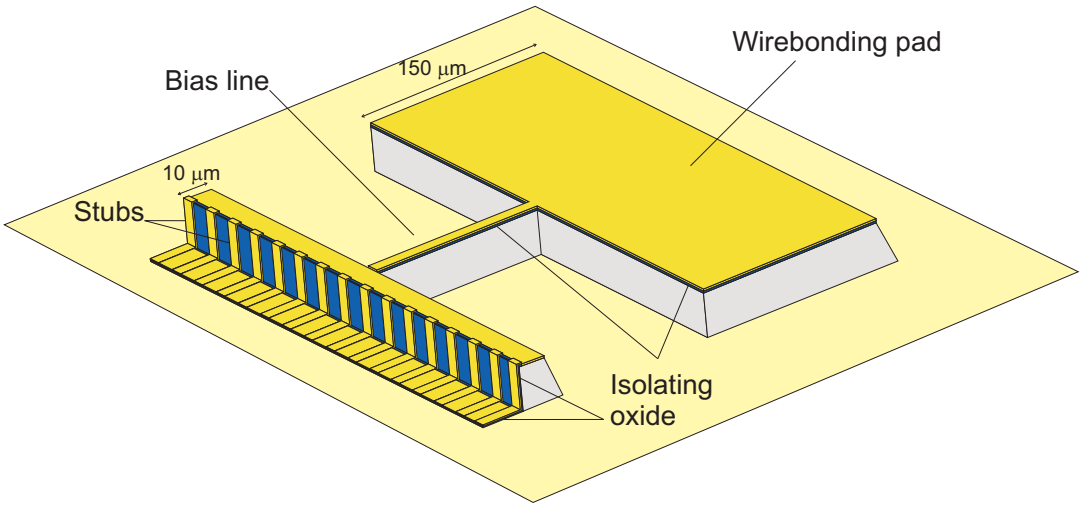

Figure 4.6: Schematic diagram of the modified terahertz metamaterial design with mesas defined by dry etching with an 85° slanted sidewall.

the results obtained from GaAs/$Al_{0.15}Ga_{0.85}As$ dry etching using Chlorine-based gases. The best results were obtained with pure BCl_3 gas and nominal RF powers of 100 W and 800 W for the RIE and ICP, respectively. Moreover, we found out that the use of an oxide mask was crucial so was the use of wet etching (BOE) for the hard mask definition. The isotropic nature of the BOE etch leaves the oxide mask with sufficient positive slope at the edges that is transferred to the mesa sidewall during the dry etch. This combination of gas chemistry, RF powers, and hard mask material would yield relatively smooth sidewalls with $80-85°$ positive slope (see Fig. 4.5(e)).

4.2.1 Design and Fabrication

Once a repeatable dry etch recipe was established, the design and fabrication process of the metamaterial waveguides were modified accordingly to address the shortcomings of the previous approach. Major modifications introduced in this generation were as follows:

- Mesas with $80-85^{\circ}$ sidewall slope were utilized. Zero-index frequency was further increased due to change in mesa sidewall slope. Shorter length of the stub "vias" resulted in smaller shunt inductance L_L per unit cell and higher shunt resonance frequency ($\omega_{\text{sh}} \sim 2.67$ THz). For such a design estimated threshold gain values to equalize radiative and metallic ohmic losses were 21 cm^{-1} and 94 cm^{-1}, respectively.

- Top contact metallization was evaporated first to avoid poor contact quality/adhesion due to any surface contamination during the fabrication process. Top metallization was deferred until the very last step in the previous generation due to enhanced etch rate of GaAs in (Phosphoric) acid etchant near exposed metals that would cause undercutting/overhanging of metal.

- While inductive stubs would still couple to the ground plane capacitively, in the new design these pads were not used for wirebonding to avoid many of the challenges encountered during wirebonding previous devices. Instead, separate large-area wirebond pads located on top of electrically isolated mesas were included in the design. The idea is shown schematically in Fig. 4.6.

For fabrication the 5-μm thick epitaxial growth of NG-B17952 was used. Top metal contact (Ta/Cu/Au::20/100/50 nm or Ti/Au::30/200 nm) was evaporated first followed by a thick PECVD oxide ($800-900$ nm) deposition that would serve as the etch mask for definition of waveguide mesas and bonding pads. After dry etch the etch mask residue was removed in BOE and a thin oxide layer (2000 Å) was deposited to electrically isolate the mesas sidewall and the bonding pads. Sidewall metallization and Au wirebond pads were defined last. While attempted several times, none of the devices fabricated using this approach saw the light of the day. Indeed many challenges were faced during the course of

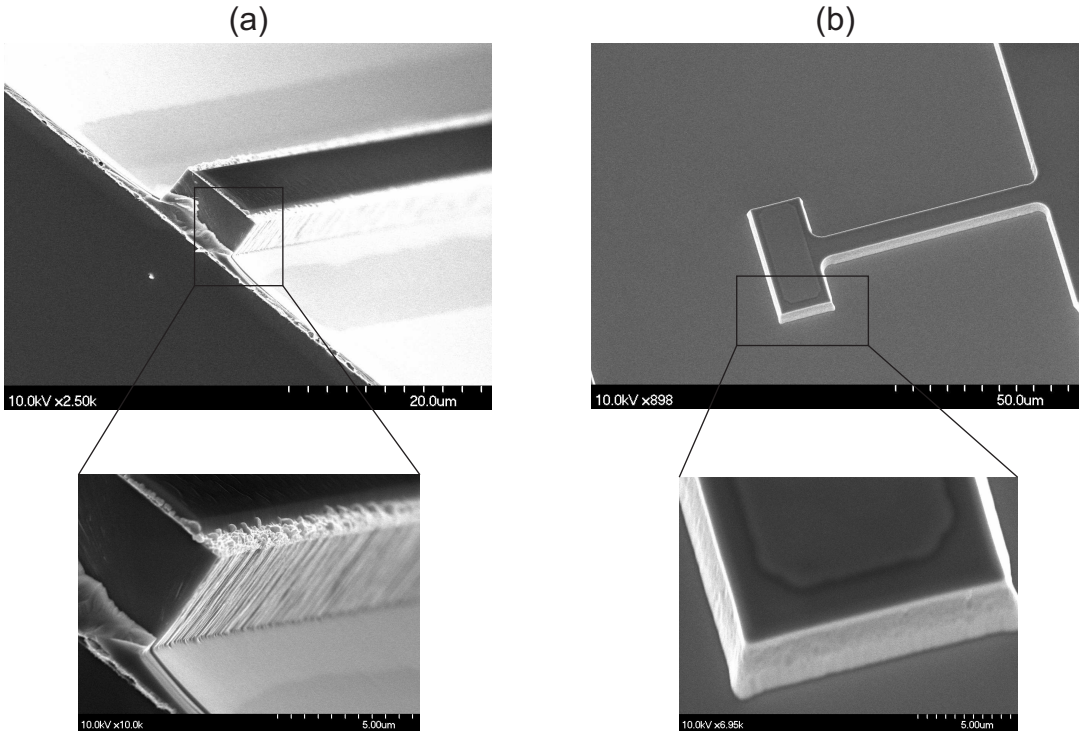

Figure 4.7: SEM image of (a) cleaved facet of a damaged metamaterial waveguide with exposed metal on the sides, and (b) a metamaterial waveguide cavity connected to the bias line and bonding pad that did not survive the BOE etch.

this processing including (a) improper lift off of Ta/Cu/Au most likely due to overheating the photoresist during Ta evaporation step, (b) exposure of top metal edges during mesa definition with dry etch which resulted in rough waveguide sidewalls (Fig. 4.7), (c) partial or in some cases complete delamination of top metal contact during etch mask residue removal due to severe undercutting of Ti in BOE etchant, and (d) accumulation of photoresist near the corners at the bottom of the mesas. All this rendered the fabrication of inductive stubs extremely challenging if not impossible.

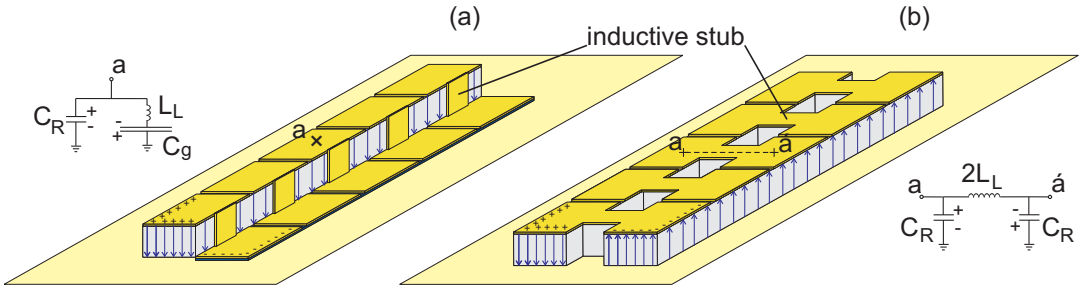

Figure 4.8: Schematic diagram showing the evolution of the metamaterial designs. (a) non-planar design based on the fundamental TM_{00} mode, and (b) planar realization of the same concept obtained by replacing the coupling capacitor insulating material with active QC material and operating in the higher-order TM_{01} mode. Insets: Equivalent circuit models at ω_{sh} for each design.

4.3 Summary

This chapter discussed many different designs that were investigated in the initial phase of the development of terahertz transmission-line metamaterials. Designs utilizing 45°-slanted sidewalls, fabricated by wet anisotropic etching of GaAs, were presented. These designs were limited in available gain in QC material due to current spreading in a wet-etched narrow-ridge metamaterial waveguide. In particular waveguide ridges with high-aspect ratio sidewalls are required to preserve current density uniformity, and gain, throughout the 5-μm-thick QC active material. For that purpose, an optimized dry etch recipe suitable for realization of waveguide mesas with 85° sidewall slope was developed and attempted for the metamaterials fabrication. While none of these designs were practical, a great deal of insight for fabrication of working devices was obtained. With slight modifications, the non-planar design of section 4.2 eventually led to an operational design which will be discussed in chapter 5. It turned out that a transition to a planar realization was necessary. Figure 4.8 shows the evolution of the original non-planar metamaterial design into a planar scheme which works based on a mode with odd lateral symmetry (TM_{01} mode of the waveguide).

CHAPTER 5

Active Leaky-Wave Metamaterial Antennas

As of August 2010, our interest shifted towards "planar" metamaterial waveguide designs that would operate in their first higher-order lateral mode (TM_{01} mode). This was partially due to the fabrication challenges associated with the original design of [140] (chapter 3) as well as higher radiation efficiency achievable with the planar design [67,89]. The planar design was inspired by the LC circuit-based resonator of Walter *et. al.* [143]. A similar design has been demonstrated in the microwaves [144] as a traveling-wave antenna. In this chapter, I demonstrate the leaky-wave characteristics of such a one-dimensional (1-D) terahertz metamaterial waveguide by using it as an active coupler antenna for a THz QC-laser.

5.1 Design

The concept is illustrated in Fig. 5.1(a). It is comprised of two closely-spaced transmission lines with subwavelength transverse dimensions (5 μm tall, 6 μm wide) coupled to each other via narrow inductive current paths. These paths play the role of the shunt inductance L_L which was originally realized in the Ref. [140] design by introducing vertical stubs on the waveguide sidewall to provide current paths to the ground plane. This requirement has been removed in this planar design by moving the virtual ground to the center of the shunt inductance L_L, i.e. symmetry plane of the structure. There are two major advantages to this scheme.

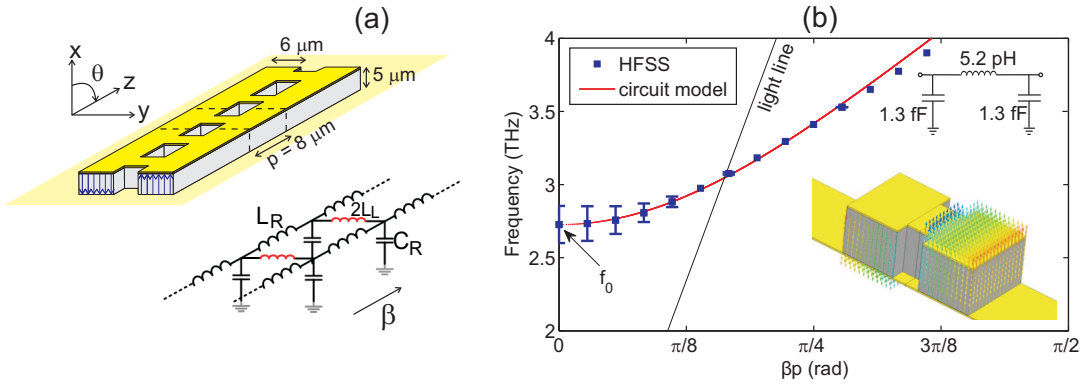

Figure 5.1: (a) Schematic representation of the 1-D metamaterial waveguide designed to operate in an odd lateral mode and its equivalent transmission-line model. (b) Dispersion characteristic of the structure obtained by full-wave finite element simulations from a unit-cell analysis and a fit by circuit model with $C_R = 1.3$ fF, $L_R = 2.7$ pH, and $L_L = 2.6$ pH. Inset shows a unit-cell with the electric field profile of the odd mode.

First, this approach does not require metallization on ridge sidewalls or virtual ground capacitors, which eases fabrication and reduces ohmic losses[1]. Second, this structure is designed to operate in a lateral mode with odd symmetry, i.e. opposite sign of electric field in each branch. Compared to the design of Ref. [140], which operates in the fundamental waveguide mode, this structure radiates more efficiently in the broadside direction due to constructive interference of radiating dipole sources on the waveguide sidewalls [67].

We consider a "gapless" design, to begin with, which lacks the series capacitance C_L, and only exhibits the right hand portion of CRLH leaky-wave behavior. Discussion on the addition of series capacitors to achieve backwards wave (left-handed) propagation is deferred to section 5.4. One can envision such a waveguide as a periodic cascade of unit cells, where each unit cell is composed of an LC resonator [143] (two capacitors in series with an inductor). Dispersion behavior of such an infinite periodic metamaterial reveals that the zero-index

[1]The loss produced by the virtual ground capacitors was estimated to increase the threshold gain by $50 - 70$ cm^{-1}.

resonance occurs at $\omega_{\text{sh}}/2\pi = \frac{1}{2\pi\sqrt{L_L C_R}} = 2.7(\pm 0.1)$ THz with the light cone ($0 < n_{\text{eff}} < 1$) extending to 3.0 THz (Fig. 5.1(b)). The dispersion relation was calculated from full-wave finite element simulations of the complex eigenfrequencies of the waveguide odd mode using periodic boundary conditions. The uncertainty bars for the calculated eigenfrequencies represent the strength of radiative losses ($\Delta\nu = 2\Im\{\nu\}$). Operation within the light cone is accompanied by a penalty in loss, primarily due to highly efficient radiative coupling, but also due to a modest increase in metallic losses compared to conventional Fabry-Pérot (FP) modes. For example, we calculate that an infinitely-long self-resonating cavity of this design lasing in the zero-index mode requires 100 cm^{-1} and 19 cm^{-1} of intersubband gain to overcome radiative and metallic losses, respectively. These threshold gain values were obtained in a similar fashion described in chapter 3, except that ports were placed in the transverse direction and by employing proper symmetry boundary conditions (perfect magnetic walls), only one unit cell was analyzed instead of five. This allowed a more accurate estimation of threshold gain values at the zero-index resonant frequency as finer finite element meshes were employed in our simulations.

While the shunt resonance frequency is determined in this design to the first order by the effective width of the waveguide ($w \sim \lambda_{\text{g}}/2$), little tuning of ω_{sh} as well as optimization of radiative losses are possible by varying the widths of the stubs. In the language of transmission-line metamaterials, narrowing the inductive paths leads to a larger shunt inductance L_L, and reduces the shunt resonant frequency. The change in the shunt capacitance C_R is not substantial since the electric field is a null in the center of the ridge. Lower shunt frequency also translates to smaller size of the radiating dipoles on the sidewalls (in the vertical direction) with respect to wavelength which makes them less efficient radiators. A comparison of the radiative losses for a fixed waveguide width and

Table 5.1: Threshold gain values for the zeroth-order resonant mode for different stub widths

w_s (μm)	$\omega_{sh}/2\pi$ (THz)	$g_{th,\,rad}$ (cm^{-1})	$g_{th,\,met}$ (cm^{-1})	$g_{th,\,tot}$ (cm^{-1})
6	2.690	97	13	110
5	2.660	88	20	108
4	2.615	80	27	107
3	2.550	68	35	103

varying stub sizes is presented in table 5.1. In the extreme case where the stub width is identical to the unit cell period $p = 8$ μm, a narrow MM waveguide operating in its TM_{01} mode is recovered. This is analogous to a microstrip patch antenna, where the patch supports a half-wavelength resonance, and the two "radiating slots" dominate the radiative process. The calculated threshold gain values[2] confirm the trend in radiative losses qualitatively explained here. While the losses of this design are too large to allow use as a laser resonator, the strong radiation coupling suggests that such a structure would be an efficient antenna.

5.2 Fabrication

The fabricated prototype consists of a compound cavity with the metamaterial antenna (408 μm long) fed by a metal-metal QC-laser cavity of 390 μm length and 25 μm width (see Fig. 5.2(a)). The metal-metal waveguide section is designed to serve as a master oscillator laser that feeds the antenna with the desired mode of odd lateral symmetry. The antenna, however, is active and can be separately biased to provide amplification. The active region was based on a resonant-phonon depopulation scheme, in a four-well design (FL86Q). The GaAs/$Al_{0.15}Ga_{0.85}As$ quantum well heterostructure was grown by molecular beam epitaxy with 86 cas-

[2]Ohmic losses due to finite conductivity of the Au metallization was incorporated using a Drude conductivity with $n = 5.9 \times 10^{22} cm^{-3}$, $\tau = 60$ fs, $m^* = m_0$, $\epsilon_{core} = 1$.

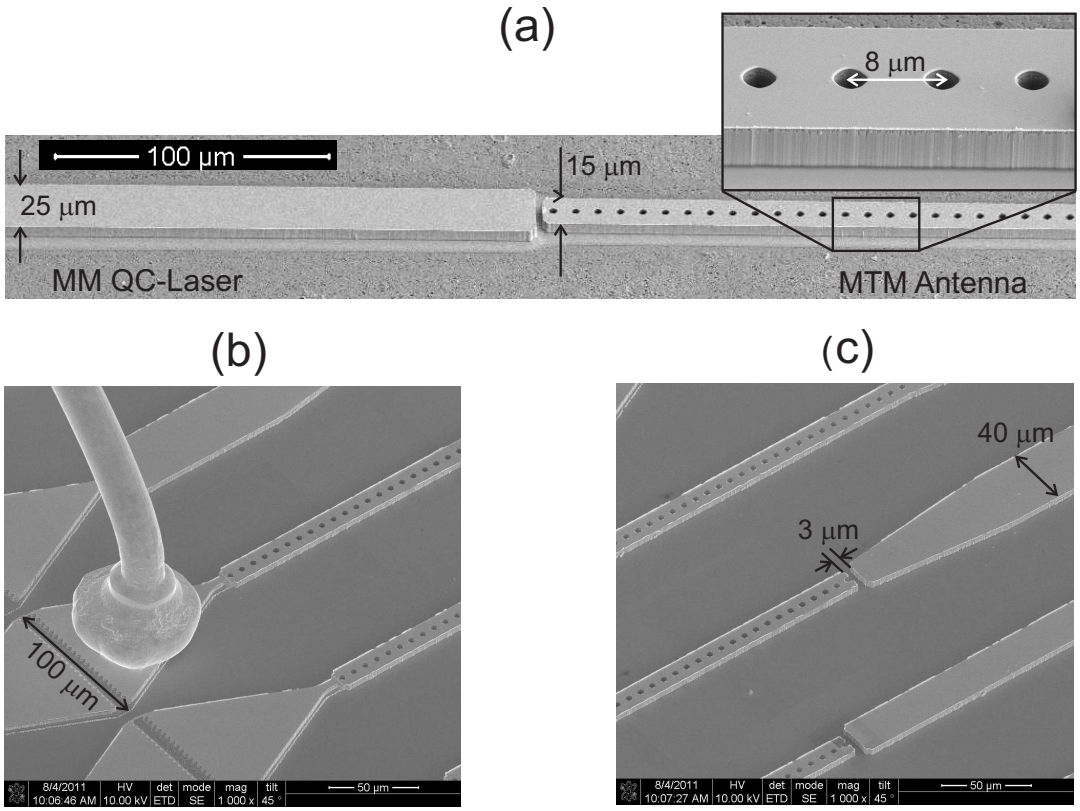

Figure 5.2: SEM image of the fabricated leaky-wave metamaterial antenna fed by a THz QC-laser source. Tapered terminations serve both as a preferential selection mechanism for the odd lateral mode and electrically isolated bonding pads.

caded modules to form a 5 μm thick active region (growth NG-B17952). The structure was fabricated in metal-metal waveguide technology using copper-to-copper thermocompression wafer bonding. The metallization for the top contact (Ti/Au/Ni::20/150/250 nm) was defined by contact lithography, and then used as a dry etch mask to define the ridges.

While it is desirable to operate the proposed planar design in its TM_{01} odd lateral mode, it would still support modes with even lateral symmetry, i.e. the fundamental TM_{00} mode. In the later case, the radiating magnetic dipoles associated with waveguide sidewalls interfere destructively in the far-field, hence

TM_{00} modes suffer less from radiation losses compared to TM_{01} modes. Moreover, there is no conduction current flowing in the transverse direction for the fundamental modes and ohmic losses only exist due to current flow in the longitudinal direction. As a result, TM_{00} modes tend to exhibit much less overall waveguide losses. Much of the success of the proposed planar design relies on the loss engineering of fundamental waveguide modes in favor of higher-order lateral modes such that the metamaterial would operate in a TM_{01} mode. One way to achieve this is to selectively increase facet loss for the fundamental modes. In our design, tapered terminations at the rear facets of the metamaterial antenna and the QC-laser were employed (shown in Fig. 5.2(b)) that serve both as a preferential selection mechanism for the odd lateral mode and electrically isolated bonding pads for DC bias. A thin (200 nm) oxide underneath these bonding pads serves as an electrical isolation layer. The concept is simple: an adiabatic taper from a narrow neck at the center of the waveguide ($\sim 3-6$ μm) to a large bonding pad ($\sim 100-150$ μm wide) provides a smooth transition for the fundamental TM_{00} mode with very little reflection at the facet. This is while the higher-order TM_{01} mode which is a null in the middle practically experiences no perturbation compared to the case without tapered terminations (See Fig. 5.3). Calculated threshold gain values also verified the effect of tapered terminations for selective excitation of higher-order modes. For instance, we estimate a 2 cm^{-1} increase in $g_{th,rad}$ for TM_{01} mode of this design whereas $g_{th,rad}$ increased by more than 200 cm^{-1} for TM_{00} once such tapered terminations were employed for a 40-μm long device (5 unit cells). Clearly, the total per-unit-length loss due to facet loss is inversely proportional to the length of devices which will affect the usable physical length for which this method is effective.

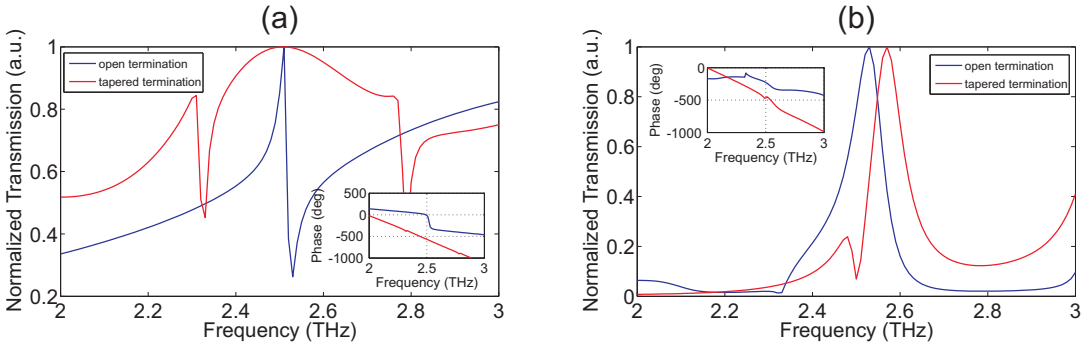

Figure 5.3: Normalized transmission magnitude ($|S_{21}|^2$) and phase ($\angle(S_{21})$) with and without tapered terminations at both ends of a 40-μm long device calculated for (a) fundamental TM_{00} lateral mode, and (b) higher-order TM_{01} lateral mode. The drastic change in FWHM (equivalently $Q = \frac{\nu_0}{\Delta\nu}$) is clearly observed for the TM_{00} whereas the Q stays almost the same for the TM_{01} mode.

5.3 Experiments

5.3.1 Far-Field Beam Patterns

For testing, devices were indium soldered onto a copper chip carrier and mounted on the cold stage of a cryostat. We examined polarization dependent 1-D far-field beam patterns of the device along with angle-resolved Fourier transform spectroscopy of the THz radiation to identify the metamaterial antenna operation within its leaky-wave bandwidth. The angular resolution of beam pattern and spectroscopy measurements were 1.5° and 3.4°, respectively. For all the measured data presented in this section, the metal-metal waveguide was biased above threshold with 5 μs pulses repeated at 10 KHz while the metamaterial antenna was unbiased and passive. A directive, single beam far-field pattern with full-width at half-maximum (FWHM) $\cong$ 15° at about 45° from broadside was observed (Fig. 5.4(a)). The frequency of radiation was measured to be 2.74 THz which is well within the calculated leaky-wave bandwidth of the antenna. The measured frequency and angle of the directive beam are approximately consis-

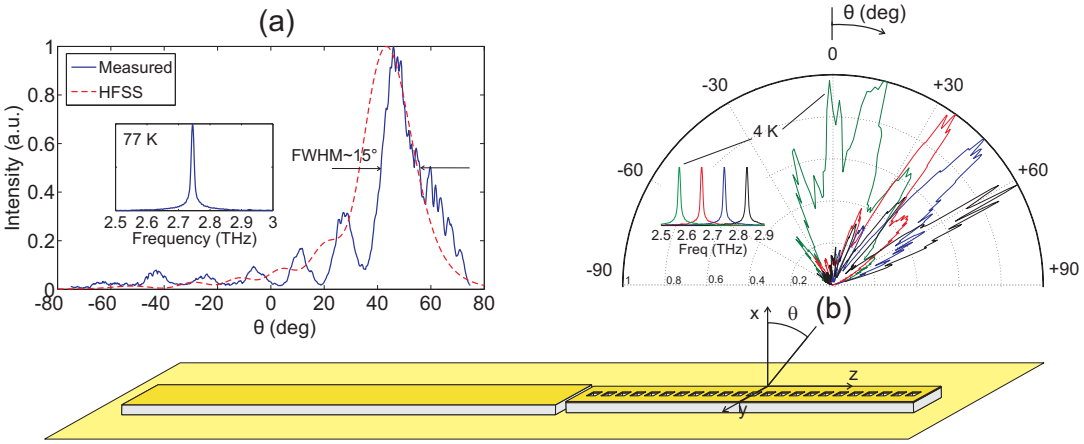

Figure 5.4: (a) Measured longitudinal cut of the far-field beam pattern at 2.74 THz, and (b) beam scanning with frequency (polar representation). Data was collected at 77 K with the QC-laser biased in pulsed mode (5 μs pulses repeated at 10 KHz) and the antenna passive. Inset shows the spectra collected at corresponding bias voltages $V_{MM} = 6.10$ (red), 6.20 (blue) and 6.30 volts (black). Data for the lowest excitation frequency of 2.57 THz, corresponding to the broad beam close to $\theta = 0$ (green), was collected at 4 K.

tent with the calculated dispersion relation of Fig. 5.1(b). A slight discrepancy between the measured and predicted beam pattern side-lobe levels in the longitudinal cut exists, which may be attributed to reflections from the other end of the antenna.

Within the light cone, the direction of radiation main beam is dictated by the metamaterial waveguide dispersion relation according to $\theta_{MB} = \sin^{-1}(\beta(\omega)/k_0$ (equation (3.6)). By changing the bias on the metal-metal QC-laser, we force the laser to hop between different axial modes, which allows us to excite the antenna at several discrete frequencies; the corresponding beam patterns are shown in Fig. 5.4. Beam scanning from $35° - 60°$ is observed as the lasing frequency of the QC-laser varies from $2.65 - 2.81$ THz. For the lowest excitation frequency of 2.57 THz, for which we expect emission close to broadside ($\theta = 0$), the beamwidth is significantly larger, likely due to the short extinction length of the THz mode

in the lossy leaky-wave antenna. This effect is attributed to the reduced group velocity $v_g = \mathrm{d}\omega/\mathrm{d}\beta$ near ω_{sh}, which leads to an increased extinction coefficient α. For instance, from the dispersion diagram of Fig. 5.1(b), one would calculate a loss coefficient of $\alpha \approx \frac{\mathrm{d}\beta}{\mathrm{d}\nu}\Delta\nu = 80-400\ \mathrm{cm}^{-1}$ within the light cone, corresponding to an extinction length of $\alpha^{-1} \sim 55 - 285\ \mu$m which is much shorter than the physical length of the antenna. The reduced extinction length results in a very short effective emitting aperture and a broad beam. Sidelobe levels as well as beamwidth may be reduced, however, by reduction of the radiative losses — for example by reducing the height— and/or active biasing of the metamaterial antenna. Nonetheless, this method provides an experimental approach to measure the dispersion of the metamaterial waveguide within its leaky-wave bandwidth.

The detected THz radiation is polarized in the direction perpendicular to the antenna axis. This is characteristic of the radiation from this transmission-line metamaterial, and opposite of what one would expect from a metal surface Bragg grating. Occasionally, for some devices the metal-metal QC-laser oscillates in its fundamental lateral mode, for which the antenna does not exhibit leaky-wave behavior. The beam patterns are dramatically different in that case; they are non-directional with strong fringes in the far-field, typically with detectable powers of order(s) of magnitude smaller and are polarized along antenna axis. Figure 5.5 shows a longitudinal cut of the beam pattern for the leaky-wave antenna when fed by a master oscillator THz QC-laser operating in the TM_{01} mode (at 2.81 THz) and the TM_{00} (at 2.50 THz) mode. For the TM_{01} mode, the detected radiation is dominantly polarized in the direction perpendicular to the antenna axis, which corresponds to E_y components. The TM_{00} mode, on the other hand, exhibited a non-directional beam pattern with many fringes in the far-field and is polarized primarily along the axis of the waveguide, corresponding to E_z components, and is an order of magnitude lower in intensity.

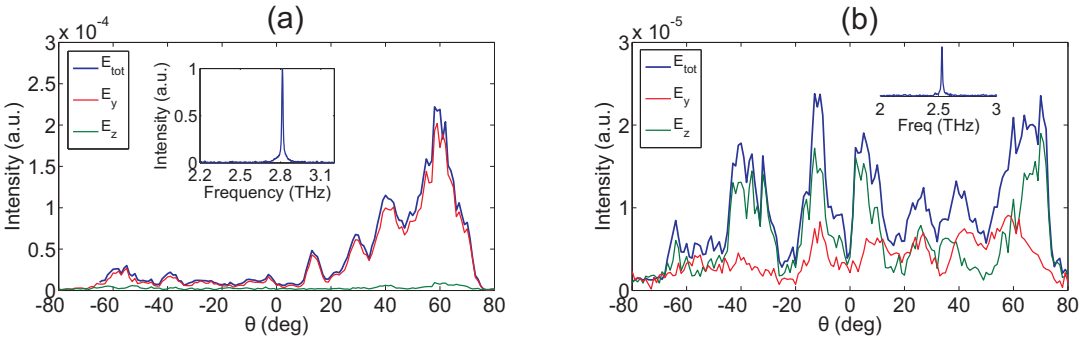

Figure 5.5: Measured far-field beam patterns and spectra at two different bias points corresponding to metamaterial operation in (a) its TM_{01} (higher-order) mode within the light cone, and (b) TM_{00} (fundamental) mode outside the fast-wave region. Data was collected at 77 K with the QC-laser biased in pulsed mode (5 μs pulses repeated at 10 KHz) and the metamaterial antenna passive.

5.3.2 Power Amplification

As was mentioned earlier the metamaterial antenna can be separately biased to provide amplification. In this section I experimentally show how the active leaky-wave antenna may be used to realize a master-oscillator power-amplifier (MOPA) device. For the measured data presented in Fig. 5.6, the metal-metal waveguide QC-laser was operated at a fixed DC bias (in cw mode) beyond its lasing threshold while the metamaterial antenna was separately biased in pulsed mode (1 μs pulses repeated at 10 KHz). Terahertz power was detected using a LHe-cooled Ge:Ga photodetector in a differential scheme with the lock-in amplifier synchronized to the bias pulse train on the antenna. A relatively narrow beam (FWHM $\sim 15^\circ$) is observed at about 40° from broadside direction, which grows in intensity as the bias on the antenna is increased. This is an indication of power amplification due to addition of gain in the antenna section. The frequency of radiation at $40^\circ(\pm 5^\circ)$ was measured to be 2.74 THz which is well within the leaky-wave bandwidth of the calculated dispersion diagram. Further increasing the bias on the antenna section is accompanied by the onset of a broadside beam

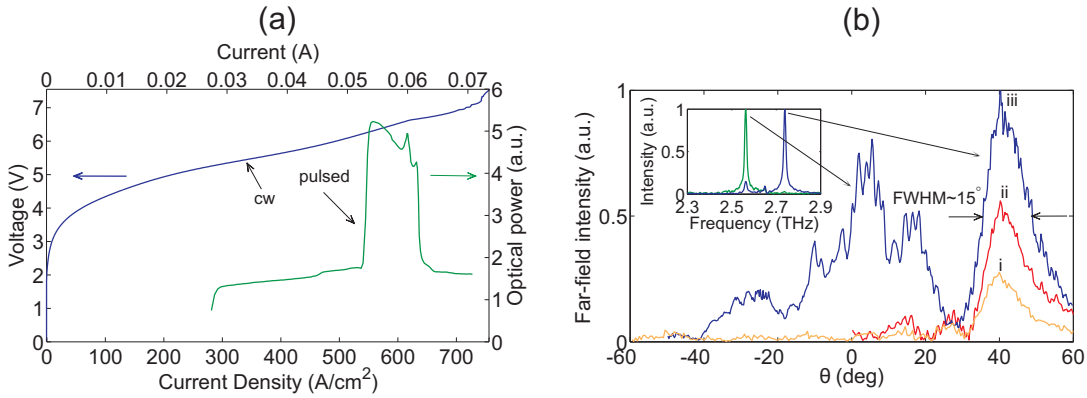

Figure 5.6: (a) CW current-voltage (I-V) and "differential" pulsed (1 μs pulses repeated at 10 KHz) light-current density (L-J) characteristic of the device at 4 K. Current density (bottom axis) is applicable to both metal-metal and metamaterial sections whereas the bias current (top axis) is only applicable to metal-metal section. (b) Measured 1-D far-field beam patterns with V_{MM} = 7.10 volts (cw) and V_{MTM} = 5.65 (i), 6.15 (ii), and 6.35 volts (iii) (pulsed). Inset shows the angle-resolved spectra collected at V_{MM} = 7.10 volts and V_{MTM} = 6.35 volts.

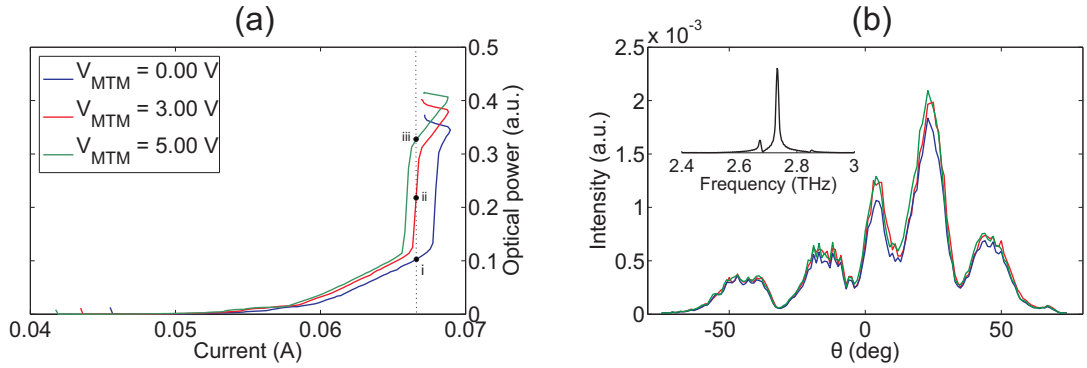

Figure 5.7: (a) Pulsed light-current (L-I) characteristic of the device at 4 K for various bias voltages on the metamaterial antenna. Horizontal axis corresponds to the total current drawn by the metal-metal section only. Both metal-metal and metamaterial sections where synchronously biased with identical pulse trains (5 μs pulses repeated at 10 KHz). (b) Measured 1-D far-field beam patterns with (i) V_{MM} = 5.16 V and metamaterial antenna passive, (ii) V_{MM} = 5.24 V and V_{MTM} = 3.0 V, and (iii) V_{MM} = 5.30 V and V_{MTM} = 5.0 V.

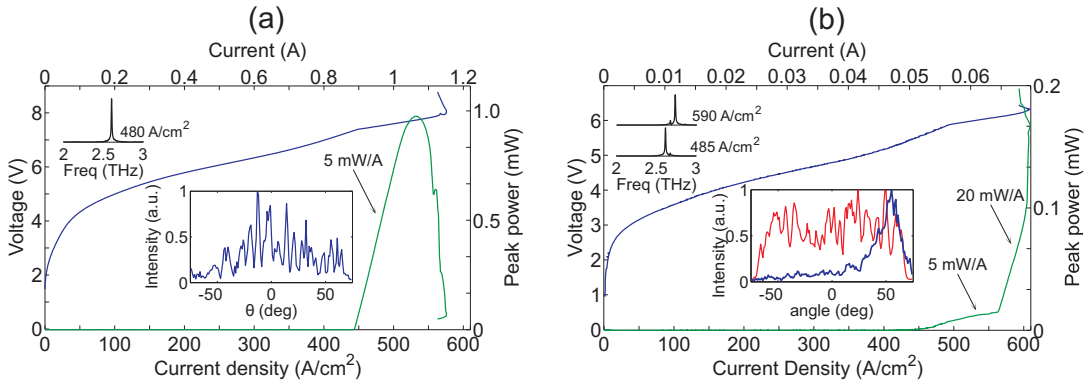

Figure 5.8: (a) Pulsed light-current-voltage (L-I-V) characteristic of a 2 mm long, 100 μm wide metal-metal FP cavity with cleaved facets. Inset shows a 1-D beam pattern along the length of the cavity for this device lasing in a single mode at 2.60 THz which is typical of the metal-metal QC-laser. (b) L-I-V curves of an antenna-coupled device with the metamaterial antenna passive. Insets show the spectra of radiation at two different bias current densities (top left) and 1-D cuts of the beam pattern in the surface direction along the longitudinal (blue) and transverse (red) directions. All data was measured using 5 μs pulses repeated at 10 KHz. Peak THz power was measured using a thermopile detector, with a collimating Winston cone in front of one facet for the FP cavity, and in the surface direction for the antenna structure with no collection optics in the cryostat.

which is measured to have a frequency of 2.56 THz, i.e. below the cut-off frequency f_0. This is attributed to a new mode that begins to lase within the master oscillator cavity, which couples to the antenna evanescently. Similar experiments were carried out with both the metal-metal waveguide QC-laser and the metamaterial antenna biased in pulsed mode (5 μs pulse trains repeated at 10 KHz). While power amplification was observed in the face-to-face L-I characterizations, no such evidence was found in far-field beam pattern measurements. This is somewhat unexpected result.

Lastly, the antenna-coupled device exhibits I-V characteristics and threshold current densities comparable to those of a conventional metal-metal Fabry-Pérot cavity fabricated from the same wafer. This is illustrated in Fig. 5.8, where for low bias current densities ($480-560$ A/cm^2), the master oscillator QC-laser lases

at 2.60 THz, outside the antenna leaky-wave bandwidth, resulting in a slope efficiency of ~ 5 mW/A similar to that of the Fabry-Pérot laser. At high enough bias current densities ($560-610$ A/cm^2), however, the antenna is fed with a 2.73 THz mode within its leaky-wave bandwidth which yields a much higher slope efficiency (~ 20 mW/A). While the antenna-coupled device is 20 times smaller in size, the peak detectable power is only 5 times smaller (~ 200 μW). This is attributed to higher radiation coupling and improved collection efficiency of the directive beam launched by the antenna. Nevertheless, the beam in the transverse direction is extremely broad due to the subwavelength width —an issue which can be addressed using array techniques [82].

5.4 Introduction of Series Capacitors

With the addition of series capacitance, this structure is suitable for development of an active THz CRLH transmission-line metamaterial. Figure 5.9 shows the effect of periodic addition of series capacitors C_L on the leaky-wave metamaterial antenna dispersion relation. Compared to the gapless design of Fig. 5.1, this structure exhibits CRLH properties such as left-handed propagation (for $f < 2.61$ THz) in addition to the right-handed propagation. Alternating gap capacitors of ~ 250 nm incorporated into the top metallization, results in a meander-type structure which is DC connected and can operate as an active CRLH antenna. This, however, increases the overall unit cell length to $p = 16$ μm, which translates to a larger series inductance L_R helping achieve a nearly balanced design with $\omega_0/2\pi \cong 2.61$ THz. The balanced CRLH design is particularly appealing as it maintains a nonzero group velocity even at $\beta = 0$, and hence a non-diverging power loss coefficient at the transition frequency ω_0 [67]. Moreover, impedance matching to a balanced CRLH transmission line is much easier than the right-

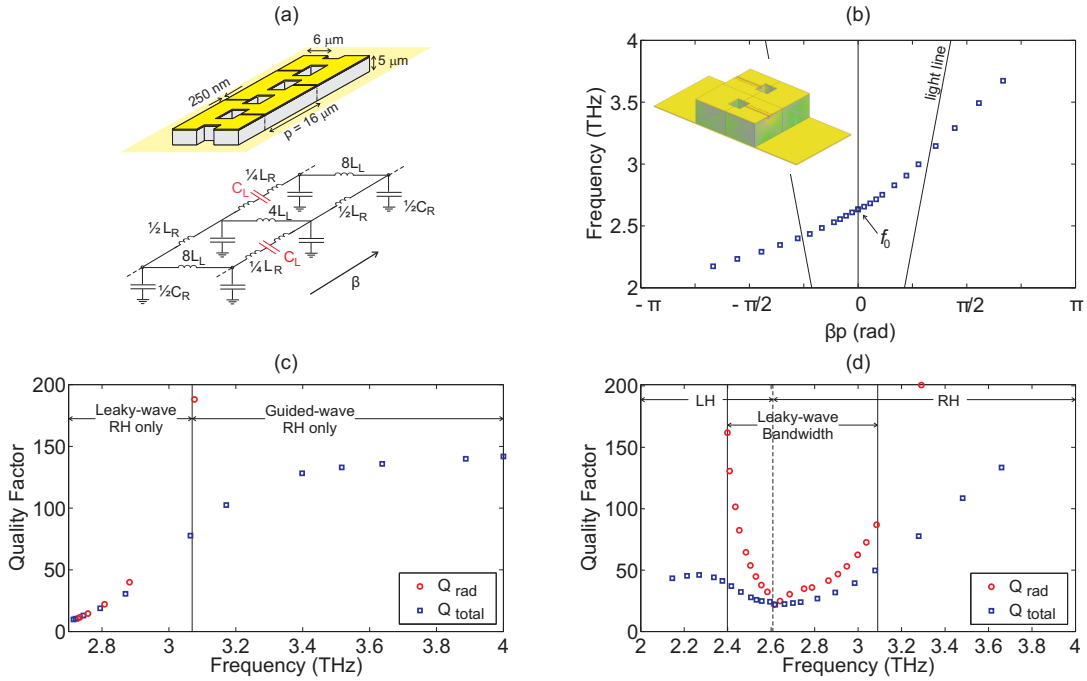

Figure 5.9: (a) Schematic representation of the 1-D metamaterial waveguide with the addition of staggered gap capacitors in the top metallization and its equivalent transmission-line model. (b) Dispersion characteristic of the structure obtained by full-wave finite element simulations from a unit-cell analysis. Inset shows the strong electric field (with opposite directions) in the gap capacitors. (c), (d) Eigenmode quality factors due to radiation loss only ($Q_{\rm rad}$), and radiation and ohmic metallic losses ($Q_{\rm tot}^{-1} = Q_{\rm rad}^{-1} + Q_{\rm met}^{-1}$) for the RH-only gapless design and meander-type CRLH metamaterial, respectively. A finite-conductivity Au metallization was incorporated in simulations using a Drude model with $n = 5.9 \times 10^{22}{\rm cm}^{-3}$, $\tau = 60$ fs, $m^* = m_0$, $\epsilon_{\rm core} = 1$.

handed-only gapless design as the Bloch impedance stays constant across the entire CRLH bandwidth [134]. Calculated quality factors due to both radiation ($Q_{\rm rad}$), and metallic losses ($\frac{1}{Q_{\rm tot}} = \frac{1}{Q_{\rm rad}} + \frac{1}{Q_{\rm met}}$) are shown in Figs. 5.9(c), (d) for the RH-only gapless design and meander-type CRLH metamaterial, respectively. Compared to the gapless design —where losses are dominated by radiation— the meander CRLH metamaterial exhibits significantly higher metallic losses particularly in the left-handed range. Moreover, $Q_{\rm rad}$ is larger in the CRLH design which may be attributed to the fact that in this structure, electric field energy can also be stored in C_L, which contributes negligible radiation due to the antisymmetric equivalent magnetic currents contributions within the gap capacitors. This is while for the gapless design all the electric field energy is stored in the shunt capacitors C_R, which is associated with strong radiation from the sidewalls. HFSS simulations also confirm the backward to forward scanning of the main beam for the CRLH metamaterial antenna of this design (see Fig. 5.10).

5.4.1 Fabrication

The structure was fabricated in metal-metal waveguide technology (Cu-Cu) using a 5 μm thick active region (growth NG-B17952 based on resonant-phonon design FL86Q). Similar to the gapless design, the fabricated prototype consists of a compound cavity with the metamaterial antenna (500 μm long) fed by a metal-metal QC-laser cavity of 500 μm length and 40 μm width (see Fig. 5.11). The process for definition of top metallization, however, had to be modified to accommodate the fabrication of submicron gaps in the antenna section. The metallization for the antenna top contact (Cr/Au::20/100 nm) was defined by electron-beam lithography using a bilayer of polymethyl methacrylate (PMMA) e-beam grade positive resists (495-A4 and 950-A2) and lift-off process. A short

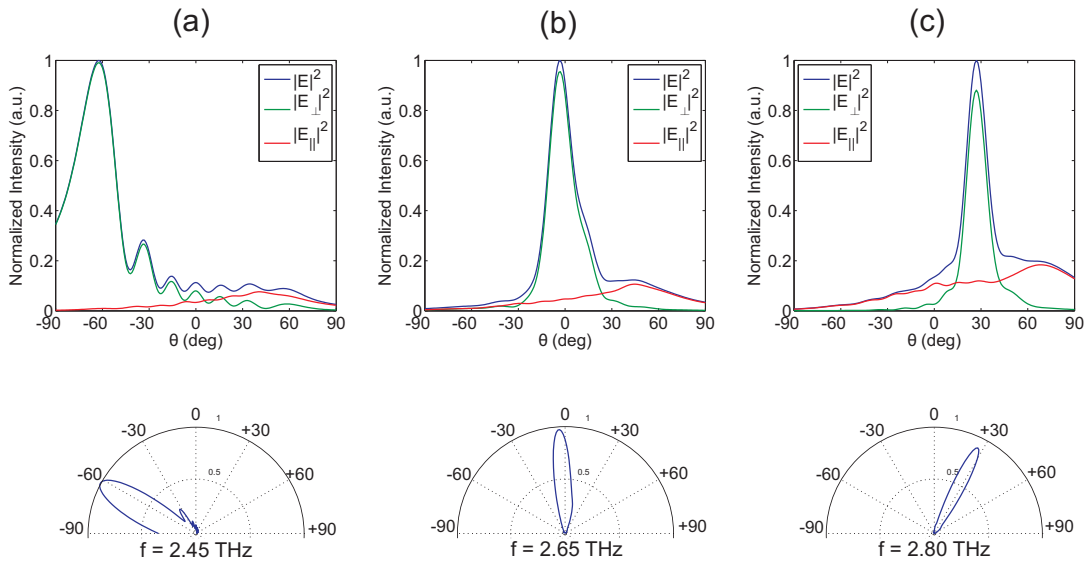

Figure 5.10: Simulated far-field beam patterns of the meander-type CRLH metamaterial antenna (480 μm-long) at three discrete frequencies within its leaky-wave bandwidth showing the scanning of the main beam angle with frequency. Components of the electric field transverse ($|E_{\perp}|$) and parallel (longitudinal) ($|E_{||}|$) to the antenna axis are shown for each frequency. E-field is dominantly polarized transverse to the antenna axis. Polar representation of the far-field beams are also presented.

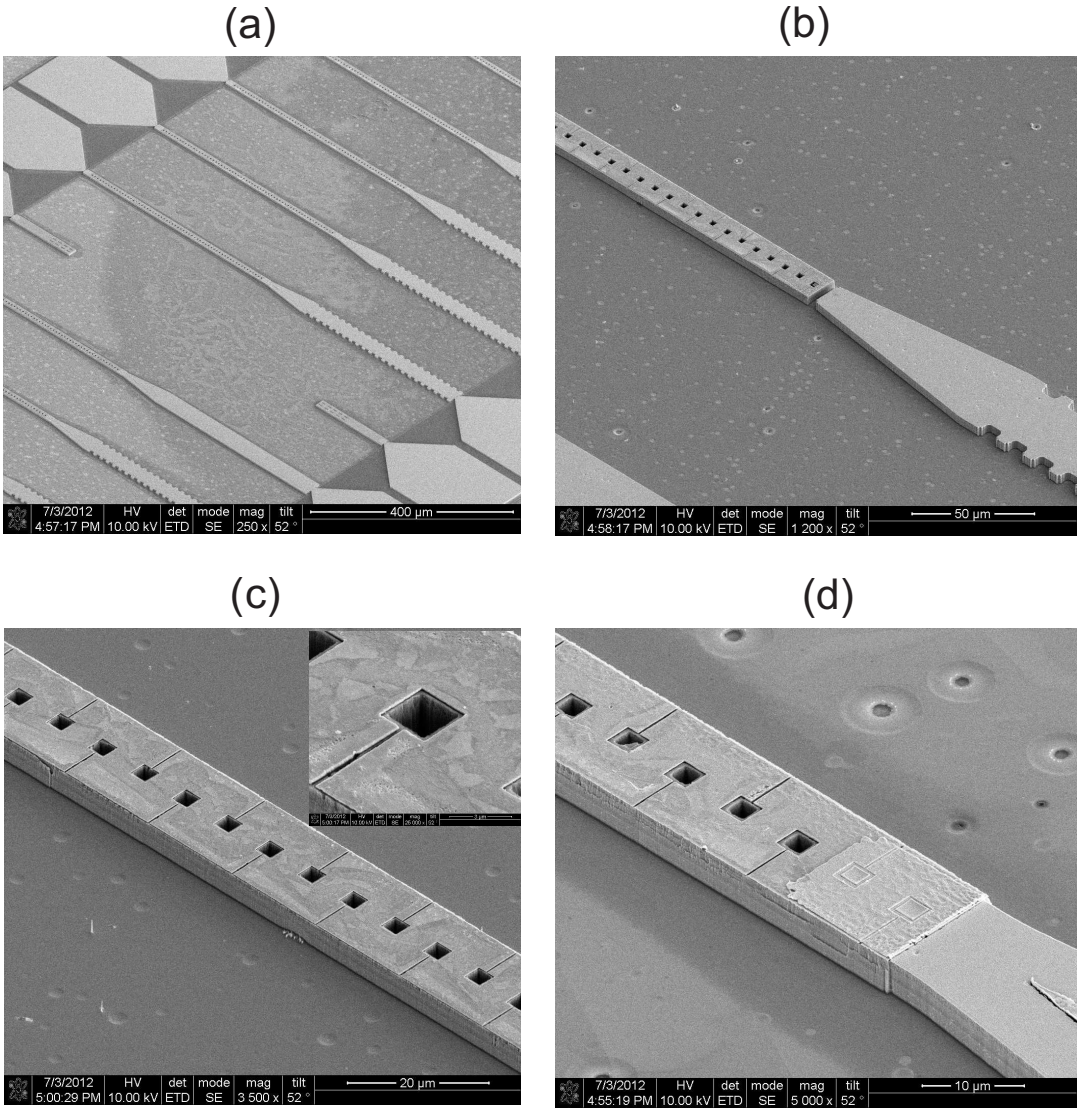

Figure 5.11: SEM image of fabricated meander-type CRLH metamaterial antennas fed by several THz QC-laser sources (a), and (b) a laterally corrugated metal-metal waveguide first-order DFB terahertz QCL coupled to a CRLH antenna with a 3 μm gap. (c) Close-up of the CRLH metamaterial waveguide with staggered gap capacitors in its top metallization. (d) An antenna-coupled device with no discontinuity at the QCL-to-antenna transition.

PA etch (NH_4OH:H_2O_2:H_2O::10:6:480 for 2 minutes) was performed prior to the e-beam lithography. This would remove any highly-doped n^+-GaAs layer present in the growth sequence to avoid shorting the gap capacitors. Dry etch mask for the antenna section was deposited by performing a second round of e-beam lithography/metal evaporation (Ni::200 nm) using the same bilayer of PMMA resists. Top metallization for the feed section and the bonding pads (Ti/Au/Ni::20/150/250 nm) was defined by contact lithography, which was also used as dry etch mask. Prior to this step 200 nm of PECVD oxide was deposited and patterned (using BOE) to electrically isolate the bonding pads from active gain material. Ridges were defined in GaAs dry etcher using BCl_3 gaseous plasma. A post-etch TFG Nickel etch[3] followed by a short clean-up PA etch (NH_4OH:H_2O_2:H_2O::5:3:490 for 20 seconds) was performed to remove any Ni residue from within the gaps which would otherwise short the series capacitors out.

5.4.2 Experimental Results

Several antenna-coupled devices were examined for their operation within the leaky-wave bandwidth of the CRLH metamaterial antenna, particularly in its left-handed range which is accompanied by a directive single beam launched in backward directions (negative angles with respect to broadside direction). Polarization dependent 1-D far-field beam pattern measurements along with angle-resolved Fourier transform spectroscopy of the THz radiation were performed to experimentally map the dispersion of the CRLH metamaterial antenna. The results are shown in Fig. 5.12 for a representative device similar to the one shown in Fig. 5.11(d) where coupling gap between the metamaterial antenna and THz QCL is zero. At 77 K, a relatively narrow beam (FWHM $\sim 15^\circ$) is observed at

[3]A high-purity nitrate-based Nickel etchant purchased from Transene company, Inc.

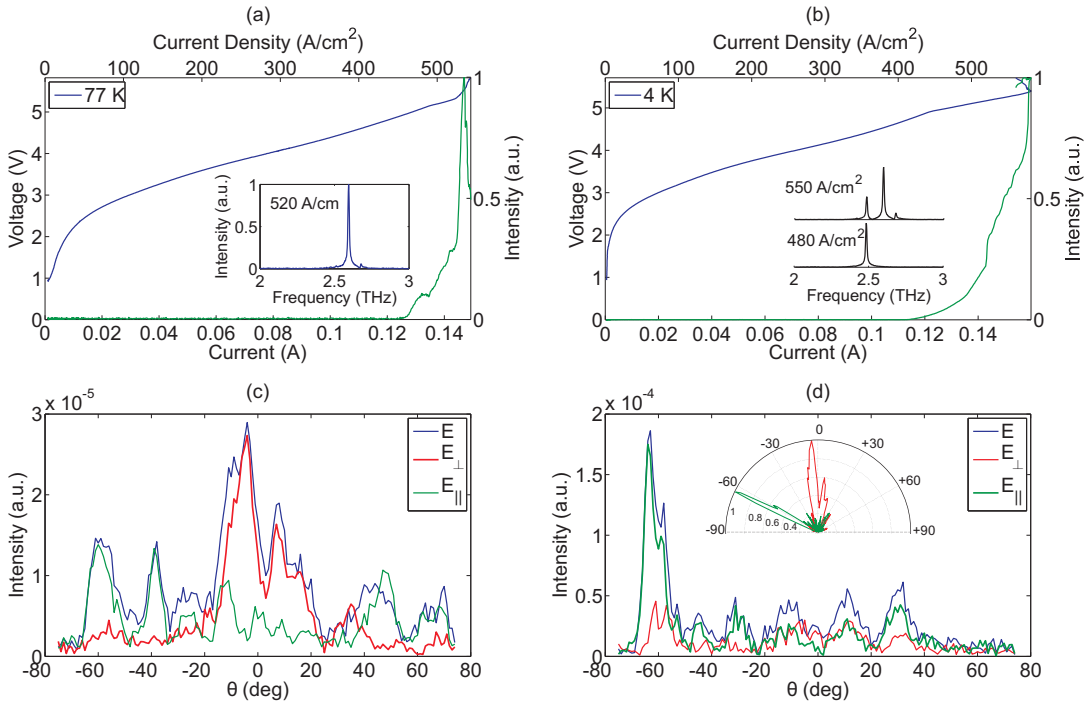

Figure 5.12: (a) 77 K and (b) 4 K face-to-face pulsed L-I-V characteristics of antenna-coupled device with the CRLH metamaterial antenna active. Insets show two representative spectra of radiation corresponding to the beam pattern measurements bias currents. All data was measured using 400 ns pulses repeated at 10 KHz.(c),(d) 1-D cuts of beam pattern in the surface direction along the longitudinal direction at 77 K and 4K, respectively. Inset is a polar representation of the two backward beams corresponding to excitation frequencies 2.484 THz (green) and 2.594 THz (red).

about $-4°$ from broadside direction. The detected THz radiation is dominantly polarized in the direction perpendicular to the antenna axis with the frequency of radiation measured to be 2.59 THz. The measured frequency and angle of the directive beam are approximately consistent with the calculated dispersion relation of Fig. 5.9(b). Compared to the gapless design, the meander-type antenna exhibits a significantly narrower beamwidth for emission close to broadside (refer to the lowest excitation frequency in Fig. 5.4). This effect is attributed to a non-zero group velocity $v_g = \mathrm{d}\omega/\mathrm{d}\beta$ at ω_0 in our balanced CRLH design, which leads to a non-diverging extinction coefficient α and much increased effective length of the antenna at or near the transition frequency.

At 4 K, the frequency of radiation Stark shifts to 2.48 THz with a single narrow beam (FWHM $\sim 10°$) observed at about $-63°$ from broadside direction. The measured frequency (angle of the directive beam) is well within the left-handed (backward wave) bandwidth of the CRLH antenna and consistent with the calculated dispersion relation of Fig. 5.9(b). The detected THz radiation — to our surprise— is dominantly polarized in the direction parallel to the antenna axis. Under ideal circumstances, one would expect the leaky-wave modes of our metamaterial waveguide to primarily radiate through the lateral fringing fields associated with the shunt capacitance C_R for which the far-field radiation is polarized transverse to the transmission-line axis. Nonetheless, the staggered nature of gap capacitors in this meander-type antenna adds another degree of freedom/complexity to the design. It is speculated that the meander-type design may radiate strongly through the longitudinal fringing fields associated with the series capacitance C_L for which the far-field radiation is polarized parallel to the transmission-line axis. Once the symmetry of the staggered design is broken, for example due to fabrication imperfections, there may be enough phase difference in between the radiating dipoles across the two gap capacitors of a unitcell (even

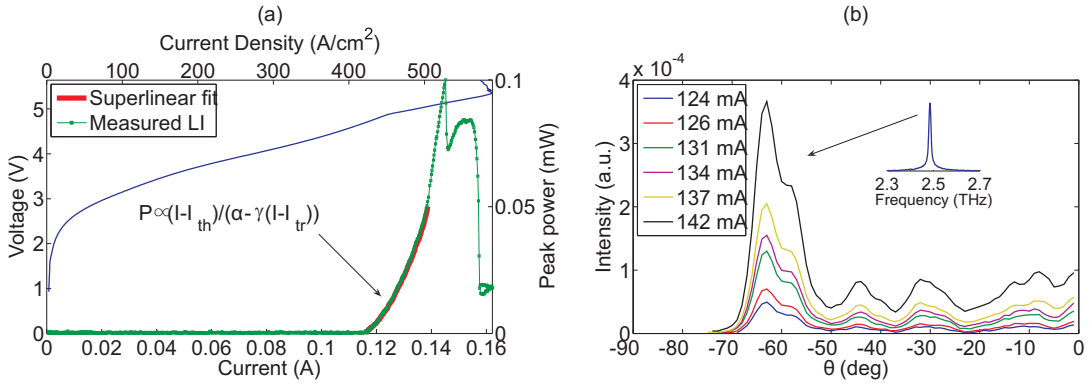

Figure 5.13: (a) Pulsed (400 ns pulses with 10 KHz PRF) L-I-V for the -60-degree beam at 4 K. Peak THz power was measured using a thermopile detector in the surface direction for the antenna structure with no collection optics in the cryostat but mounted at an angle (60 degrees) with respect to the cryostat window. A superlinear fit to the LI curve is also included with $I_{\rm th} = 116$ mA, $\alpha = 8.2$ cm^{-1}, $\gamma = 89.2$ cm^{-1}/A, and $I_{\rm tr} = 69$ mA. (b) 1-D cuts of beam pattern in the surface direction along the longitudinal direction at various bias currents. Inset shows the spectrum of radiation corresponding to -60-degree beam.

with opposite directions of E-field) that they no longer destructively interfere in the far-field, and the radiation from C_L becomes dominant over that of C_R. This is particularly important for points away from the transition frequency ω_0 on the dispersion relation where there is inherently a phase accumulation across the unitcell itself. While longitudinally polarized backward-wave radiation is feasible from Bragg surface couplers, small periodicity of the holes at the center of the waveguide ($8\ \mu$m $\sim \lambda_{\rm g}/4$) rules outs the possibility of any such scattering effects.

Since the CRLH metamaterial antenna is DC connected to the master-oscillator metal-metal QC-laser, it is synchronously biased with the same pulse trains and may provide amplification. The device exhibits a superlinear $L - I$ characteristic (see Fig. 5.13(a)) once mounted at an angle (+60 degrees) with respect to the cryostat window which indirectly implies amplification in the active antenna. Let power propagating inside antenna be $P(z) = P_0 \exp(-(\alpha - {\rm g})z)$ where $P_0 = (I - I_{\rm th})\frac{{\rm d}L}{{\rm d}I}$ is the power emitted by laser into antenna, α is the total loss

dominated by radiation, and $g = \gamma(I - I_{tr})$ is the gain coefficient beyond transparency current I_{tr}. The power radiated per unit length is $\alpha_{rad}P(z)$, so that the total radiated power is given by $P_{rad} = \frac{\alpha_{rad}}{\alpha - g}P_0$. Thus one would expect a superlinear dependence on I:

$$P_{rad} = \frac{dL}{dI}\alpha_{rad}\frac{I - I_{th}}{\alpha - \gamma(I - I_{tr})} \tag{5.1}$$

This is further evidenced in measured far-field beam patterns and angle-resolved spectra of Fig. 5.13(b) where the $-60°$-beam grows in intensity as the bias on the device is increased within the superlinear dynamic range while remaining single mode at 2.484 THz.

5.5 Conclusions

In conclusion, a one-dimensional waveguide for terahertz quantum-cascade lasers is demonstrated that acts as a leaky-wave antenna and tailors laser radiation in one dimension to a directional beam. This scheme adapts microwave transmission-line metamaterial concepts to a planar structure realized in terahertz metal-metal waveguide technology. The active leaky-wave antenna is fed by a master oscillator QC-laser with a mode that propagates with an effective phase index smaller than unity such that it radiates in the surface direction and exhibits frequency-dependent direction of radiation. We emphasize that the periodicity of the metamaterial is sufficiently small ($p = 8\ \mu m \sim \lambda_g/4$) so that the antenna is not acting as a Bragg surface coupler. This is experimentally verified by measuring polarization-dependent far-field beam patterns. As a proof of concept, we have demonstrated the beam steering capability of the leaky-wave metamaterial antenna with frequency. While the radiative losses of this initial demonstration

structure are excessive, they can be reduced by engineering the waveguide dimensions and structure —for example by reducing the height or by playing with holes in the center.

CHAPTER 6

Terahertz CRLH Transmission-Line Metamaterials

Terahertz composite right-/left-handed (CRLH) transmission-line metamaterials were eventually demonstrated in November 2011. The structure was an evolution of its precedent planar "meander" design of chapter 5, realized in GaAs/AlGaAs quantum-cascade heterostructures with terahertz metal-metal waveguide technology. Due to the addition of distributed series capacitors (realized by introducing gaps in top metallization) and shunt inductors (realized by operating in the higher-order lateral mode of the waveguide), the transmission-line exhibits left-handed (backward waves or negative index) leaky-wave propagation from $2.3 - 2.6$ THz in addition to the conventional right-handed leaky-wave behavior (from $2.6 - 3.0$ THz). This was experimentally verified via angle-resolved reflection spectroscopy measurements performed on large-area arrays of such CRLH transmission lines.

6.1 Design

The concept is illustrated in Fig. 6.1(a). It is comprised of a narrow-ridge transmission line with subwavelength transverse dimensions (3 μm tall, 14 μm wide). This height and width was chosen so as to maintain the same shunt resonance

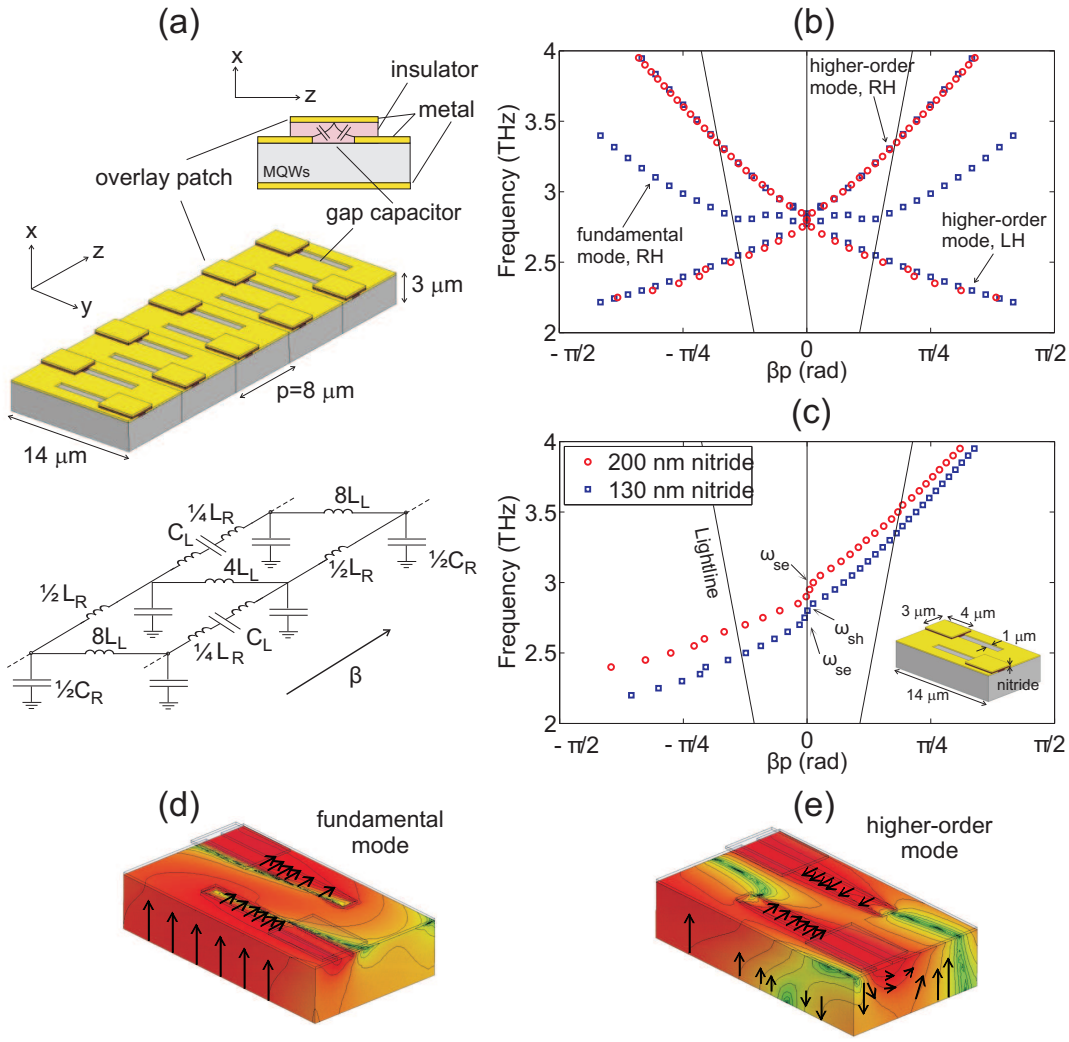

Figure 6.1: (a) Schematic representation of the CRLH transmission-line metamaterial designed to operate in a higher-order lateral mode and its equivalent transmission-line model. Distributed series capacitors are realized by introducing alternating slits in the top metallization. Overlay metallic patches provide the right amount of C_L to achieve a nearly balanced design. (b) Full band structure of an infinite CRLH line obtained by full-wave finite element simulations from a unit-cell eigenmode analysis (blue squares) showing the dispersion of the fundamental mode and the first higher-order lateral mode, and an "odd-mode" s-parameter analysis of 5 CRLH unit cells embedded in a conventional RH line (red circles). (c) Tuning of the dispersion with isolating nitride thickness (equivalently varying C_L). Inset shows one unit cell of the structure. (d), (e) field distribution for the fundamental and higher-order lateral modes, respectively.

frequency ($\omega_{\rm sh}/2\pi = \frac{1}{2\pi\sqrt{L_L C_R}} \cong 2.77$ THz) while decreasing the radiative losses ($g_{\rm th,rad} \sim 70$ cm^{-1}) compared to the planar design of Ref. [89]. The design philosophy was based on realizing the distributed shunt inductors L_L by operating in the higher-order mode of the waveguide while distributed series capacitors C_L were realized by incorporating alternating slits in the top metallization. Overlay metallic patches electrically isolated from the top metallization by a thin (~ 140 nm) silicon nitride —similar to the ones discussed in section 3.3— were employed to provide the right amount of C_L required for a nearly balanced design ($\omega_{\rm se}/2\pi = \frac{1}{2\pi\sqrt{L_R C_L}} \cong 2.75$ THz). By employing alternating gap capacitors a meandered structure is obtained which exhibits an effectively larger right-handed inductance L_R and helps achieving a balanced design with not-so-aggressive gap dimensions (1 μm). Moreover, due to its continuous DC connectivity, the structure can be used as an active terahertz QCL waveguide as well as a purely passive metamaterial leaky-wave antenna.

Dispersion behavior of an infinitely long CRLH transmission-line metamaterial of this design is shown in Fig. 6.1(b). The transition frequency occurs at $\omega_0/2\pi = \frac{1}{2\pi}\sqrt{\omega_{\rm sh}\omega_{\rm se}} = 2.76$ THz with the light cone ($-1 < n_{\rm eff} < 1$) extending from $2.5-3.3$ THz. The full band structure was obtained from finite element simulations of a single unit-cell using periodic boundary conditions which shows the dispersion of the fundamental and higher-order lateral modes of the waveguide. The structure supports left-handed (negative index) propagation only for the higher-order mode since there are no conduction currents in the transverse direction for the fundamental mode. Nonetheless, leaky-wave behavior ($0 < n_{\rm eff} < 1$, right-handed (RH) portion only) is still observed for the fundamental mode due to the existence of series capacitors. Owing to the asymmetric nature of the meander design, the eigenmodes of the waveguide are indeed superposition modes with "odd-like" or "even-like" characteristics (see Fig. 6.1(d),(e)). This makes modal

identification confusing sometimes. For that reason, the dispersion characteristic of the structure was alternatively obtained from an "odd-mode" s-parameter analysis of 5 CRLH unit cells embedded in a conventional RH line. Good agreement between the unit-cell eigenmode analysis and five-cell s-parameter analysis is observed. Nonetheless, both simulations rendered computationally time- and memory-intensive mainly due to the large number of finite elements required for proper meshing of the patch capacitors.

Tuning of the dispersion relation is possible via varying the series capacitors C_L (equivalently moving ω_{se} up or down in frequency). This could be achieved by either varying the overlay patch dimensions or isolating nitride thickness, or both. Dispersion tuning with the nitride thickness is shown in Fig. 6.1(c). In the language of transmission-line metamaterials, thinning the isolating nitride layer from $200 - 130$ nm leads to a larger series capacitor C_L, and reduces the series resonance frequency from 3.0 THz down to 2.65 THz. For a given waveguide width and gap dimensions, C_R and L_L are fixed however, and ω_{sh} does not change.

6.2 Fabrication

The fabricated prototype consists of large-area arrays of CRLH transmission-lines suitable for performing reflection spectroscopy measurements on a metamaterial surface. The structure was fabricated in metal-metal waveguide technology (Cu-Cu) using the 5-μm-thick GaAs/$Al_{0.15}Ga_{0.85}As$ multiple-quantum-well heterostructure (growth NG-B17952). For some wafer pieces the epilayer was thinned to 3 μm using dilute peroxide ammonia (PA) etch (NH_4OH:H_2O_2:H_2O::5:3:490) which left the wafers with rough surfaces. The process was not continued for those pieces and the results shown here are only for 5-μm-tall structures. The metallization for the top contact (Ti/Au::20/100 nm) was defined by electron-beam

lithography using a bilayer of polymethyl methacrylate (PMMA) e-beam grade positive resists (495-A4 and 950-A2) and lift-off process (see Fig. 6.2(a)). Any highly-doped n^+-GaAs layer present in the growth sequence should be removed at or before this stage to avoid shorting the gap capacitors. For that reason, a PA etch (NH_4OH:H_2O_2:H_2O::10:6:480 for 2 minutes) was performed prior to the e-beam lithography. A thin (1400 Å) PECVD nitride was deposited next and the metallization for the overlay patches (Ti/Au::15/85 nm) was defined by e-beam lithography using the same bilayer of PMMA resists (Fig. 6.2(b)). Lastly, a dry etch mask to define the ridges was deposited by performing a third round of e-beam lithography/metal evaporation (Ni::200 nm). Prior to mesa definition the insulating nitride was removed in an STS advanced oxide etcher using the same Ni mask.

Figure 6.3 shows an SEM image of the fabricated metamaterial surface. CRLH transmission-line arrays are uniformly formed over an area of 0.5 cm $\times$ 0.5 cm —a challenge that has successfully been overcome in this demonstration. Due to the requirements set by the e-beam writing alignment, however, wafer pieces of 1.3 cm $\times$ 1.3 cm were processed, accommodating four metamaterial arrays of variuos feature sizes. The array period in the transverse direction is 100 μm. This periodicity in the y-direction was chosen as a compromise between e-beam write time, i.e. cost, and appearance of grating lobes within the frequency range of interest, and provides enough spacing between neighboring waveguides to avoid mode coupling. A cross-section of the the overlay capacitor along the longitudinal direction obtained by focused ion beam (FIB) milling is also shown in Fig. 6.3.

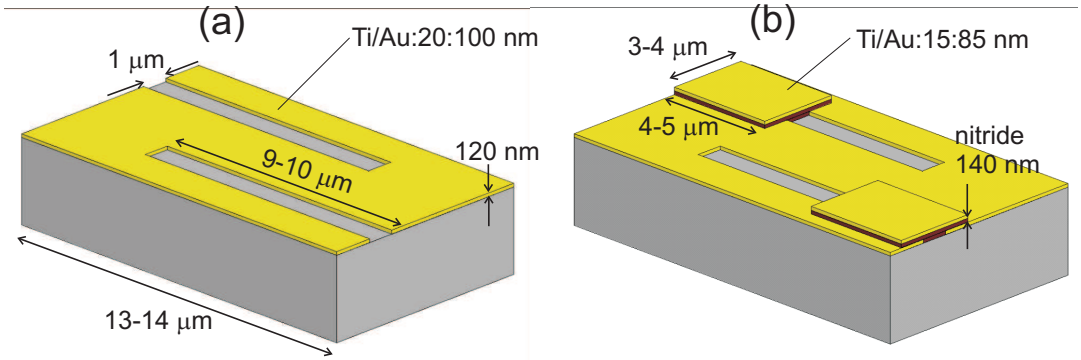

Figure 6.2: Schematic drawings showing the metallization layers involved in the fabrication of the CRLH transmission-line metamaterial. (a) Meander top metal contact with alternating slits, and (b) overlay patch capacitors laying on the insulating nitride layer.

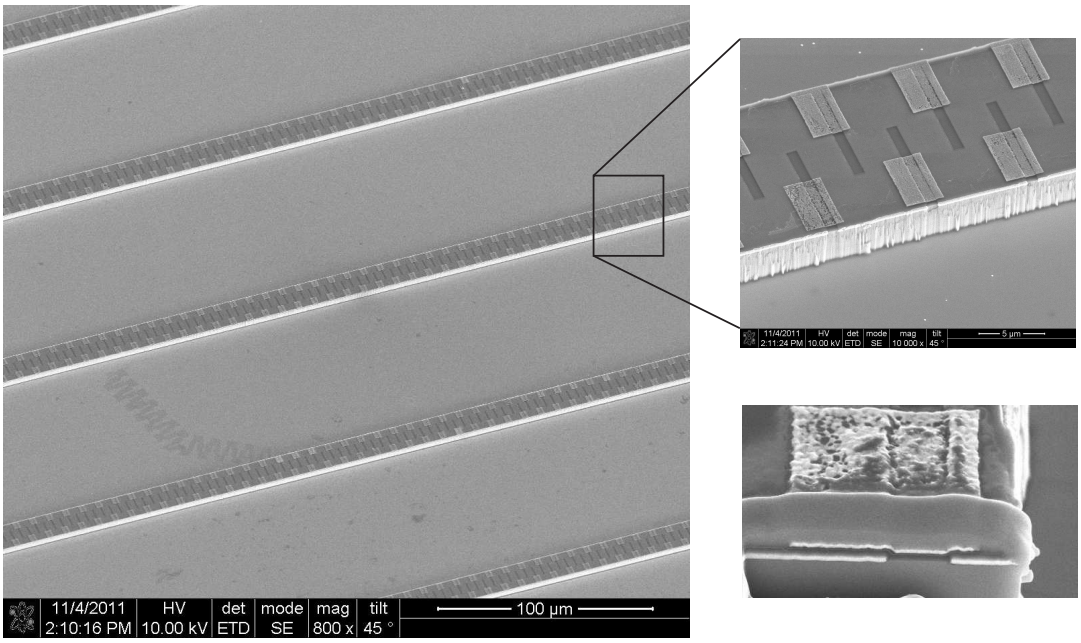

Figure 6.3: SEM image of the fabricated CRLH metamaterial waveguide array. A cross-section of the the overlay capacitor along the longitudinal direction is shown in the lower right. The layer above the overlay Au patch is platinum introduced during FIB milling, and is not present in the actual structure.

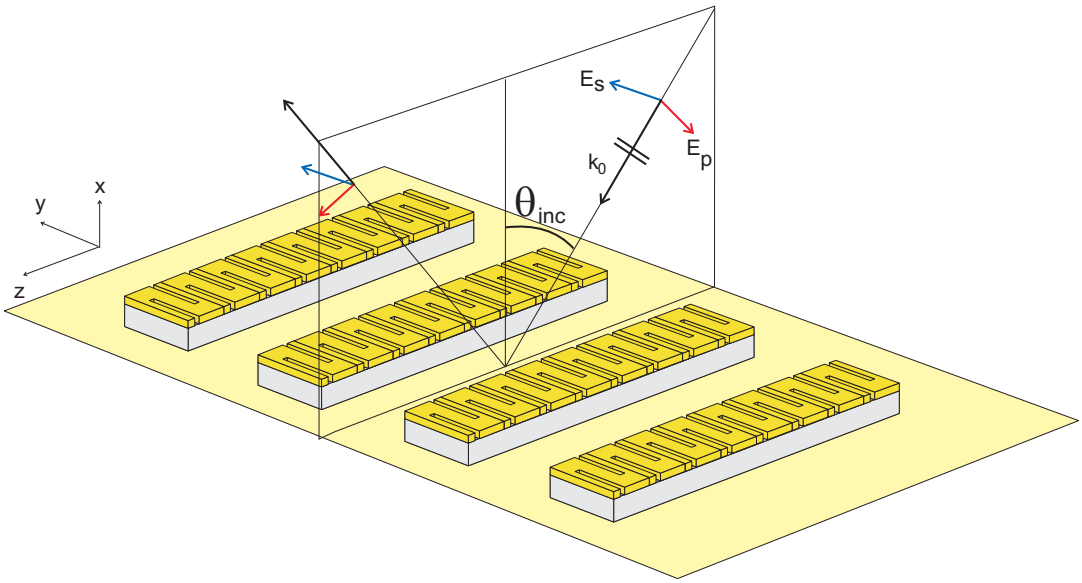

Figure 6.4: Reflection spectroscopy setup.

6.3 Experiments

The dispersion relations of the CRLH transmission-line metamaterials were mapped experimentally with angle-resolved Fourier transform infrared (FTIR) reflection spectroscopy. The experimental setup for this approach was originally performed by Zhijun Liu in our group. He established the process on larger (1 cm $\times$ 1 cm) CRLH metamaterial waveguide arrays of similar design fabricated with spin-coated Benzocyclobutene (BCB) in lieu of the QC gain material and contact photolithography [145]. The sample and detector were mounted on a $\theta - 2\theta$ rotary stage, which allows for a continuous incident angle scan from $10 - 90°$. The FTIR broadband light was focused on the sample with an 8 in focal length off-axis paraboloid mirror with a spot size ($D \sim 0.7$ cm) slightly larger than the sample size. This resulted in a smaller signal-to-noise ratio compared to the previous experiments performed on the BCB-CRLH waveguides due to beam walk-off, especially at larger incident angles. The plane of incidence was kept perpendic-

ular to the sample surface and parallel to the transmission-line axis as shown in Fig. 6.4. All measurements were performed at room temperature. The system was purged with N_2 gas. The reflection from a gold mirror mounted back-to-back to the sample was used as the reference spectrum which allowed for not breaking the purge for the entire experiment duration.

We focus on the leaky-wave bandwidth of the CRLH transmission-line metamaterial where coupling of the waveguide propagating modes to the free-space radiating modes are most efficient. Within the light cone the propagation constant β of the guided modes is smaller than the wave-vector amplitude k_0 of the incident light. Therefore, for a given incident angle θ_{inc}, the in-plane wave-vector of the incident light matches that of the guided propagating mode at a specific frequency $k_0 \sin(\theta_{\text{inc}}) = \beta(\omega)$, and the incident light is coupled into the waveguide array resulting in absorption dip(s) in the reflection spectrum due to metallic and dielectric losses. Experiments were performed for both *s*-polarized (electric field polarized transverse to the transmission-line axis) and *p*-polarized (electric field polarized along the longitudinal direction) incident light corresponding to the far-field radiation polarization of the metamaterial waveguide operation in higher-order and fundamental modes, respectively [146].

Coupling of the *s*-polarized light with the leaky-wave modes of our metamaterial waveguide is primarily through the lateral fringing fields associated with the shunt capacitance C_R for which the far-field radiation is polarized transverse to the transmission-line axis. For the *s*-polarized incident light, we expect two absorption dips in the reflection spectrum corresponding to both right-handed and left-handed (backward wave) propagating higher-order waveguide modes. Figure 6.5(a) shows the reflection spectra of the CRLH transmission-line metamaterial at different incident angles for incident *s*-polarized light. Two absorp-

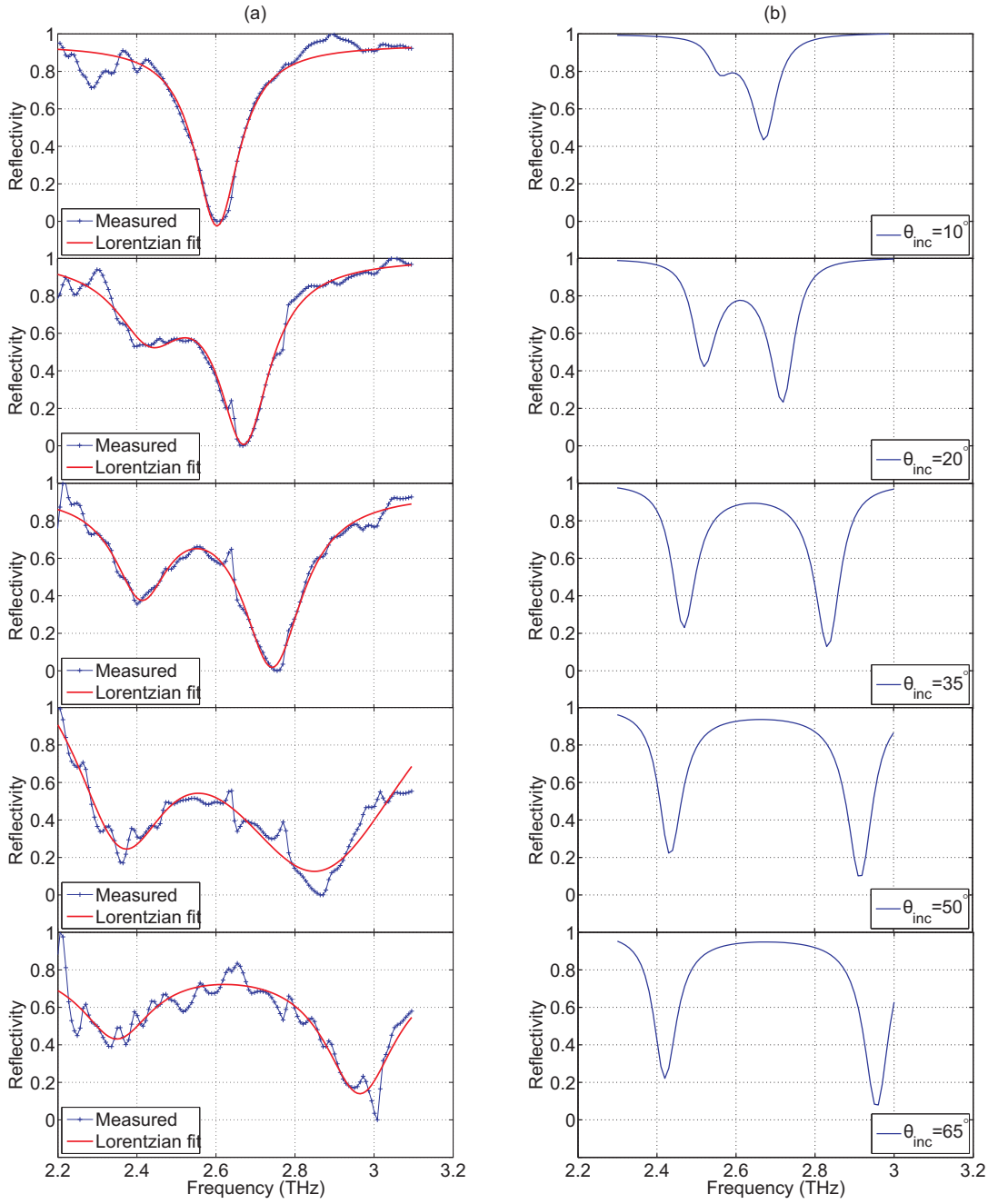

Figure 6.5: Reflection spectra of the CRLH transmission-line metamaterial for incident s-polarized light. (a) Measured spectra (+) showing two absorption dips corresponding to RH and LH propagating modes and Lorentzian fits (solid lines) to the data, and (b) simulated reflection spectra of the same structure obtained by full-wave finite element simulations from a unit-cell s-parameter analysis using Floquet's boundary conditions. The thickness of the QC material was assumed 5 μm. Ohmic losses due to finite conductivity of the Au metallization was incorporated using a Drude conductivity with $n = 5.9 \times 10^{22}\text{cm}^{-3}$, $\tau = 60$ fs, $m^* = m_0$, $\epsilon_{\text{core}} = 1$ for the Drude parameters.

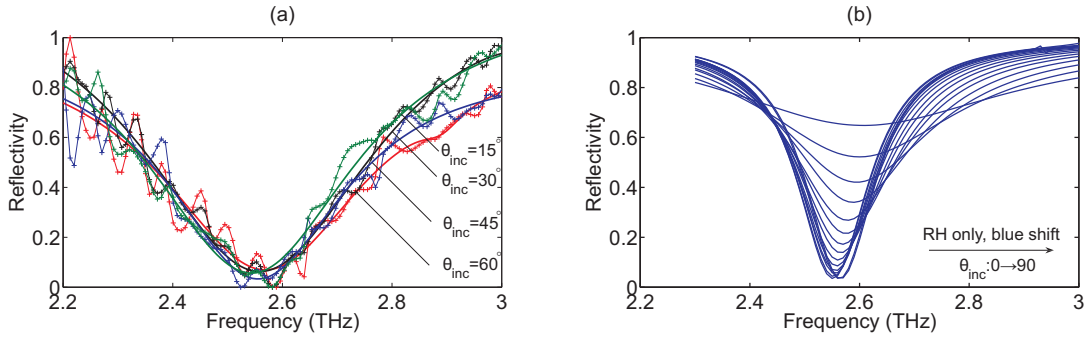

Figure 6.6: Reflection spectra of the CRLH transmission-line metamaterial for incident p-polarized light. (a) Measured spectra (+) showing a single absorption dip corresponding to RH propagating modes and a Lorentzian fit (solid lines) to the data, and (b) simulated reflection spectra of the same structure obtained by full-wave finite element simulations from a unit-cell s-parameter analysis using Floquet's boundary conditions.

tion dips are observed in the spectrum, each with a Lorentzian lineshape. As the incident angle is increased from 10° to 75°, the higher frequency absorption dip blue-shifts from 2.6 to 3.0 THz, corresponding to right-handed propagating modes. The absorption dip at lower frequency red-shifts from 2.45 to 2.3 THz, however, which corresponds to left-handed propagating modes with anti-parallel group and phase velocities. The observation of the CRLH dispersion behavior for incident s-polarization is consistent with the predicted reflectivity obtained from full-wave finite element simulations (Fig. 6.5(b)) which clearly shows the right-handed and left-handed characteristics of such a CRLH transmission line.

Similar experiments were performed on the CRLH transmission-line metamaterial with the polarization of the incident light parallel to the waveguide axis (p-polarization). Since the incident p-polarized light couples to the series capacitors C_L and does not excite any transverse currents (equivalently does not exhibit an effective shunt inductance L_L), only right-handed propagation is expected. For the p-polarized light, we only expect one absorption dip associated with right-handed dispersion of the propagating fundamental waveguide modes.

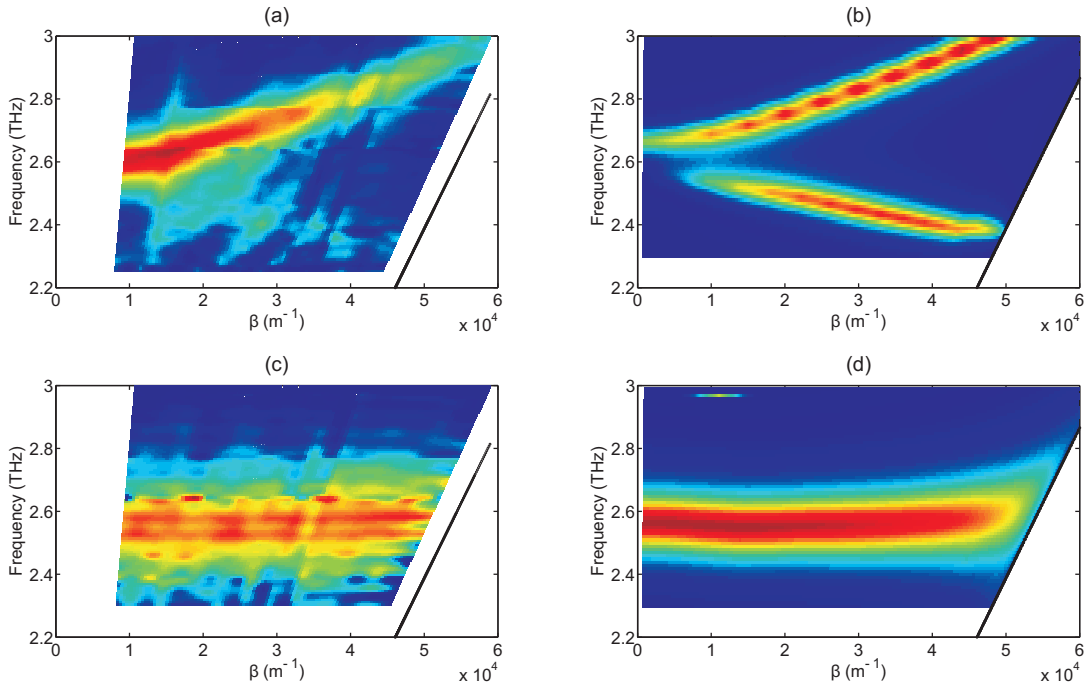

Figure 6.7: Contour plots of the absorption for the *s*-polarized incident light. (a) Measured, and (b) simulated.(c),(d) Measured and simulated contour plots of the absorption for the *p*-polarized incident light.

Figure 6.6(a) shows the corresponding measured reflection spectra where there is only one absorption dip which blue-shifts with increasing incident angle. This is the characteristic of our transmission-line metamaterial when operating in the fundamental mode as was verified via finite element simulations (Fig. 6.6(b)). The cut-off frequency of this mode is dictated by the series resonance frequency, extrapolated to be at $\omega_{se}/2\pi \cong 2.59$ THz.

Lastly, the dispersion relations of the CRLH transmission-line metamaterial were extracted from the raw measured absorption spectra (Fig. 6.7) using a least-squares fit to a (or two) Lorentzian lineshape function(s). The results are plotted in Fig. 6.8 for *s*- and *p*-polarized incident light. Both right-handed and left-handed branches exist for the the *s*-polarized light which clearly confirms the demonstration of CRLH behavior for our terahertz metamaterial.

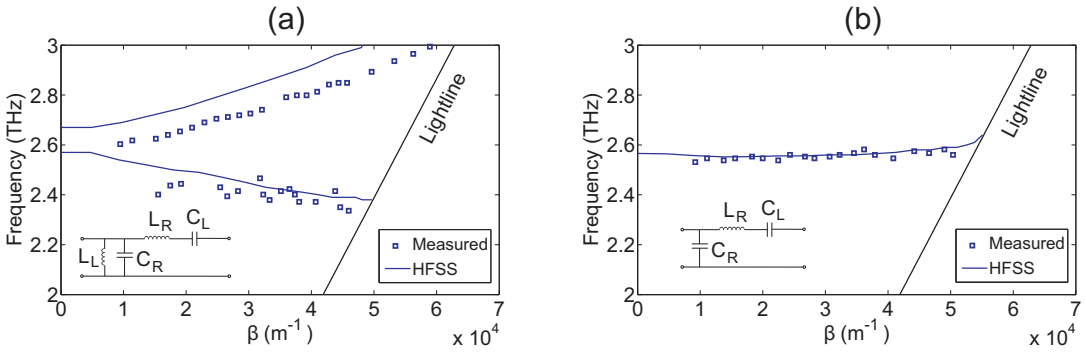

Figure 6.8: Dispersion diagrams of the CRLH transmission-line metamaterial extracted from measured absorption spectra using a least-squares fit to (a) two Lorentzian lineshape functions for the *s*-polarized incident light, and (b) one Lorentzian lineshape function for the *p*-polarized incident light.

6.4 Conclusions and Discussion

In this thesis, I have described the development of a terahertz composite right-/left-handed transmission-line metamaterial realizable in active quantum-cascade structures with terahertz metal-metal waveguide technology. The research conducted in this study primarily involved device theory and design, extensive electromagnetic modeling, micro- and nano-fabrication, and experimental characterization and testing. The QC-CRLH transmission-line metamaterial demonstration was a convergence of a wide variety of designs/ideas that were modeled, simulated, and tested in order to obtain operational structures. Over the course of this thesis many design tools were developed that contributed to our understanding of these devices. Of particular importance was the development of a general-purpose platform for calculations of threshold intersubband gain in metal-metal waveguide structures. Along with three-dimensional full-wave finite element simulations, transmission-line circuit models as well as cavity antenna models were employed that allowed rapid and intuitive modification of design strategies. Several fabrication procedures were established two of the most sig-

nificant being the fabrication of metal-metal waveguides using robust copper-to-copper thermocompression wafer bonding with dry-etched laser structures, and fabrication of terahertz transmission-line metamaterials using e-beam lithography and multilayer metal deposition techniques. Lastly, many terahertz metamaterial structures were tested using pulsed and continuous-wave transport, polarization-dependent far-field radiation pattern measurements, and polarization-dependent angle-resolved Fourier transform emission/reflection spectroscopy techniques performed at cryogenic temperatures.

Some of the major accomplishments and experimental observations that were achieved throughout the course of this research includes:

- Demonstration of thin-core (5-μm-thick) terahertz quantum-cascade lasers at $2.4 - 2.9$ THz ($\lambda \approx 100 - 125$ μm) based on resonant-phonon active regions and metal-metal waveguides which served as the foundation for development of active terahertz QC-CRLH transmission-line metamaterials. The resonant-phonon QC designs operate based on resonant tunneling of the lower radiative state combined with direct LO-phonon scattering for rapid and selective depopulation which provides an efficient and temperature insensitive depopulation mechanism. Low-loss metal-metal waveguides have been used for mode confinement. Such a waveguide has a confinement factor close to unity which allows realization of laser microcavities with deep subwavelength dimensions.

- Observation of narrow (FWHM $\sim 15^\circ$ along one direction) single beam surface radiation ($\sim 40^\circ$ from broadside) from a one-dimensional terahertz leaky-wave transmission line used as a coupler antenna for a THz quantum-cascade laser. This scheme adapted microwave transmission-line metamaterial concepts to a planar structure realized in terahertz metal-

metal waveguide technology. The leaky-wave antenna operation is based on a propagating mode with an effective phase index smaller than unity such that it radiates in the surface direction into a single directive beam with slope efficiencies $\sim$ 4 times greater than conventional Fabry-Pérot metal-metal waveguides. Such a characteristic —extensively discussed in section 3.3— is a boon for THz QC-lasers, which suffer from highly divergent beam patterns and poor power out-coupling efficiencies.

- Observation of frequency-dependent direction of radiation main beam for leaky-wave metamaterial antennas and experimental demonstration of 50 degrees (from $10 - 60°$) of forward beam steering with frequency. Beam scanning from $35° - 60°$ was observed from a single device as the lasing frequency of the QC-laser varied from $2.65 - 2.81$ THz. By changing the bias on the metal-metal QC-laser, the laser was forced to hop between different axial modes, which allowed us to excite the antenna at several discrete frequencies. Beamwidth broadening was also experimentally observed for emission close to broadside which indicated reduction of group velocity and effective antenna aperture for excitation frequencies close to ω_{sh}.

- Demonstration of power amplification in far-field radiation intensity of a terahertz master oscillator power amplifier (MOPA) realized by employing a THz QC-laser as a master oscillator feeding a leaky-wave metamaterial antenna and active biasing of the antenna section. Narrow beam emission (at $\sim$ 2.74 THz) was observed, which grew in intensity as the bias on the antenna was increased.

- Experimental observation of both right-handed and left-handed branches of CRLH dispersion for a meander-type terahertz QC-CRLH transmission-line metamaterial by performing polarization-dependent angle-resolved re-

flection spectroscopy measurements on large-area transmission-line arrays. Two absorption dips with Lorentzian lineshapes were observed in the spectrum. The high-frequency absorption dip exhibited blue-shift (from 2.6−3.0 THz) by increasing the incident angle of s-polarized light (from $10 - 75^{\circ}$) corresponding to right-handed propagating modes. The low-frequency absorption dip exhibited red-shift (from $2.45 - 2.3$ THz) by increasing the incident angle of light corresponding to left-handed propagating modes.

A lot of what has been done in this thesis could be considered first steps for opening up new approaches to THz devices. A relevant question to ask would be what the full promise for THz transmission-line metamaterials is and can they, for instance, compete with third-order DFBs? The answer partially relies on how good of an optimization can be performed in future demonstrations. For example, the leaky-wave antenna of [89, 147] was designed to couple to the master-oscillator THz QCL via a 3-μm gap. The coupling efficiency of such a design is calculated to be only $\sim 12\%$ at 2.7 THz (varying from $3 - 35\%$ over the bandwidth $2.6 - 3.0$ THz, obtained from full-wave finite element simulations). Obviously, higher output power (up to an order of magnitude) can be achieved from an optimized transition —a continuous transition for instance— with slope efficiency exceeding that of a third-order DFB. Further benefits will result from reducing the height of QC gain material, e.g. to 3 μm, to alleviate the excessive radiative losses of this initial demonstration. Moreover, phase-locked arrays of these leaky-wave antennas can be employed to reduce beam divergence in the transverse direction and improve the radiation coupling and collection efficiency.

One can readily envision extending the planar CRLH transmission-line arrays to large aperture emitters (see Fig. 6.9). By employing such CRLH transmission-lines as coupler antenna arrays for a master oscillator THz QC-laser, one obtains

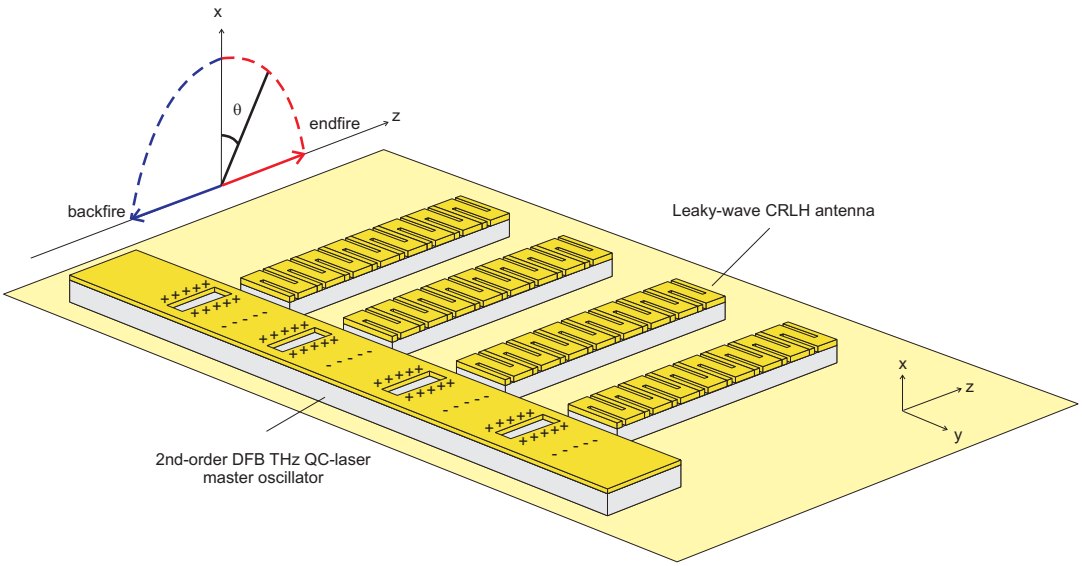

Figure 6.9: Schematic drawing showing a large aperture emitter consisting of a 2nd-order DFB master-oscillator THz QC-laser feeding an array of CRLH transmission-line metamaterial leaky-wave antennas.

a large aperture emitter with narrow (in both axial and transverse directions) steerable beam and full backfire to endfire beam scanning capability. At this time, however, additional challenges exist for demonstration of backward waves (left-handed or negative index propagation) in an active CRLH transmission-line metamaterial of this design. This is in part due to increased metal losses and reduced group velocity in the LH range as well as challenges involved in microfabrication of active devices due to additional lithography/etch steps. One solution may be to avoid additional metallization steps by resorting to the original "nano-gap" capacitors to achieve the right amount of series capacitance C_L. This would require more demanding e-beam lithography as gaps with order of magnitude smaller dimensions ($\leq$ 200 nm) are needed (section 5.4).

Nonetheless, apart from novel functionalities demonstrated and/or discussed in this thesis, CRLH metamaterial waveguides can offer terahertz QC-lasers several other advantages. The most significant of which, in my opinion, is the single-

mode dynamic frequency tuning of a THz QC-laser. By dynamically varying the value of lumped elements of the CRLH transmission line (series capacitors for instance) one can modify the dispersion of the line and consequently the spectral properties of a cavity made in part or whole from such a transmission-line metamaterial. This is particularly promising as the characteristic resonant frequencies of a THz QCL can be tuned over a wide spectral range (e.g. 100s of GHz). One of the largest needs for terahertz technology at present is a compact, widely-tunable terahertz source, that operates in continuous-wave mode with high output power. Traditionally, external cavity tuning has been the most common approach of achieving wideband mode-hop-free tunability, which involves an inherently slow mechanical tuning mechanism [148–150]. The tunable metamaterial cavity represents a way to electrically tune the resonance frequencies of the laser without any moving parts, which is inherently faster, more stable and less challenging at cryogenic temperatures [151].

Another appealing future research direction is the use of zero-index or negative-index CRLH metamaterials for demonstration of ultra small THz lasers and light-emitting devices operating in the strong-coupling regime between light and matter. Unlike conventional lasers which operate in the weak-coupling regime, coherent energy exchange between cavity photons and intersubband electronic states can take place in deep subwavelength micro-cavities, leading to intersubband polaritons [152–155]. The use of a quantum cascade structure to achieve photon emission from intersubband cavity polariton states holds a great promise to realize mid-infrared/THz lasers operating without population inversion [156].

Appendix A

Processing recipes

A.1 AZ nLOF 2035 photostep

(1) Wafer prebake at 150 °C for 3 minutes on hotplate, then cool to ambient.

(2) Soak in HMDS vapor for 15 minutes.

(3) Deposit AZ nLOF 2035. Spin at 4000 rpm for 30 seconds.

(4) Wafer softbake at 110 °C for 60 seconds on hotplate.

(5) Clean backside of the wafer with a swab.

(6) Karl-Suss exposure for 12 seconds (8 mW/cm^2, 365 nm).

(7) Wafer postbake at 110 °C for 60 seconds on hotplate.

(8) Develop in AZ 300 MIF for 75 seconds. DI water rinsing. Blow dry with N_2.

A.2 GaAs dry etching recipe

Dry etching was performed in the Unaxis SLR770 ICP-RIE using the ATGAAS.RCP recipe, listed below. Etch rate is 0.5 μm/minute.

BCl_3 flow rate 50 sccm.

Pressure 10 mTorr.

RF1 (RIE) power 100 W.

RF2 (ICP) power 800 W.

Temperature 21 °C.

A.3 High-deposition rate SiO_2 PECVD recipe

PECVD SiO_2 deposition was performed in the STS using the HIDROXID.RCP recipe, listed below. Calibration runs on blank Si wafer(s) before performing the deposition is essential, since the deposition rate varies from run to run and/or may not be linear in the first few minutes. Deposition rate is ~ 3000 $\mathring{A}$/minute.

N_2O flow rate 2000 sccm.

SiH_4 flow rate 50 sccm.

Pressure 400 mTorr.

LF power 140 W.

Temperature 300 °C.

A.4 Ammonium-free Si_3N_4 PECVD recipe

PECVD Si_3N_4 deposition was performed in the STS using the NH3FREE.RCP recipe, listed below. Deposition rate is ~ 230 $\mathring{A}$/minute.

N_2O flow rate 2294 sccm.

SiH_4 flow rate 12 sccm.

Pressure 550 mTorr.

LF power 40 W.

Temperature 300 °C.

A.5 SiO_2/Si_3N_4 dry etching recipe

SiO_2/Si_3N_4 dry etching was performed in the STS AOE (Advanced Oxide Etcher) using the SIN4000.RCP recipe, listed below. Running etch cleans and conditioning the chamber before performing the etch is essential. Etch rate is

4000 $\mathring{A}$/minute.

CF_4 flow rate 20 sccm.

C_4F_8 flow rate 20 sccm.

O_2 flow rate 4 sccm.

Pressure 4 mTorr.

RF1 (RIE) power 200 W.

RF2 (ICP) power 1250 W.

References

[1] P. Siegel, "Terahertz technology," *IEEE Transactions on Microwave Theory and Techniques*, vol. 50, no. 3, pp. 910–928, 2002.

[2] B. Ferguson and X.-C. Zhang, "Materials for terahertz science and technology," *Nature Materials*, vol. 1, no. 1, pp. 26–33, 2002.

[3] D. Woolard, R. Brown, M. Pepper, and M. Kemp, "Terahertz frequency sensing and imaging: A time of reckoning future applications?," *Proceedings of the IEEE*, vol. 93, no. 10, pp. 1722–1743, 2005.

[4] M. Tonouchi, "Cutting-edge terahertz technology," *Nature Photonics*, vol. 1, no. 2, pp. 97–105, 2007.

[5] P. L. Richards, "Bolometers for infrared and millimeter waves," *Journal of Applied Physics*, vol. 76, no. 1, pp. 1–24, 1994.

[6] E. Haller, "Advanced far-infrared detectors," *Infrared Physics and Technology*, vol. 35, no. 23, pp. 127 – 146, 1994.

[7] K. A. McIntosh, E. R. Brown, K. B. Nichols, O. B. McMahon, W. F. DiNatale, and T. M. Lyszczarz, "Terahertz photomixing with diode lasers in low-temperature-grown GaAs," *Applied Physics Letters*, vol. 67, no. 26, pp. 3844–3846, 1995.

[8] S. Matsuura, M. Tani, and K. Sakai, "Generation of coherent terahertz radiation by photomixing in dipole photoconductive antennas," *Applied Physics Letters*, vol. 70, no. 5, pp. 559–561, 1997.

[9] S. Verghese, K. A. McIntosh, S. Calawa, W. F. Dinatale, E. K. Duerr, and K. A. Molvar, "Generation and detection of coherent terahertz waves using two photomixers," *Applied Physics Letters*, vol. 73, no. 26, pp. 3824–3826, 1998.

[10] A. Raisanen, "Frequency multipliers for millimeter and submillimeter wavelengths," *Proceedings of the IEEE*, vol. 80, no. 11, pp. 1842–1852, 1992.

[11] F. Maiwald, F. Lewen, B. Vowinkel, W. Jabs, D. Paveljev, M. Winnewisser, and G. Winnewisser, "Planar schottky diode frequency multiplier for molecular spectroscopy up to 1.3 THz," *IEEE Microwave and Guided Wave Letters*, vol. 9, no. 5, pp. 198–200, 1999.

[12] G. Chattopadhyay, E. Schlecht, J. Ward, J. Gill, H. Javadi, F. Maiwald, and I. Mehdi, "An all-solid-state broad-band frequency multiplier chain at 1500 GHz," *IEEE Transactions on Microwave Theory and Techniques*, vol. 52, no. 5, pp. 1538–1547, 2004.

[13] E. R. Brown, K. A. McIntosh, K. B. Nichols, and C. L. Dennis, "Photomixing up to 3.8 THz in low-temperature-grown GaAs," *Applied Physics Letters*, vol. 66, no. 3, pp. 285–287, 1995.

[14] E. Rouvalis, C. C. Renaud, D. G. Moodie, M. J. Robertson, and A. J. Seeds, "Traveling-wave Uni-Traveling Carrier Photodiodes for continuous wave THz generation," *Opt. Express*, vol. 18, no. 11, pp. 11105–11110, 2010.

[15] A. Maestrini, I. Mehdi, J. Ward, R. Lin, B. Thomas, C. Lee, J. Gill, G. Chattopadhyay, E. Schlecht, and P. H. Siegel, "A 2.5-2.7 THz room temperature electronic source," in *22nd International Symposium on Space Terahertz Technology*, 2011.

[16] T. W. Crowe, J. L. Hesler, C. Pouzou, W. L. Bishop, and G. S. Schoenthal, "Development and characterization of a 2.7 THz LO source," in *22nd International Symposium on Space Terahertz Technology*, 2011.

[17] J. Ward, F. Maiwald, G. Chattopadhyay, E. Schlecht, A. Maestrini, J. Gill, and I. Mehdi, "1400-1900 GHz local oscillators for the Herschel Space Observatory," in *14th International Symposium on Space TeraHertz Technology*, 2003.

[18] G. Chattopadhyay, "Technology, capabilities, and performance of low power terahertz sources," *IEEE Transactions on Terahertz Science and Technology*, vol. 1, no. 1, pp. 33–53, 2011.

[19] http://www.esa.int/SPECIALS/Herschel/index.html.

[20] L. Samoska, "An overview of solid-state integrated circuit amplifiers in the submillimeter-wave and THz regime," *IEEE Transactions on Terahertz Science and Technology*, vol. 1, no. 1, pp. 9–24, 2011.

[21] R. Lai, X. Mei, W. Deal, W. Yoshida, Y. Kim, P. Liu, J. Lee, J. Uyeda, V. Radisic, M. Lange, T. Gaier, L. Samoska, and A. Fung, "Sub 50 nm InP HEMT device with Fmax greater than 1 THz," in *IEEE International Electron Devices Meeting*, pp. 609–611, 2007.

[22] R. Lai, X. Mei, S. Sarkozy, W. Yoshida, P. Liu, J. Lee, M. Lange, V. Radisic, K. Leong, and W. Deal, "Sub 50 nm InP HEMT with f_T =586 GHz and

amplifier circuit gain at 390 GHz for sub-millimeter wave applications," in *International Conference on Indium Phosphide Related Materials*, pp. 1–3, 2010.

[23] V. Jain, J. Rode, H.-W. Chiang, A. Baraskar, E. Lobisser, B. Thibeault, M. Rodwell, M. Urteaga, D. Loubychev, A. Snyder, Y. Wu, J. Fastenau, and W. Liu, "1.0 THz fmax InP DHBTs in a refractory emitter and self-aligned base process for reduced base access resistance," in *69th Annual Device Research Conference*, pp. 271–272, 2011.

[24] K. Shinohara, A. Corrion, D. Regan, I. Milosavljevic, D. Brown, S. Burnham, P. Willadsen, C. Butler, A. Schmitz, D. Wheeler, A. Fung, and M. Micovic, "220GHz fT and 400GHz fmax in 40-nm GaN DH-HEMTs with regrown ohmic," in *IEEE International Electron Devices Meeting*, pp. 30.1.1 –30.1.4, 2010.

[25] H. Eisele, "InP Gunn devices for 400-425 GHz," *Electronics Letters*, vol. 42, no. 6, pp. 358–359, 2006.

[26] H. Eisele, "Third-harmonic power extraction from InP Gunn devices up to 455 GHz," *IEEE Microwave and Wireless Components Letters*, vol. 19, no. 6, pp. 416–418, 2009.

[27] S. Suzuki, M. Asada, A. Teranishi, H. Sugiyama, and H. Yokoyama, "Fundamental oscillation of resonant tunneling diodes above 1 THz at room temperature," *Applied Physics Letters*, vol. 97, no. 24, p. 242102, 2010.

[28] J. Hesse and H. Preier, "Lead salt laser diodes," in *Festkrperprobleme 15* (H. Queisser, ed.), vol. 15 of *Advances in Solid State Physics*, pp. 229–251, Springer Berlin / Heidelberg, 1975.

[29] H. Hubers, S. Pavlov, and V. Shastin, "Terahertz lasers based on germanium and silicon," *Semiconductor Science and Technology*, vol. 20, no. 7, pp. S211–S221, 2005.

[30] L.-H. Xu, R. Lees, E. Vasconcellos, S. Zerbetto, L. Zink, and K. Evenson, "Methanol and the optically pumped far-infrared laser," *IEEE Journal of Quantum Electronics*, vol. 32, no. 3, pp. 392 –399, 1996.

[31] G. P. Williams, "FAR-IR/THz radiation from the Jefferson Laboratory, energy recovered linac, free electron laser," *Review of Scientific Instruments*, vol. 73, no. 3, pp. 1461–1463, 2002.

[32] J. Faist, F. Capasso, D. L. Sivco, C. Sirtori, A. L. Hutchinson, and A. Y. Cho., "Quantum cascade laser," *Science*, vol. 264, no. 5158, pp. 553–556, 1994.

[33] R. Kohler, A. Tredicucci, F. Beltram, H. E. Beere, E. Harvey, E. H. Linfield, A. G. Davies, D. A. Ritchie, R. C. Iotti, and F. Rossi, "Terahertz semiconductor-heterostructure laser," *Nature*, vol. 417, no. 6885, pp. 156–159, 2002.

[34] B. S. Williams, "Terahertz quantum-cascade lasers," *Nature Photonics*, vol. 1, no. 9, pp. 517–525, 2007.

[35] C. Walther, M. Fischer, G. Scalari, R. Terazzi, N. Hoyler, and J. Faist, "Quantum cascade lasers operating from 1.2 to 1.6 thz," *Applied Physics Letters*, vol. 91, no. 13, p. 131122, 2007.

[36] S. Kumar and A. W. M. Lee, "Resonant-phonon terahertz quantum-cascade lasers and video-rate terahertz imaging," *IEEE Journal of Selected Topics in Quantum Electronics*, vol. 14, no. 2, pp. 333–344, 2008.

[37] A. Wade, G. Fedorov, D. Smirnov, S. Kumar, B. S. Williams, Q. Hu, and J. L. Reno, "Magnetic-field-assisted terahertz quantum cascade laser operating up to 225 K," *Nature Photonics*, vol. 3, no. 1, pp. 41–45, 2009.

[38] G. Scalari, C. Walther, M. Fischer, R. Terazzi, H. Beere, D. Ritchie, and J. Faist, "THz and sub-THz quantum cascade lasers," *Laser and Photonics Reviews*, vol. 3, no. 1-2, pp. 45–66, 2009.

[39] J. Darmo, V. Tamosiunas, G. Fasching, J. Kröll, K. Unterrainer, M. Beck, M. Giovannini, J. Faist, C. Kremser, and P. Debbage, "Imaging with a terahertz quantum cascade laser," *Opt. Express*, vol. 12, no. 9, pp. 1879–1884, 2004.

[40] H.-B. Liu, Y. Chen, G. J. Bastiaans, and X.-C. Zhang, "Detection and identification of explosive RDX by THz diffuse reflection spectroscopy," *Opt. Express*, vol. 14, no. 1, pp. 415–423, 2006.

[41] J. R. Gao, J. N. Hovenier, Z. Q. Yang, J. J. A. Baselmans, A. Baryshev, M. Hajenius, T. M. Klapwijk, A. J. L. Adam, T. O. Klaassen, B. S. Williams, S. Kumar, Q. Hu, and J. L. Reno, "Terahertz heterodyne receiver based on a quantum cascade laser and a superconducting bolometer," *Applied Physics Letters*, vol. 86, no. 24, p. 244104, 2005.

[42] S. Fathololoumi, E. Dupont, C. Chan, Z. Wasilewski, S. Laframboise, D. Ban, A. Mátyás, C. Jirauschek, Q. Hu, and H. C. Liu, "Terahertz quantum cascade lasers operating up to $\sim$ 200 K with optimized oscillator strength and improved injection tunneling," *Opt. Express*, vol. 20, no. 4, pp. 3866–3876, 2012.

[43] M. Rochat, L. Ajili, H. Willenberg, J. Faist, H. Beere, G. Davies, E. Linfield, and D. Ritchie, "Low-threshold terahertz quantum-cascade lasers," *Applied Physics Letters*, vol. 81, no. 8, pp. 1381–1383, 2002.

[44] G. Scalari, L. Ajili, J. Faist, H. Beere, E. Linfield, D. Ritchie, and G. Davies, "Far-infrared ($\lambda\simeq$87 μm) bound-to-continuum quantum-cascade lasers operating up to 90 K," *Applied Physics Letters*, vol. 82, no. 19, pp. 3165–3167, 2003.

[45] C. Walther, G. Scalari, J. Faist, H. Beere, and D. Ritchie, "Low frequency terahertz quantum cascade laser operating from 1.6 to 1.8 THz," *Applied Physics Letters*, vol. 89, no. 23, p. 231121, 2006.

[46] B. S. Williams, H. Callebaut, S. Kumar, Q. Hu, and J. L. Reno, "3.4-THz quantum cascade laser based on longitudinal-optical-phonon scattering for depopulation," *Applied Physics Letters*, vol. 82, no. 7, pp. 1015–1017, 2003.

[47] B. Williams, S. Kumar, Q. Hu, and J. Reno, "Operation of terahertz quantum-cascade lasers at 164 K in pulsed mode and at 117 K in continuous-wave mode," *Opt. Express*, vol. 13, no. 9, pp. 3331–3339, 2005.

[48] S. Kumar, Q. Hu, and J. L. Reno, "186 K operation of terahertz quantum-cascade lasers based on a diagonal design," *Applied Physics Letters*, vol. 94, no. 13, p. 131105, 2009.

[49] F. Capasso, K. Mohammed, and A. Y. Cho, "Sequential resonant tunneling through a multiquantum well superlattice," *Applied Physics Letters*, vol. 48, no. 7, pp. 478–480, 1986.

[50] L. Sirigu, A. Rudra, E. Kapon, M. I. Amanti, G. Scalari, and J. Faist, "A terahertz quantum cascade laser grown by low-pressure metalorganic vapor phase epitaxy," *Applied Physics Letters*, vol. 92, no. 18, p. 181111, 2008.

[51] M. I. Amanti, G. Scalari, R. Terazzi, M. Fischer, M. Beck, J. Faist, A. Rudra, P. Gallo, and E. Kapon, "Bound-to-continuum terahertz quantum cascade laser with a single-quantum-well phonon extraction/injection stage," *New Journal of Physics*, vol. 11, no. 12, p. 125022, 2009.

[52] L. Ajili, G. Scalari, N. Hoyler, M. Giovannini, and J. Faist, "InGaAs–AlInAs/InP terahertz quantum cascade laser," *Applied Physics Letters*, vol. 87, no. 14, p. 141107, 2005.

[53] M. Fischer, G. Scalari, C. Walther, and J. Faist, "Terahertz quantum cascade lasers based on $In_{0.53}Ga_{0.47}As/In_{0.52}Al_{0.48}As$/InP," *Journal of Crystal Growth*, vol. 311, no. 7, pp. 1939 – 1943, 2009.

[54] C. Deutsch, A. Benz, H. Detz, P. Klang, M. Nobile, A. M. Andrews, W. Schrenk, T. Kubis, P. Vogl, G. Strasser, and K. Unterrainer, "Terahertz quantum cascade lasers based on type II InGaAs/GaAsSb/InP," *Applied Physics Letters*, vol. 97, no. 26, p. 261110, 2010.

[55] H. Detz, C. Deutsch, M. Nobile, P. Klang, A. Andrews, C. Schwarzer, W. Schrenk, K. Unterrainer, and G. Strasser, "InGaAs/GaAsSb terahertz quantum cascade lasers," in *Lasers and Electro-Optics (CLEO), 2011 Conference on*, pp. 1 –2, may 2011.

[56] J. Faist, F. Capasso, C. Sirtori, D. Sivco, and A. Cho, *Intersubband transitions in quantum wells: Physics and device applications II*, vol. 66, ch. 1, pp. 1–83. Academic, San Diego, 2000.

[57] K. Unterrainer, R. Colombelli, C. Gmachl, F. Capasso, H. Y. Hwang, A. M. Sergent, D. L. Sivco, and A. Y. Cho, "Quantum cascade lasers with double metal-semiconductor waveguide resonators," *Applied Physics Letters*, vol. 80, no. 17, pp. 3060–3062, 2002.

[58] B. S. Williams, S. Kumar, H. Callebaut, Q. Hu, and J. L. Reno, "Terahertz quantum-cascade laser at $\lambda \approx 100$ μm using metal waveguide for mode confinement," *Applied Physics Letters*, vol. 83, no. 11, pp. 2124–2126, 2003.

[59] B. S. Williams, *Terahertz quantum-cascade lasers*. PhD thesis, Dept. of Electrical Engineering and Computer Science, MIT, Cambridge, MA, 2003.

[60] S. Kumar, B. S. Williams, S. Kohen, Q. Hu, and J. L. Reno, "Continuous-wave operation of terahertz quantum-cascade lasers above liquid-nitrogen temperature," *Applied Physics Letters*, vol. 84, no. 14, pp. 2494–2496, 2004.

[61] S. Kumar, *Development of terahertz quantum-cascade lasers*. PhD thesis, Dept. of Electrical Engineering and Computer Science, MIT, Cambridge, MA, 2007.

[62] Y. Chassagneux, J. Palomo, R. Colombelli, S. Barbieri, S. Dhillon, C. Sirtori, H. Beere, J. Alton, and D. Ritchie, "Low threshold THz QC lasers with thin core regions," *Electronics Letters*, vol. 43, no. 5, pp. 41–42, 2007.

[63] E. Strupiechonski, D. Grassani, D. Fowler, F. H. Julien, S. P. Khanna, L. Li, E. H. Linfield, A. G. Davies, A. B. Krysa, and R. Colombelli, "Vertical subwavelength mode confinement in terahertz and mid-infrared quantum cascade lasers," *Applied Physics Letters*, vol. 98, no. 10, p. 101101, 2011.

[64] B. Williams, S. Kumar, Q. Hu, and J. Reno, "High-power terahertz quantum-cascade lasers," *Electronics Letters*, vol. 42, no. 2, pp. 89–91, 2006.

[65] A. J. L. Adam, I. Kasalynas, J. N. Hovenier, T. O. Klaassen, J. R. Gao, E. E. Orlova, B. S. Williams, S. Kumar, Q. Hu, and J. L. Reno, "Beam patterns of terahertz quantum cascade lasers with subwavelength cavity dimensions," *Applied Physics Letters*, vol. 88, no. 15, p. 151105, 2006.

[66] S. Kohen, B. S. Williams, and Q. Hu, "Electromagnetic modeling of terahertz quantum cascade laser waveguides and resonators," *Journal of Applied Physics*, vol. 97, no. 5, p. 053106, 2005.

[67] P. Hon, A. Tavallaee, Q.-S. Chen, B. Williams, and T. Itoh, "Radiation model for terahertz transmission-line metamaterial quantum-cascade lasers," *Terahertz Science and Technology, IEEE Transactions on*, vol. 2, no. 3, pp. 323 –332, 2012.

[68] M. Amanti, M. Fischer, C. Walther, G. Scalari, and J. Faist, "Horn antennas for terahertz quantum cascade lasers," *Electronics Letters*, vol. 43, no. 10, pp. 573–574, 2007.

[69] A. W. M. Lee, Q. Qin, S. Kumar, B. S. Williams, Q. Hu, and J. L. Reno, "High-power and high-temperature THz quantum-cascade lasers based on lens-coupled metal-metal waveguides," *Opt. Lett.*, vol. 32, no. 19, pp. 2840–2842, 2007.

[70] W. Maineult, P. Gellie, A. Andronico, P. Filloux, G. Leo, C. Sirtori, S. Barbieri, E. Peytavit, T. Akalin, J.-F. Lampin, H. E. Beere, and D. A. Ritchie, "Metal-metal terahertz quantum cascade laser with micro-transverse-electromagnetic-horn antenna," *Applied Physics Letters*, vol. 93, no. 18, p. 183508, 2008.

[71] J. A. Fan, M. A. Belkin, F. Capasso, S. Khanna, M. Lachab, A. G. Davies, and E. H. Linfield, "Surface emitting terahertz quantum cascade laser with a double-metal waveguide," *Opt. Express*, vol. 14, no. 24, pp. 11672–11680, 2006.

[72] S. Kumar, B. S. Williams, Q. Qin, A. W. Lee, Q. Hu, and J. L. Reno, "Surface-emitting distributed feedback terahertz quantum-cascade lasers in metal-metal waveguides," *Opt. Express*, vol. 15, no. 1, pp. 113–128, 2007.

[73] L. Mahler, A. Tredicucci, F. Beltram, C. Walther, J. Faist, H. E. Beere, and D. A. Ritchie, "High-power surface emission from terahertz distributed feedback lasers with a dual-slit unit cell," *Applied Physics Letters*, vol. 96, no. 19, p. 191109, 2010.

[74] M. I. Amanti, M. Fischer, G. Scalari, M. Beck, and J. Faist, "Low-divergence single-mode terahertz quantum cascade laser," *Nature Photonics*, vol. 3, no. 10, pp. 586–590, 2009.

[75] M. I. Amanti, G. Scalari, F. Castellano, M. Beck, and J. Faist, "Low divergence Terahertz photonic-wire laser," *Opt. Express*, vol. 18, no. 6, pp. 6390–6395, 2010.

[76] T.-Y. Kao, Q. Hu, and J. L. Reno, "Perfectly phase-matched third-order distributed feedback terahertz quantum-cascade lasers," *Opt. Lett.*, vol. 37, pp. 2070–2072, Jun 2012.

[77] L. Sirigu, R. Terazzi, M. I. Amanti, M. Giovannini, J. Faist, L. A. Dunbar, and R. Houdré, "Terahertz quantum cascade lasers based on two-dimensional photonic crystal resonators," *Opt. Express*, vol. 16, no. 8, pp. 5206–5217, 2008.

[78] O. P. Marshall, V. Apostolopoulos, J. R. Freeman, R. Rungsawang, H. E. Beere, and D. A. Ritchie, "Surface-emitting photonic crystal terahertz quantum cascade lasers," *Applied Physics Letters*, vol. 93, no. 17, p. 171112, 2008.

[79] Y. Chassagneux, R. Colombelli, W. Maineult, S. Barbieri, H. E. Beere, D. A. Ritchie, S. P. Khanna, E. H. Linfield, and A. G. Davies, "Electrically pumped photonic-crystal terahertz lasers controlled by boundary conditions," *Nature*, vol. 457, no. 7226, pp. 174–178, 2009.

[80] G. Xu, R. Colombelli, S. P. Khanna, A. Belarouci, X. Letartre, L. Li, E. H. Linfield, A. G. Davies, H. E. Beere, and D. A. Ritchie, "Efficient power extraction in surface-emitting semiconductor lasers using graded photonic," *Nature Communications*, vol. 3, no. 952, 2012.

[81] J. Lloyd-Hughes, G. Scalari, A. van Kolck, M. Fischer, M. Beck, and J. Faist, "Coupling terahertz radiation between sub-wavelength metal-metal waveguides and free space using monolithically integrated horn antennae," *Opt. Express*, vol. 17, no. 20, pp. 18387–18393, 2009.

[82] T.-Y. Kao, Q. Hu, and J. L. Reno, "Phase-locked arrays of surface-emitting terahertz quantum-cascade lasers," *Applied Physics Letters*, vol. 96, no. 10, p. 101106, 2010.

[83] L. Mahler, A. Tredicucci, F. Beltram, C. Walther, J. Faist, H. E. Beere, D. A. Ritchie, and D. S. Wiersma, "Quasi-periodic distributed feedback laser," *Nature Photonics*, vol. 4, no. 3, pp. 165–169, 2010.

[84] L. Mahler, A. Tredicucci, F. Beltram, C. Walther, J. Faist, B. Witzigmann, H. E. Beere, and D. A. Ritchie, "Vertically emitting microdisk lasers," *Nature Photonics*, vol. 3, no. 1, pp. 46–49, 2009.

[85] L. Mahler, M. I. Amanti, C. Walther, A. Tredicucci, F. Beltram, J. Faist, H. E. Beere, and D. A. Ritchie, "Distributed feedback ring resonators for vertically emitting terahertz quantum cascade lasers," *Opt. Express*, vol. 17, no. 15, pp. 13031–13039, 2009.

[86] H. Zhang, L. A. Dunbar, G. Scalari, R. Houdré, and J. Faist, "Terahertz photonic crystal quantum cascade lasers," *Opt. Express*, vol. 15, no. 25, pp. 16818–16827, 2007.

[87] G. Sevin, D. Fowler, G. Xu, F. Julien, R. Colombelli, H. Beere, and D. Ritchie, "Continuous-wave operation of 2.7 THz photonic crystal quantum cascade lasers," *Electronics Letters*, vol. 46, no. 22, pp. 1513–1515, 2010.

[88] T.-Y. Kao, Q. Hu, and J. L. Reno, "THz QCLs with high power extraction efficiency based on slot antennas," in *International Quantum Cascade Lasers School and Workshop*, 2012.

[89] A. A. Tavallaee, B. S. Williams, P. W. C. Hon, T. Itoh, and Q.-S. Chen, "Terahertz quantum-cascade laser with active leaky-wave antenna," *Applied Physics Letters*, vol. 99, no. 14, p. 141115, 2011.

[90] C. Caloz and T. Itoh, "Transmission line approach of left-handed (LH) materials and microstrip implementation of an artificial LH transmission line," *IEEE Transactions on Antennas and Propagation*, vol. 52, no. 5, pp. 1159–1166, 2004.

[91] H.-T. Chen, W. J. Padilla, J. M. O. Zide, A. C. Gossard, A. J. Taylor, and R. D. Averitt, "Active terahertz metamaterial devices," *Nature*, vol. 444, no. 7119, pp. 597–600, 2006.

[92] A. Yariv, *Quantum electronics*. J. Wiley, 3rd ed.

[93] M. McLennan and S. Datta, "Sequal Users Manual." Purdue University, Layfayette, 1989.

[94] C. Sirtori, H. Page, C. Becker, and V. Ortiz, "GaAs-AlGaAs quantum cascade lasers: physics, technology, and prospects," *IEEE Journal of Quantum Electronics*, vol. 38, pp. 547 –558, jun 2002.

[95] S. Adachi, "GaAs, AlAs, and Al[sub x]Ga[sub 1 - x]As: Material parameters for use in research and device applications," *Journal of Applied Physics*, vol. 58, no. 3, pp. R1–R29, 1985.

[96] H. Callebaut and Q. Hu, "Importance of coherence for electron transport in terahertz quantum cascade lasers," *Journal of Applied Physics*, vol. 98, no. 10, p. 104505, 2005.

[97] H. Callebaut, S. Kumar, B. S. Williams, Q. Hu, and J. L. Reno, "Analysis of transport properties of tetrahertz quantum cascade lasers," *Applied Physics Letters*, vol. 83, no. 2, pp. 207–209, 2003.

[98] Y. Chassagneux, Q. Wang, , S. Khanna, E. Strupiechonski, J. Coudevylle, E. Linfield, A. Davies, F. C. M.A., B. R., and Colombelli, "Limiting factors to the temperature performance of thz quantum cascade lasers based on the resonant-phonon depopulation scheme," *IEEE Transactions on Terahertz Science and Technology,*, vol. 2, no. 1, pp. 83–92, 2012.

[99] S. Kumar, B. S. Williams, Q. Hu, and J. L. Reno, "1.9 THz quantum-cascade lasers with one-well injector," *Applied Physics Letters*, vol. 88, no. 12, p. 121123, 2006.

[100] J. T. Robinson, K. Preston, O. Painter, and M. Lipson, "First-principle derivation of gain in high-index-contrast waveguides," *Opt. Express*, vol. 16, no. 21, pp. 16659–16669, 2008.

[101] N. W. Ashcroft and N. D. Mermin, *Solid state physics*. Saunders college, 1976.

[102] J. A. Fan, M. A. Belkin, F. Capasso, S. P. Khanna, M. Lachab, A. G. Davies, and E. H. Linfield, "Wide-ridge metal-metal terahertz quantum cascade lasers with high-order lateral mode suppression," *Applied Physics Letters*, vol. 92, no. 3, p. 031106, 2008.

[103] N. Laman and D. Grischkowsky, "Terahertz conductivity of thin metal films," *Applied Physics Letters*, vol. 93, no. 5, p. 051105, 2008.

[104] M. J. Madou, *Fundamentals of microfabrication: the science of miniaturization*. CRC Press, 2nd ed., 2002.

[105] V. M. Lubecke, K. Mizuno, and G. M. Rebeiz, "Micromachining for terahertz applications," *IEEE Transactions on Microwave Theory and Techniques*, vol. 46, pp. 1821–1831, Nov. 1998.

[106] P. H. Siegel, P. de Maagt, and A. I. Zaghloul, "Antennas for terahertz applications," in *Antennas and Propagation Society International Symposium 2006, IEEE*, pp. 2383–2386, july 2006.

[107] J. P. Becker, J. R. East, and L. B. Katehi, "Performance of silicon micromachined waveguide at W-band," *Electronics Letters*, vol. 38, pp. 638–639, Jun. 2002.

[108] B. Veidt, K. Kornelsen, J. F. Vaneldik, D. Routledge, and M. J. Brett, "Diagonal horn integrated with micromachined waveguide for submillimeter applications," *Electronics Lett.*, vol. 31, pp. 1307–1309, Aug. 1995.

[109] B. A. Shenouda, L. W. Pearson, and J. E. Harriss, "Etched-silicon micromashined W-band waveguides and horn antennas," *IEEE Transactions on Microwave Theory and Techniques*, vol. 49, pp. 724–727, Apr. 2001.

[110] J. L. Hesler, K. Hui, R. K. Dahlstrom, R. M. Weikle, T. W. Crowe, C. M. Mann, and H. B. Wallace, "Analysis of an octagonal micromachined horn antenna for submillimeter-wave applications," *IEEE Transactions on Antennas and Propagation*, vol. 49, pp. 997–1001, Jun. 2001.

[111] S. Biber, A. Murk, L. P. Schmidt, and N. Kämfer, "Design and measurement of a 600 GHz micromachined horn antenna manufactured by combined drie and koh-etching of silicon," *International Symposium on sapce terahertz technology*, 2005.

[112] B. S. Williams, S. Kumar, Q. Hu, and J. L. Reno, "Distributed-feedback terahertz quantum-cascade lasers with laterally corrugated metal waveguides," *Opt. Lett.*, vol. 30, pp. 2909–2911, 2005.

[113] M. Wanke, C. Nordquist, C. Arrington, A. Rowen, A. Grine, E. Shaner, and M. Lee, "Integration of terahertz quantum cascade lasers with lithographically micromachined waveguides," in *33rd International Conference on Infrared, Millimeter and Terahertz Waves (IRMMW-THz 2008)*, p. 1, 2008.

[114] M. C. Wanke, C. D. Nordquist, M. J. Cich, A. M. Rowen, C. L. Arrington, M. Lee, A. D. Grine, C. T. Fuller, J. L. Reno, and E. W. Young, "Terahertz quantum cascade laser integration with on-chip micromachined rectangular waveguides," vol. 7215, p. 721504, SPIE, 2009.

[115] A. O. Dirisu, G. Silva, Z. Liu, C. F. Gmachl, F. J. Towner, J. Bruno, and D. L. Sivco, "Reduction of facet reflectivity of quantum-cascade lasers with subwavelength gratings," *Photonics Technology Letters, IEEE*, vol. 19, no. 4, pp. 221 –223, 2007.

[116] D. R. Smith, W. J. Padilla, D. C. Vier, S. C. Nemat-Nasser, and S. Schultz, "Composite medium with simultaneously negative permeability and permittivity," *Phys. Rev. Lett.*, vol. 84, pp. 4184–4187, Dec. 2000.

[117] J. B. Pendry, A. J. Holden, D. J. Robbins, and W. J. Stewart, "Magnetism from conductors and enhanced nonlinear phenomena," *IEEE Transactions on Microwave Theory and Techniques*, vol. 47, pp. 2075–2084, Nov. 1999.

[118] R. W. Ziolkowski, "Propagation in and scattering from a matched metamaterial having a zero index of refraction," *Phys. Rev. E*, vol. 70, p. 046608, Oct. 2004.

[119] V. A. Podolskiy and E. E. Narimanov, "Near-sighted superlens," *Opt. Lett.*, vol. 30, no. 1, pp. 75–77, 2005.

[120] E. Shamonina, V. A. Kalinin, K. H. Ringhofer, and L. Solymar, "Imaging, compression and poynting vector streamlines for negative permittivity materials," *Electron. Lett.*, vol. 37, pp. 1243–1244, Sep. 2001.

[121] S. A. Ramakrishna and J. B. Pendry, "Removal of absorption and increase in resolution in a near-field lens via optical gain," *Phys. Rev. B*, vol. 67, p. 201101, May 2003.

[122] M. A. Noginov, G. Zhu, M. Bahoura, J. Adegoke, C. E. Small, B. A. Ritzo, V. P. Drachev, and V. M. Shalaev, "Enhancement of surface plasmons in an Ag aggregate by optical gain in a dielectric medium," *Opt. Lett.*, vol. 31, pp. 3022–3024, Oct. 2006.

[123] A. K. Popov and V. M. Shalaev, "Compensating losses in negative-index metamaterials by optical parametric amplification," *Opt. Lett.*, vol. 31, pp. 2169–2171, Jul. 2006.

[124] V. M. Shalaev, "Optical negative-index metamaterials," *Nature Photonics*, vol. 1, pp. 41–48, Jan. 2007.

[125] T. J. Yen, W. J. Padilla, N. Fang, D. C. Vier, D. R. Smith, J. B. Pendry, D. N. Basov, and X. Zhang, "Terahertz magnetic response from artificial materials," *Science*, vol. 303, pp. 1494–1496, Mar. 2004.

[126] T. Driscoll, G. O. Andreev, D. N. Basov, S. Palit, S. Y. Cho, N. M. Jokerst, and D. R. Smith, "Tuned permeability in terahertz split-ring resonators for devices and sensors," *Appl. Phys. Lett.*, vol. 91, p. 062511, Aug. 2007.

[127] H.-T. Chen, J. F. O'Hara, A. K. Azad, A. J. Taylor, R. D. Averitt, D. B. Shrekenhamer, and W. J. Padilla, "Experimental demonstration of frequency-agile terahertz metamaterials," *Nature Photonics*, vol. 2, pp. 295–298, Apr. 2008.

[128] T. Crepin, J. F. Lampin, T. Decoopman, X. Melique, L. Desplanque, and D. Lippens, "Experimental evidence of backward waves on terahertz left-handed transmission lines," *Appl. Phys. Lett.*, vol. 87, p. 104105, Sep. 2005.

[129] C. Caloz and T. Itoh, "Application of the transmission line theory of left-handed (LH) materials to the realization of a microstrip LH transmission line," *Proc. IEEE-APS USNC/URSI National Radio Science Meeting*, vol. 2, pp. 412–415, Jun. 2002.

[130] G. V. Eleftheriades, A. K. Iyer, and P. C. Kremer, "Planar negative refractive index media using periodically L-C loaded transmission lines," *IEEE Transactions on Microwave Theory and Techniques*, vol. 50, pp. 2702–2712, Dec. 2002.

[131] A. A. Oliner, "A planar negative-refractive-index medium without resonant elements," *IEEE MTT-S Int. Microw. Symp. Dig.*, pp. 191–194, Jun. 2003.

[132] A. Alù and N. Engheta, "Optical nanotransmission lines: synthesis of planar left-handed metamaterials in the infrared and visible regimes," *J. Opt. Soc. Am. B*, vol. 23, pp. 571–583, Mar. 2006.

[133] J. B. Khurgin and G. Sun, "Scaling of losses with size and wavelength in nanoplasmonics and metamaterials," *Applied Physics Letters*, vol. 99, no. 21, p. 211106, 2011.

[134] C. Caloz and T. Itoh, *Electromagnetic metamaterials: transmission line theory and microwave applications*. Wiley-IEEE Press, 2005.

[135] J. Kröll, J. Darmo, K. Unterrainer, S. S. Dhillon, and C. Sirtori, "Longitudinal spatial hole burning in terahertz quantum cascade lasers," *Appl. Phys. Lett.*, vol. 91, p. 161108, Oct. 2007.

[136] A. Gordon, C. Y. Wang, L. Diehl, F. X. Kartner, A. Belyanin, D. Bour, S. Corzine, G. Hofler, H. C. Liu, H. Schneider, T. Maier, M. Troccoli, J. Faist, and F. Capasso, "Multimode regimes in quantum cascade lasers:

From coherent instabilities to spatial hole burning," *Phys. Rev. A (Atomic, Molecular, and Optical Physics)*, vol. 77, p. 053804, May 2008.

[137] T. Gresch, M. Giovannini, N. Hoyer, and J. Faist, "Quantum cascade lasers with large optical waveguides," *IEEE Photon. Tech. Lett.*, vol. 18, pp. 544–546, Feb. 2006.

[138] J. Kröll, J. Darmo, S. S. Dhillon, X. Marcadet, M. Calligaro, C. Sirtori, and K. Unterrainer, "Phase-resolved measurements of stimulated emission in a laser," *Nature*, vol. 449, pp. 698–701, Oct. 2007.

[139] H. Li, J. C. Cao, J. T. Lü, and Y. J. Han, "Monte Carlo simulation of extraction barrier width effects on terahertz quantum cascade lasers," *Appl. Phys. Lett.*, vol. 92, p. 221105, Jun. 2008.

[140] A. A. Tavallaee, P. Hon, K. Mehta, T. Itoh, and B. Williams, "Zero-index terahertz quantum-cascade metamaterial lasers," *IEEE Journal of Quantum Electronics*, vol. 46, no. 7, pp. 1091–1098, 2010.

[141] R. Williams, *Modern GaAs processing methods*. Artech house, 1990.

[142] K. Mehta, Personal communication.

[143] C. Walther, G. Scalari, M. I. Amanti, M. Beck, and J. Faist, "Microcavity laser oscillating in a circuit-based resonator," *Science*, vol. 327, no. 5972, pp. 1495–1497, 2010.

[144] W. Menzel, "A new travelling wave antenna in microstrip," in *Microwave Conference, 8th European*, pp. 302–306, Sept. 1978.

[145] Z. Liu, P. W. C. Hon, A. A. Tavallaee, T. Itoh, and B. S. Williams, "Terahertz composite right-left handed transmission-line metamaterial waveguides," *Applied Physics Letters*, vol. 100, no. 7, p. 071101, 2012.

[146] P. W. Hon, A. A. Tavallaee, Z. Liu, B. S. Williams, and T. Itoh, "Radiation modeling of terahertz transmission-line metamaterials," in *CLEO:2012 - Laser Applications to Photonic Applications*, 2012.

[147] A. A. Tavallaee, M. Puckett, B. Williams, P. Hon, T. Itoh, and Q.-S. Chen, "A terahertz quantum-cascade laser with an active leaky-wave metamaterial antenna," in *CLEO:2011 - Laser Applications to Photonic Applications*, p. CThE1, Optical Society of America, 2011.

[148] J. M. Hensley, D. J. Bamford, M. G. Allen, J. Xu, A. Tredicucci, H. E. Beere, and D. A. Ritchie, "Demonstration of an external cavity terahertz quantum cascade laser," in *Optical Terahertz Science and Technology*, p. TuA3, Optical Society of America, 2005.

[149] J. Xu, J. M. Hensley, D. B. Fenner, R. P. Green, L. Mahler, A. Tredicucci, M. G. Allen, F. Beltram, H. E. Beere, and D. A. Ritchie, "Tunable terahertz quantum cascade lasers with an external cavity," *Applied Physics Letters*, vol. 91, no. 12, p. 121104, 2007.

[150] A. W. M. Lee, B. S. Williams, S. Kumar, Q. Hu, and J. L. Reno, "Tunable terahertz quantum cascade lasers with external gratings," *Opt. Lett.*, vol. 35, no. 7, pp. 910–912, 2010.

[151] Q. Qin, B. S. Williams, S. Kumar, J. L. Reno, and Q. Hu, "Tuning a terahertz wire laser," *Nature Photonics*, vol. 3, no. 12, pp. 732–737, 2009.

[152] D. Dini, R. Köhler, A. Tredicucci, G. Biasiol, and L. Sorba, "Microcavity polariton splitting of intersubband transitions," *Phys. Rev. Lett.*, vol. 90, p. 116401, 2003.

[153] Y. Todorov, A. M. Andrews, I. Sagnes, R. Colombelli, P. Klang, G. Strasser, and C. Sirtori, "Strong light-matter coupling in subwavelength metal-dielectric microcavities at terahertz frequencies," *Phys. Rev. Lett.*, vol. 102, p. 186402, 2009.

[154] M. Geiser, C. Walther, G. Scalari, M. Beck, M. Fischer, L. Nevou, and J. Faist, "Strong light-matter coupling at terahertz frequencies at room temperature in electronic LC resonators," *Applied Physics Letters*, vol. 97, no. 19, p. 191107, 2010.

[155] E. Strupiechonski, G. Xu, M. Brekenfeld, Y. Todorov, N. Isac, A. M. Andrews, P. Klang, C. Sirtori, G. Strasser, A. Degiron, and R. Colombelli, "Sub-diffraction-limit semiconductor resonators operating on the fundamental magnetic resonance," *Applied Physics Letters*, vol. 100, no. 13, p. 131113, 2012.

[156] R. Colombelli, C. Ciuti, Y. Chassagneux, and C. Sirtori, "Quantum cascade intersubband polariton light emitters," *Semiconductor Science and Technology*, vol. 20, no. 10, p. 985, 2005.